ELSEVIER

Infrared Physics & Technology 39 (1998) 123–183

INFRARED PHYSICS
& TECHNOLOGY

Nanometer thin-film Ni–NiO–Ni diodes for detection and mixing of 30 THz radiation

C. Fumeaux [a], W. Herrmann [a], F.K. Kneubühl [a,*], H. Rothuizen [b]

[a] *Institute of Quantum Electronics, Swiss Federal Institute of Technology (ETH), CH-8093 Zürich, Switzerland*
[b] *IBM Research Laboratory, Säumerstrasse 4, CH-8803 Rüschlikon, Switzerland*

Received 12 December 1997

Abstract

We report on the realization and the experimental study of thin-film Ni–NiO–Ni diodes with integrated infrared antennas. These diodes are applied as detectors and mixers of 28-THz CO_2-laser radiation with difference frequencies up to 176 GHz. They constitute a mechanically stable alternative to the point-contact MOM diodes used today in heterodyne detection of such high frequencies. Thus, they represent the extension of present millimeter-wave and microwave thin-film and antenna techniques to the infrared. Our thin-film Ni–NiO–Ni diodes are fabricated on SiO_2/Si substrates with the help of electron-beam lithography at the IBM Research Laboratory (Rüschlikon, Switzerland). We have reduced the contact area to 110 nm × 110 nm in order to achieve a fast response of the device. This contact area is in the order of those of point-contact diodes and represents the smallest ever reported for thin-film MOM diodes. The thin NiO layer with a thickness of about 35 Å is deposited by sputtering. Our thin-film diodes are integrated with planar dipole, bow-tie and spiral antennas that couples the incident field to the contact. The second derivative $I''(V)$ of the nonlinear $I(V)$ characteristics at the bias voltage applied to the diode is measured at a frequency of 10 kHz. It determines the detection and second-order mixing performed with the diode for frequencies from dc to at least 30 THz. The $I''(V)$ characteristics exhibit for low bias voltage V_{bias} a linear dependence, which is followed by a saturation and a maximum for high V_{bias}. The zero-bias resistance of the diode is in the order of 100 Ω. It is not strictly inversely proportional to the contact area of the diode. The first application of our thin-film diodes was the detection of cw CO_2-laser radiation. The measured dc signal generated by the diode when illuminated with 10.6-μm radiation includes a polarization-independent contribution, caused by thermal effects. This contribution is independent of the contact area and of the type of integrated antenna. The polarization-dependent contribution of the signal originates in the rectification of the antenna currents in the diode by nonlinear tunneling through the thin NiO layer. It follows a cosine-squared dependence on the angle of orientation of the linear polarization, as expected from antenna theory. For the linearly polarized dipole and bow-tie antennas, the maximum detection signals are therefore measured for the polarization parallel to the antenna axis. Bow-tie antennas with a half length of 2.3 μm generate the highest detection signals. The full length of these antennas corresponds to $3/2$ of the wavelength of the incident 10.6-μm radiation in the supporting Si substrate. The relevance of the substrate wavelength confirms that our antennas are more sensitive to the radiation incident from the substrate side. The time of response of our thin-film diode is not limited by the speed of the electron-tunneling effect, but by the RC time constant of the diode circuitry. Thus, the overall best performances are attained by the diodes with the smallest contact areas and corresponding capacitances. The study of the

---

[*] Corresponding author. E-mail: kneubuhl@iqe.phys.ethz.ch.

1350-4495/98/$19.00 © 1998 Elsevier Science B.V. All rights reserved.
PII S1350-4495(98)00004-8

polarization response of our integrated asymmetric spiral antennas revealed the contribution of an unbalanced mode propagating on the antenna arms beside the fundamental balanced mode. The imbalance is caused by the reactive impedance of the diode and by the asymmetry of the antenna arms in the feed region. In addition, the response of the diode is influenced by reflection of the antenna currents near the end of the spiral arms. The resulting polarization of our spiral antenna is therefore not the expected circular polarization, yet an elliptical polarization with an axial ratio in the order of 0.12. Furthermore, we have demonstrated the presence of two distinct additive thermal effects besides the fast antenna-induced contribution by the measurement of the response of our thin-film diodes to 35 ps optical-free-induction decay (OFID) CO_2-laser pulses. The measured characteristic times of these two relatively slow relaxations are $\tau_1 \approx 100$ ns and $\tau_2 \approx 15$ ns. These exponential relaxations observed are explained by thermal diffusion in the SiO_2 and in the Ni layers of our structures. These time constants show that thermal effects influence mixing processes at low difference frequencies. For the first time, the operation of thin-film diodes as mixers of 28-THz radiation was demonstrated. Difference frequencies up to 176 GHz have been measured when the diode was irradiated by two CO_2-laser beams and microwaves generated by a Gunn oscillator working at 58.8 GHz. These difference frequencies were generated in mixing processes from the second to the fifth order. These experiments were performed with thin-film Ni–NiO–Ni diodes with the minimum contact area of 0.012 μm^2 and integrated resonant bow-tie antennas. The transmission of the high-frequency signals to the spectrum analyzer was accomplished using integrated rhodium waveguides and flip-chip connections. The diode and the antenna were irradiated through the substrate, taking advantage of the better sensitivity of the antenna to radiation incident from the substrate side. The dependence on the linear polarization of the mixing signal matches almost perfectly the ideal cosine-squared dependence predicted by antenna theory for bow-tie antennas. A ratio of the mixing signals for the polarization parallel to the axis vs. the cross-polarization of over 50 was attained. The signal-to-noise ratios of our mixing signals demonstrate the potential of our type of diodes to respond to even higher carrier and difference frequencies. Also higher-order mixing can be achieved with our thin-film diodes. © 1998 Elsevier Science B.V. All rights reserved.

Keywords: MOM and MIM diodes; Integrated infrared antenna; CO_2 laser radiation; THz mixing

1. Introduction

Mixing and detection with point-contact metal–oxide–metal (MOM or MIM) diodes at millimeter and submillimeter wavelengths were first reported in 1966 [1]. The working range of these devices was extended in the following years to infrared [2] and visible laser radiation [3,4]. These diodes consist of a thin metallic wire with a fine etched tip in weak contact with an oxidized metallic surface in the typical arrangement shown in Fig. 1. The most commonly used metal for the whisker is tungsten. It can be sharpened by electrical etching in NaOH or KOH that yields tip radii of less than 50 nm [5,6]. Contact areas in the order of 0.01 μm^2 are achieved. This results in a small capacitance that minimizes the response time. Various materials are used as metallic base, including, e.g., nickel [7], steel and silver [2]. The tungsten wire acts as a long-wire antenna and couples the applied radiation field to the diode [8]. A strong evidence of the whisker acting as antenna at infrared frequencies is manifested by the marked polarization dependence of the signal detected. This dependence is in good agreement with low-frequency antenna theory [5].

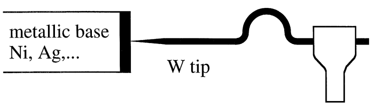

Fig. 1. Typical configuration of a point-contact MOM diode.

The main application of MOM diodes concerns mixers in heterodyne detection [9]. Because of their high speed of response, they have been extensively used in absolute frequency measurements for the development of time and frequency standards [10]. The capability of the MOM diodes to generate and reradiate difference frequencies permits their application as tunable cw FIR radiation source in high-resolution spectroscopy [11].

The use of MOM diodes as fast detectors for infrared and visible radiation is limited because of the problems caused by the point-contact configuration. The main disadvantage of point-contact diodes is their low mechanical stability. In addition, the sensitivity and the response time of these devices are strongly dependent on the contact area and on the oxide thickness. For this reason the point contacts are irreproducible. Hence, serious attempts have been made to integrate the MOM diodes on a substrate to achieve stability and reproducibility. In the early seventies, Small et al. [12] and Wang et al. [13] reported the fabrication of thin-film diodes with integrated antennas exhibiting rectification capabilities in the 10-μm region. Small et al. also reported on third-order frequency mixing performed with the HCN-laser emissions at 337 μm (890.2 GHz) and 311 μm (964.6 GHz) wavelength and the microwave radiation from a klystron. No other successful mixing with thin-film diodes has been reported since. Thin-film MOM diodes fabricated with optical lithography possess contact areas about a hundred times larger than point contacts, because of the micrometer resolution of this technique [14,15].

Besides the previously mentioned advantages of the thin-film configuration, the integration of MOM diodes on a substrate opens new fields of applications in detector and infrared antenna technologies. The possibility to integrate these devices in arrays allows the development of thermal imaging systems. Furthermore, thin-film MOM diodes constitute outstanding detectors for the study of integrated infrared antennas because of their fast response at room temperature. The understanding acquired in measurements with MOM diodes can be extended to other antenna-coupled detectors with dimensions considerably smaller than the wavelength of incident radiation, e.g., microbolometers [16].

Our development of thin-film MOM diodes started in 1976 [17]. The diodes were connected to long-wire antennas while the smallest contact areas produced with photolithographic techniques were in the order of 1.2 μm × 1.2 μm. Detection of CO_2-laser radiation with a wavelength of 10.6 μm was achieved yet showed a predominant thermal contribution. Smaller contacts were required in order to obtain a faster optical response. Years later, the application of electron-beam lithography permitted the manufacture of thin-film Ni–NiO–Ni diodes with a minimum contact area of 0.056 μm^2 [18,19]. These devices printed on SiO_2/Si substrates were integrated with dipole antennas that coupled the incident infrared CO_2-laser radiation efficiently to the diode.

This study describes the continuation of the development of the thin-film Ni–NiO–Ni diodes as fast antenna-coupled detectors on one hand and the extension of their range of operation to the mixing of 28-THz infrared radiation on the other hand. For these purposes, the contact area of the diode was reduced further to approximately 110 nm × 110 nm (Fig. 2) with the aid of electron-beam lithography. The minimum contact areas of about 0.012 μm^2 are smaller than those of any thin-film diodes reported previously. They are in the order of the areas of point contacts. The theoretical considerations for the development of our antenna-coupled thin-film diodes are summarized in Section 2, first with respect to the diode and second with regard to the infrared antennas. In the first part, a short description of nonlinear-conduction mechanisms and of circuit speed limitations in the device permits the identification of various contributions to the measured diode signals and demonstrates the requirement of a minimum contact area. In the second part, the antenna theory is extended to infrared antennas on a substrate and applied to our design of bow-tie and spiral antenna microstructures.

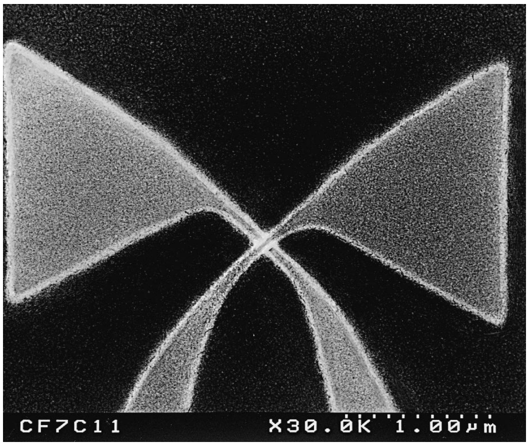

Fig. 2. Electron-microscope image of the thin-film Ni-NiO-Ni diode with a contact area of 0.012 μm^2 connected to an integrated bow-tie antenna.

The fabrication of our nanometer-scale thin-film diodes integrated with various types of antennas and the configurations of their connections to the amplifiers are presented in Section 3. The flip-chip connections have been a crucial issue for successful mixing experiments. They permitted irradiation of the diodes from the substrate side and an excellent transmission of the high-frequency mixing signals generated by the diode. The last part of Section 3 describes the preliminary electrical testing of the diodes at dc and radio frequencies. These measurements yield valuable information on the $I(V)$ characteristics that describe the nonlinearity of our Ni–NiO–Ni diodes from dc to at least 30 THz.

The infrared measurements performed with CO_2-laser radiation are described in Sections 4–6. Section 4 is devoted to the dc-response of the diodes to cw laser radiation. The observed substrate interference patterns prevailing for all diodes are presented first. Subsequently, the measurements performed on linear polarized antennas, i.e., dipole and bow-tie antennas, are described. The dependence of the diode detection-signals on the direction of the input polarization permits an approximate distinction between antenna-induced mechanisms and thermal effects. The characterization of the efficiency of the diode detection with regard to contact area and types of infrared antennas gives important information concerning the choice of the diodes best suited for mixing experiments. The antenna patterns observed for different antennas yielded an additional evidence of the efficient coupling of the radiation into the diode. Section 4.4 deals with the polarization response of asymmetric spiral antennas.

Section 5 describes the measurement of the interaction of short 35-ps OFID CO_2-laser pulses with our thin-film diodes. These experiments permit a classification of the different rectification mechanisms of the diode by their observed transients, and, also a characterization of the thermal effects. These are explained by a model based on the heat-conduction equation.

In Section 6, we report on the first mixing of 28-THz radiation with measurement of difference frequencies up to 176 GHz in mixing processes up to the fifth order. These experiments required the irradiation of the diode by two CO_2-laser beams as well as by microwaves generated by a Gunn oscillator. For this purpose, we have used thin-film Ni–NiO–Ni diodes with bow-tie antennas and integrated rhodium waveguides. The mixing signals exhibit a cosine-squared dependence on the polarization of the incident 10.7-μm CO_2-laser radiation. This demonstrates that our bow-tie antennas show almost complete polarization as predicted by antenna theory. These results verify the extension of millimeter-wave and microwave thin-film techniques to the infrared.

2. Theory

In this chapter we present the operation principle of MOM detectors and mixers. First we describe the nonlinearity of these diodes and the likely mechanisms responsible for this nonlinearity. The detection and mixing mechanisms are similar in point-contact and thin-film configurations. Thus, the basic theoretical considerations can be applied to both. Secondly we discuss the coupling of the incoming radiation field to the diode by the means of integrated antennas.

2.1. MOM diodes

2.1.1. Nonlinear response of MOM diodes

Because of the insulating thin oxide layer, the MOM diodes are not ohmic contacts. The nonlinearity of their $I(V)$ characteristics generates a dc component when a voltage with a circular frequency ω is applied. According to theory [20], the amplitude of the rectified signal V_{dc} is proportional to the second derivative of the $I(V)$ curve

$$V_{dc} \propto \frac{1}{4}\left(\frac{d^2I}{dV^2}\right)\Delta V^2, \tag{2.1}$$

where ΔV is the amplitude of the ac voltage that originates in the infrared radiation coupled to the MOM diode by the antenna. The generated dc signal is therefore proportional to the power of the incoming radiation. Hence the diode acts as a square-law detector.

Similarly when diode and antenna are illuminated simultaneously with two laser beams of frequencies ω_1 and ω_2, a voltage oscillating with the difference frequency $\omega_1 - \omega_2$ is generated. Accordingly, the amplitude $V_{\omega_1 - \omega_2}$ of the beat frequency signal is proportional to

$$V_{\omega_1 - \omega_2} \propto \frac{1}{2}\left(\frac{d^2I}{dV^2}\right)\Delta V_1 \Delta V_2, \tag{2.2}$$

where the ΔV's indicate the amplitudes of the dc voltages coupled to the diode by the antenna and the indices 1 and 2 refer to the contributions by each laser beam. The higher-order mixing is described by the term of the Taylor expansion of the $I(V)$ characteristics corresponding to the mixing order.

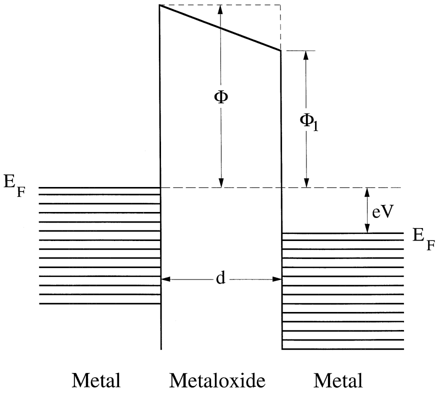

Fig. 3. Energy diagram of the MOM diode.

2.1.2. Rectification and mixing mechanisms in MOM diodes

A simplified energy diagram of an MOM diode is shown in Fig. 3. The thin oxide layer between the two nickel electrodes represents a potential barrier with a thickness d and a height Φ that is described by a rectangle function in a first-order approximation. The symmetry of a structure with two similar electrodes that possess the same Fermi level is distorted by applying a bias voltage V on the contact. This gives rise to the diode characteristics of the MOM structure.

Various effects contribute to the detection and mixing mechanisms in MOM diodes. The different electrical-conduction processes exhibit distinct properties and characteristic times. In most cases, several additive conduction mechanisms are active simultaneously. Therefore, it is difficult to decide which is predominant. In the following we summarize the generally accepted conduction mechanisms.

2.1.2.1. Electron tunneling. According to quantum mechanics, electrons in metals can tunnel through a high barrier. The probability for electrons of passing through a potential barrier falls exponentially with its thickness. Thus, the oxide layer thickness should not exceed a few tens of angstroms [21]. A theoretical analysis was performed by Simmons [22]. It yielded an expression for the tunnel current as a function of the barrier height Φ, its thickness d and permittivity ε. In that calculation, the deformation of the rectangular potential barrier by image forces was taken into account. The tunneling effect is nonlinear and permits rectification and mixing of the infrared radiation coupled by the antenna to the diode.

The theoretical calculation of the tunneling time remains an unsolved problem: Several different approaches were tried without success [23]. Estimation of the tunneling time yields values in the range from 10^{-15} to 10^{-16} s. An absolute frequency measurement was performed at a frequency of 148 THz by Jennings et al. [24], which showed that the tunneling time is not a limit for the mixing of 30-THz laser radiation.

Difference-frequency generation was also achieved in the visible range in the early 1980's, although with a poor conversion efficiency [4,25,26]. In the visible range, photo-assisted tunneling seems to play an important role in the detection and mixing mechanism [27] because the photo-energy gained by electrons is in the range of the barrier height of 1 to 2 eV. At infrared frequencies near 30 THz, however, this effect is negligible compared to field-assisted tunneling [28].

2.1.2.2. Thermionic emission. Absorption of radiation increases the temperature of the MOM diode. Thermally excited electrons can therefore be emitted above the potential barrier. For point-contact diodes used at infrared frequencies, this effect yields no significant contribution because of the poor absorptivity of metal in this range [5,6]. At visible frequencies however, thermal effects seem to dominate the detection mechanism [4]. A theoretical treatment of thermal currents that includes a comparison with the tunneling currents was published by Simmons [29]. This calculation predicts that thermally excited currents become predominant for oxide barriers thicker than 50 Å.

In the case of thin-film MOM diodes, absorption of the incoming radiation also occurs in the substrate. The thermal contribution is important for these devices and has been intensively investigated by Wilke et al. [18] for the case of thin-film Ni–NiO–Ni diodes. They demonstrate that the heating of the diode is mainly caused by absorption of infrared radiation in the SiO_2-layer of the substrate and by dissipation of antenna currents.

The thermal effects are inherently slow because they are limited by the thermal time constant of the junction. They certainly represent a significant contribution to the detector response for the dc detection of radiation, but are too slow to play a role in mixing processes beyond a cut-off frequency [30]. This frequency is determined by the thermal time constant of the structure and depends strongly on the heat conductivity of the material used and on the geometry of the diode.

2.1.2.3. Spreading resistance. Evidence that spreading resistance also contributes to the nonlinear operation of Ni–NiO–Ni diodes was found by Wilke et al. [18]. This effect relies on the inelastic scattering of electrons by phonons in the bulk material. It is observed for metal–metal and low-resistance contacts [31–33]. It is likely that pinholes in the 35-Å NiO layer of our diodes are responsible for this effect because they represent a small conductive path [34]. The spreading-resistance nonlinearity can contribute simultaneously with tunneling mechanisms. However, the high-frequency cut off is expected to be lower than for electron tunneling, i.e., between 10^{13} and 10^{14} Hz [33].

2.1.3. RC time constant of thin-film MOM diodes

In order to mix different radiation sources at infrared frequencies, MOM diodes must have a fast response time. As mentioned before the tunneling mechanism is faster than one infrared wave cycle. Consequently, it is not a limiting factor in achieving a sufficiently fast response. Therefore, the circuit speed limit of the diode determines the response time. In the equivalent circuit presented in Fig. 4, the diode is described by a junction capacitance C_D in parallel with an internal nonlinear resistance $R_D(V)$. It is connected in series with the resistance R_A of the antenna. The cut-off frequency of the circuitry is defined as [35]:

$$\nu_c = \frac{1}{2\pi R_A C_D}. \tag{2.3}$$

Rectification and mixing are still observed above this frequency, but with rapidly decreasing efficiencies. Sanchez et al. [35] calculate a signal amplitude decreasing as $\omega^{-3/2}$ for frequencies above the cut-off frequency while results of other calculations range from a ω^{-1} [36,12] to a ω^{-2} variation [37]. To minimize the response time and attain a high cut-off frequency, the diode capacitance must be small according to Eq. (2.3). For a thin-film MOM diode, the contact is produced by two overlapping thin metal strips separated by a thin oxide layer. In a first approach the junction is considered as a small parallel-plate capacitor with the capacitance

$$C_D = \varepsilon\varepsilon_0 \frac{A}{d}, \tag{2.4}$$

where ε represents the relative electric permittivity of the oxide, d the thickness of the oxide layer and A the junction area determined by the width of the metal strips. To minimize this capacitance, the oxide layer must not be too thin and the area of the contact has to be small. Measurements show that the thickness of the nickel oxide layer is about 35 Å [18]. No further attempt was made to increase this thickness because this would reduce the tunnel currents. A better approach to attain a fast response is to reduce the contact area [37]. In order to have an RC-limited cut-off frequency higher than the 30-THz frequency of 10-μm CO_2-laser radiation, structure widths on the order of 100 nm are required, leading to a capacitance of approximately 0.1 fF. For thin-film diodes, this requirement cannot be fulfilled with conventional photolithographic techniques. Their fabrication requires the resolution of electron-beam lithography.

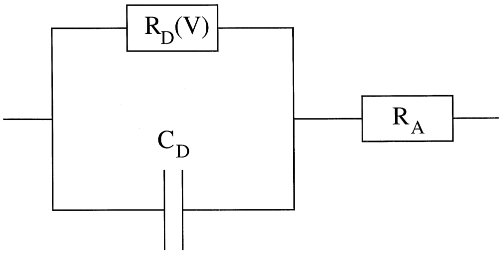

Fig. 4. Equivalent circuit model for the diode and antenna.

2.2. Antenna theory

The dimensions of the MOM diodes are much smaller than the wavelengths of interest. The coupling of the incident radiation field to the diodes can be substantially improved by connecting them to antennas much larger than the diode. The responsivity of the diode is considerably influenced by the geometry of this antenna. In the case of point-contact diodes, the metal whisker was shown to act as a long-wire antenna. For the same purpose, thin-film MOM diodes are connected to integrated antennas. In the first part of this section, we discuss the influence of the substrate on the properties of these antennas. Then we describe the characteristics of the various types of antennas used in this study, including dipole, bow-tie, and spiral antennas.

2.2.1. Antenna on a substrate

A planar antenna in free space radiates equally on both sides of its plane because of symmetry. The presence of a dielectric substrate on one side of the antenna breaks this symmetry and changes the current distribution and the wave velocity in the antenna. It has been observed that an antenna on a substrate radiates most of the power into the dielectric [38]. According to the reciprocity theorem [39], these antennas couple dominantly radiation incident from the substrate side. As in the transmission-line theory, the waves in the antenna propagate at a velocity that is intermediate between air and dielectric wave velocity [40]. This holds for an elementary dipole at the interface between air and a dielectric, but this statement can be extended to any antenna by considering it as an ensemble of elementary radiating dipoles. The ratio of radiated power in the dielectric P_{subst} and in the air P_{air} is given by

$$\frac{P_{\mathrm{subst}}}{P_{\mathrm{air}}} = \left(\frac{\varepsilon_{\mathrm{subst}}}{\varepsilon_{\mathrm{air}}} \right)^{3/2}, \qquad (2.5)$$

where $\varepsilon_{\mathrm{subst}}$ represents the relative electric permittivity of the substrate. For our silicon substrate $\varepsilon_{\mathrm{subst}}$ is about 11.7 for 10.6-μm wavelength. This yields about 40 times more radiation in the substrate than in the air. In order to take advantage of this fact, a receiving antenna should be illuminated from the substrate side. The use of a substrate lens (see, e.g., Ref. [41]) combines the advantages of the better response of the antenna to the substrate-side radiation and of reduced losses caused by surface waves in the substrate. We have used another scheme for our thin-film MOM diodes [19]: The SiO_2-layer of the substrate is optimized as an anti-reflection coating, while the back side of the chip is coated with a gold mirror or mounted on a gold socket. Thus, infrared radiation coming from the air side and then transmitted by the substrate is reflected back to the diode and the antenna. The interference patterns that are observed between radiation reflected directly on the air–SiO_2-layer interface and radiation reflected on the gold mirror demonstrate the better response of our antenna to substrate-side illumination. They are described in Section 4. Alternatively, our high-frequency mixing experiments described in Section 6 have been performed by irradiation of the thin-film Ni–NiO–Ni diode through our Si/SiO_2 substrate.

The radiation pattern of an antenna on a substrate has been investigated theoretically and experimentally. For example, Brewitt-Taylor et al. [38] evaluated numerically the radiation pattern of a resonant dipole antenna on a substrate. Similar patterns have been calculated for a horizontal infinitesimal dipole by Engheta et al. [42,43] and for a current element at an air–dielectric interface by Rutledge and Muha [41]. The patterns are determined in two orthogonal planes, i.e., the E and the H plane defined by the axis of the dipole antenna (inset of Fig. 5): The E plane is perpendicular to the substrate and contains the elementary dipole. The H plane is normal to the dipole [40]. Rutledge and Muha [41] calculated the far-field power density S_{H} in the dielectric for the H plane at a distance r as

$$S_{\mathrm{H}}(\theta_{\mathrm{d}}) = \alpha n \left(\frac{n \cos\theta_{\mathrm{d}}}{|\cos\theta_{\mathrm{a}} + n\cos\theta_{\mathrm{d}}|} \right)^2$$

$$\text{with } \alpha \equiv \left(\frac{\omega\mu_0 I h}{4\pi r} \right)^2, \qquad (2.6)$$

where n is the refraction index of the substrate, θ_{a} the angle of incidence in the air and θ_{d} the refracted angle in the substrate. The current element is described by its amplitude I, its length h and its frequency ω. The similar calculation for the E plane yields

$$S_{\mathrm{E}}(\theta_{\mathrm{d}}) = \alpha n \left| \frac{n\cos\theta_{\mathrm{a}}\cos\theta_{\mathrm{d}}}{n\cos\theta_{\mathrm{a}} + \cos\theta_{\mathrm{d}}} \right|^2. \qquad (2.7)$$

These patterns are represented in Fig. 5 as a function of the incidence angle in the air. This angle

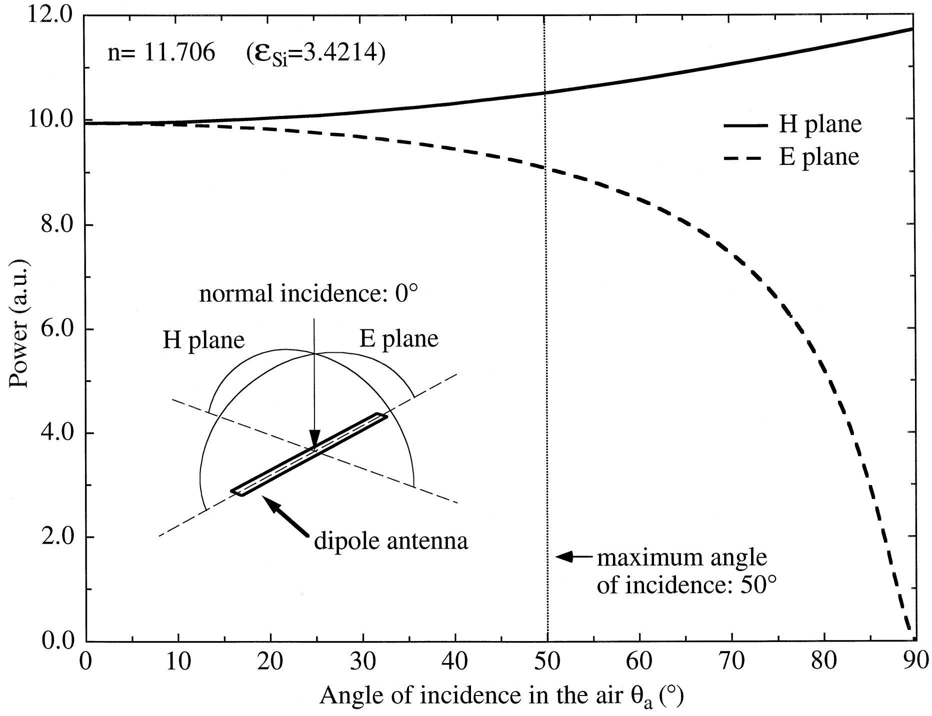

Fig. 5. Radiation pattern in the dielectric of a current element on a dielectric substrate.

is relevant in our experiments. These plots correspond to the representations of the above references only for angles in the dielectric that are below the critical angle of total reflection in the substrate.

Measurements have been made for a bow-tie antenna by Rutledge and Muha [41] and for a spiral antenna by Grossman et al. [44]. All the radiation patterns give confirmation that the antennas are considerably more sensitive to radiation coming from the substrate side and by reciprocity that most of the power is radiated into the substrate. However, the antenna patterns of our different antennas have been only measured up to a maximum angle of incidence in the air of about 50°, as indicated in Fig. 5, because of the presence of bonding wires. In this interval, the interferences in the substrate have a significant influence on the response of our diode and partially mask the radiation pattern of the antenna as demonstrated in Section 4.

The velocity of the current waves in an antenna on a dielectric substrate with permittivity $\varepsilon_{\mathrm{subst}}$ is calculated with the aid of the effective relative electric permittivity $\varepsilon_{\mathrm{eff}}$ of the system

$$v = \frac{c}{\sqrt{\varepsilon_{\mathrm{eff}}}}. \tag{2.8}$$

For an antenna on a substrate in the millimeter-wave range, this effective permittivity is well approximated by the quasi-static value ε_{q} calculated for zero frequency [40]:

$$\varepsilon_{\mathrm{q}} = \varepsilon_{\mathrm{eff}}(\nu = 0) = \frac{\varepsilon_{\mathrm{subst}} + 1}{2}. \tag{2.9}$$

For frequencies higher than a few GHz, the range of validity of the quasi-static approximation is exceeded. Under these circumstances the frequency dispersion of the effective permittivity must be taken into account. The analogy between integrated transmission lines and antennas permits the transfer of the dispersion characteristics of coplanar transmission lines to integrated antennas. For example, a bow-tie antenna or a spiral antenna can be transformed by the appropriate conformal mappings into coplanar transmission lines as presented below in Sections 2.2.3 and 2.2.4. An analytical expression of the frequency dependence of the effective permittivity for a coplanar waveguide and for coplanar strips has been derived by Hasnain et al. [45] on the basis of the empirical formula for the microstrip dispersion and verified in the terahertz range by Frankel et al. [46]. The effective permittivity $\varepsilon_{\mathrm{eff}}(\nu)$ as a function of the frequency ν is given by the expression

$$\sqrt{\varepsilon_{\mathrm{eff}}(\nu)} = \sqrt{\varepsilon_{\mathrm{q}}} + \left(\frac{\sqrt{\varepsilon_{\mathrm{subst}}} - \sqrt{\varepsilon_{\mathrm{q}}}}{1 + A\left(\dfrac{\nu}{\nu_{\mathrm{TE}}}\right)^{-1.8}} \right). \qquad (2.10)$$

In this equation A is a parameter related to the waveguide geometry. It has been estimated numerically by Hasnain et al. [45]. The frequency ν_{TE} is the surface wave TE_1 mode cut-off frequency that has the following dependence on the substrate thickness d:

$$\nu_{\mathrm{TE}} = \frac{c}{4d\sqrt{\varepsilon_{\mathrm{subst}} - 1}}, \qquad (2.11)$$

where c represents the velocity of light in vacuum. The cut-off frequency ν_{TE} is approximately 60 GHz for our 385-μm silicon substrate. The dispersion curve looks similar to those of microstrip lines [47]. It is represented in Fig. 6. The effective permittivity $\varepsilon_{\mathrm{eff}}$ for coplanar waveguides varies from the quasi-static value at zero frequency to the asymptotic value $\varepsilon_{\mathrm{subst}}$ for infinite frequency with an inflection point typically between 10 GHz and 1 THz depending on the geometry of the antenna or transmission line. The antennas connected to our MOM diodes are optimized for 10.6-μm infrared radiation with a frequency of about 28 THz. In this range the effective relative electric permittivity $\varepsilon_{\mathrm{eff}}$ seen by a wave propagating on the antenna is well approximated by the substrate permittivity $\varepsilon_{\mathrm{subst}}$ corresponding to the

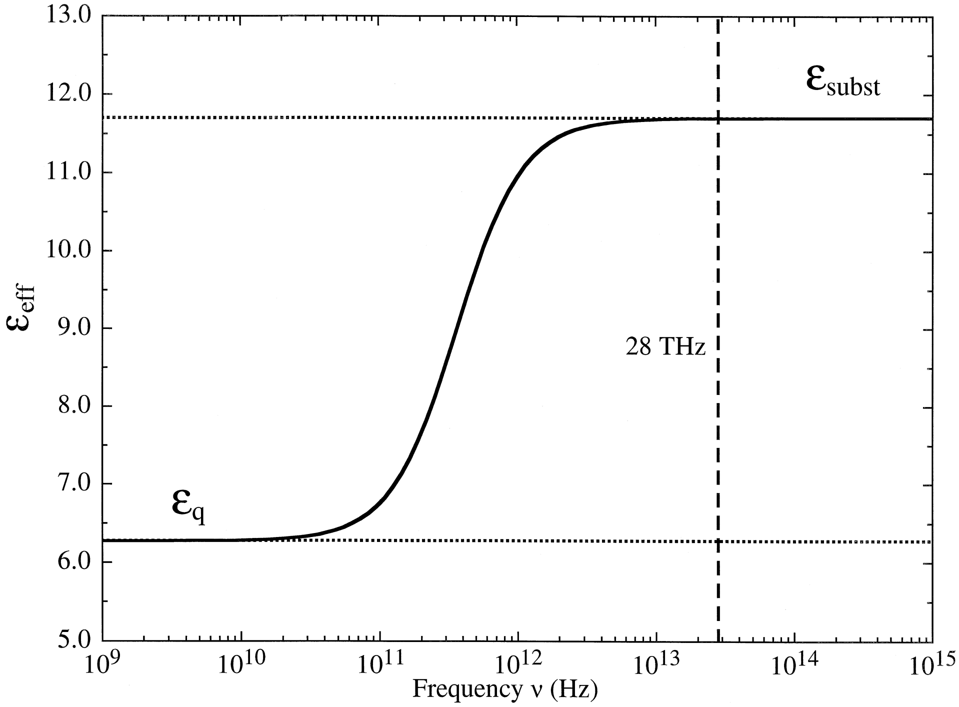

Fig. 6. Frequency dependence of the effective permittivity of a coplanar waveguide.

asymptotic permittivity for infinite frequency as apparent in Fig. 6. This has been confirmed by our detection experiment performed with dipole antennas.

2.2.2. Dipole antennas

Thin-film Ni–NiO–Ni diodes connected to dipole antennas have been extensively studied by Wilke et al. [18,19]. The detected signals as a function of the antenna length have been compared with the theoretical far-field distribution of a thin center-fed linear antenna, where the antenna current distribution is assumed to be sinusoidal. A first resonance was observed for an antenna length $L = 3.1$ μm corresponding to the substrate wavelength of the incident infrared radiation. Higher-order resonances were also observed yet they are weaker than the first full-wave dipole resonance. This is explained by the attenuation of the antenna currents characterized by the measured coefficient $\Gamma = 0.15$ $\mu\mathrm{m}^{-1}$. We assume the same coefficient for the attenuation on the other types of antennas investigated in this study because of the analogy of materials, fabrication processes, and structure dimensions.

The dc response of the diodes consists of a polarization-dependent part due to antenna coupling and a polarization-independent part mainly of thermal origin. The highest signal is measured for the linear polarization parallel to the antenna axis. The polarization-dependent part of the response as a function of the linear polarization angle is well approximated by a squared cosine, in agreement with antenna theory.

2.2.3. Bow-tie antennas

The radiation characteristics and the impedance of thin dipole antennas are extremely sensitive to frequency. The bandwidth of the dipole antenna is limited for narrow dipoles. A slight wavelength variation or a small inaccuracy in the manufacture of the resonant dipole gives rise to parasitic capacitances and inductances. For our CO_2-laser infrared radiation with a wavelength of 10.6 μm, resonant dipole antennas at the corresponding wavelengths in the dielectric are difficult to manufacture with the precision achieved by electron-beam lithography. The solution to this problem is a broadband antenna. If the width d of the arms of a dipole antenna is increased above the standard limit $d > 0.05\lambda$, the current distribution shows a deviation from the idealized sinusoidal distribution [48]. A broad-band antenna as used at millimeter and submillimeter wavelengths is the bow-tie antenna or triangular antenna because of its simple design (Fig. 7). Its triangular structures can be considered as tapered dipole arms. The impedance of an infinite bow-tie antenna depends only on its flare angle ϕ defined in Fig. 7, yet not on the frequency. A method of calculating this impedance relies on conformal mappings that transform a two-dimensional boundary problem into a simpler equivalent problem. The conformal transformation $z = \ln(w)$ maps radial lines in the w plane

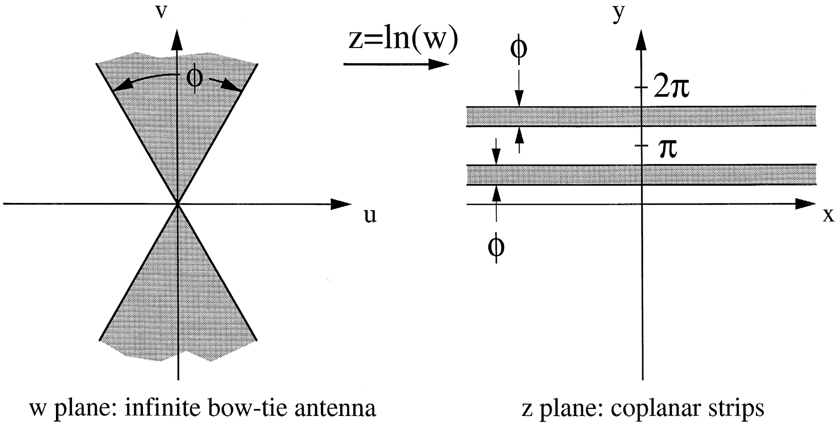

Fig. 7. Conformal mapping of a bow-tie antenna.

onto horizontal lines in the z plane. This yields the representation of Fig. 7 where a bow-tie antenna is transformed into coplanar strips [49,50]. The impedance of the infinite bow-tie antenna is then derived from the characteristic impedance of coplanar strips. The result is [51,52]:

$$Z_{\text{ant}} = \frac{\eta_0}{2}\sqrt{\frac{1}{\varepsilon_{\text{eff}}}}\,\frac{K(\cos(\phi/2))}{K(\sin(\phi/2))}. \tag{2.12}$$

$K(k)$ is the complete elliptic integral of the first kind [53], η_0 the free-space impedance and ε_{eff} the effective dielectric constant which at infrared frequencies close to 30 THz equals the dielectric constant of the substrate $\varepsilon_{\text{subst}}$. We have chosen the flare angle $\phi = 60°$ because the theory predicts an impedance in the range of 70 Ω for this angle. This impedance is in the order the average zero-bias resistance of our diodes. The ratio of these resistances is not 1:1 yet larger than 1:2 for all diodes. Thus the matching of the antenna to the load is sufficient [35]. For a bow-tie antenna of finite size, reactive components appear in the impedance that depends on the length $L/2$ of the arms of the antenna defined in Fig. 8. The dependence of the reactance of such an antenna, i.e., a triangular unipole on this length was measured by Brown and Woodward [54]. The resonances occur for lengths where the reactance equals zero. In our configuration they correspond to arm lengths of approximately 0.5 μm and 1.06 μm for the first and the second resonance according to Fig. 28 of Ref. [54]. The resolution of the electron-beam lithography implies a lower limit to the dimension of the structure. Consequently, we have manufactured bow-tie antennas with an arm length corresponding to the third resonance that occurs approximately at $L/2 = 1.90$ μm (Fig. 8). A more recent experiment by Compton et al. [55] who worked with a frequency of 94 GHz showed that the dominant modes of a 60° bow-tie antenna on a substrate propagate with the wave number of the dielectric bulk. By taking account of these results, we manufactured bow-tie antennas with arm lengths of $L/2 = 2.3$ μm and $L/2 = 3.9$ μm, corresponding to overall lengths L of $3/2$ and $5/2$ times the wavelength in the dielectric bulk of our 10.6-μm laser radiation (Fig. 8). We did not fabricate antennas with longer arms because of the high attenuation of the antenna currents in the antenna arms which are described in Section 2.2.2 for the case of dipole antennas. For the same reason, the form of the arm caps does not affect the impedance. Therefore we chose a simple triangular end.

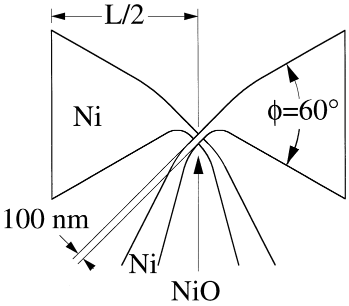

Fig. 8. Survey of a bow-tie antenna with arm length L/2. We have manufactured three different antennas with the lengths L/2 = 1.9 μm, 2.3 μm and 3.9 μm.

2.2.4. Spiral antennas

Antennas with a shape specified only by angles possess frequency-independent impedance and radiation patterns. This is the Rumsey principle introduced in the 1950's [56]. This property originates in the fact that the scaling caused by changing the wavelength corresponds to a rotation of the antenna by the appropriate in-plane angle. This presupposes that the antenna extends to infinity. In practical designs, the corresponding finite structures exhibit practically frequency independent properties over a large bandwidth. An example of these broad-band structures is the planar two-arm logarithmic spiral antenna. It has been studied at millimeter and microwave wavelengths [57–59]. Outside the feed region, the logarithmic spiral is defined in polar coordinates $(r;\phi)$ by the general equation [57]

$$r = r_0 \exp(\phi \ln a) = r_0 a^{\phi}. \tag{2.13}$$

where r_0 and a are positive constants that determine the radius of the inner structure and the tightness of the spiral. In order to generate a self-complementary spiral antenna we have designed four spirals with relative rotations of $\pi/2$

$$r_1 = r_0 a^{\phi},\ r_2 = r_0 a^{\phi-\pi/2},\ r_3 = r_0 a^{\phi-\pi},$$
$$r_4 = r_0 a^{\phi+\pi/2}. \tag{2.14}$$

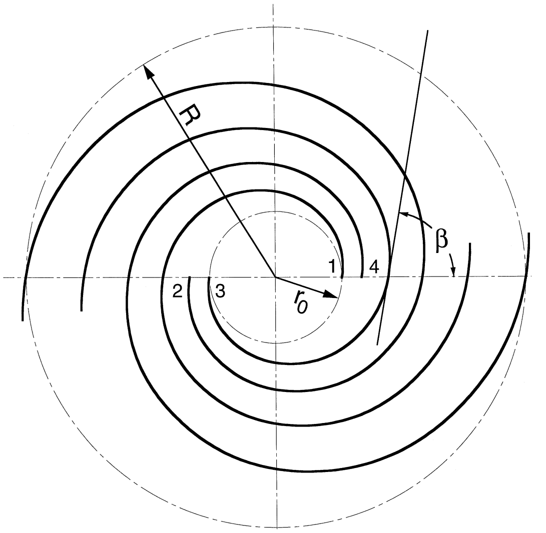

Fig. 9. Spiral structure of the antenna outside the feed region.

The antenna consists of metallized areas between spirals 1 and 4 and spirals 2 and 3 (Fig. 9). The curvature of the spiral causes an attenuation of the antenna current that decreases more rapidly than $1/r$ [60]. Thus, the structure can be truncated at the outer radius R determined by the desired bandwidth with practically no effect on the properties of the antenna. The outer radius R of the truncated spiral gives the low-frequency limit of the antenna and is commonly accepted to be [48]

$$R = \lambda/4. \tag{2.15}$$

Our maximal free-space wavelength of 11 μm yields an outer diameter $2R$ of 5.5 μm for our spiral antenna. It should be noted that this value is considerably larger than the wavelength in the dielectric bulk of 30 THz infrared radiation which plays the dominant role in antenna coupling. Therefore the outer diameter $2R = 5.5$ μm of our spiral antenna is sufficient. The inner diameter yields the high-frequency limit of operation and is determined by the dimensions of the feed structure. For our infrared antennas connected to thin-film MOM diodes, the resolution of the electron-beam lithography requires a terminal inner structure that stretches over the standard $\lambda/10$ limit of the feed diameter [48]. The consequence of an oversized center structure is an elliptical polarization different from the circular polarization expected for a spiral antenna. However, for lithographic spiral antennas with an inner radius corresponding to one quarter of the quasistatic wavelength, Grossman et al. [44] report detection of 10-μm radiation with almost circular polarization. For normal incidence, a ratio of response to orthogonal polarizations of 1.35 dB was measured. In our case, the inner radius r_0 was minimized to one quarter of the effective wavelength of 9.8-μm infrared radiation

$$r_0 = \frac{\lambda_{\text{eff}}}{4} = \frac{\lambda_0}{4\sqrt{\varepsilon_{\text{eff}}}} \approx 0.73\ \mu\text{m with } \varepsilon_{\text{eff}} = 11.7. \tag{2.16}$$

The values of the inner and outer radii permit the determination of the constant a in the spiral Eq. (2.14). For a one-turn spiral, the conditions yield

$$r_1(0) = r_0 \text{ and } r_4(2\pi) = R. \tag{2.17}$$

This results in the following parameters of the spiral

$$r_1 = 0.73\ \mu\text{m and } a = \left(\frac{R}{r_0}\right)^{\frac{2}{5\pi}} = 1.184. \tag{2.18}$$

The tightness of a spiral antenna can also be specified by the wrap angle β that corresponds to the angle between a line tangential to the spiral and a radial line from the origin (Fig. 9). It can be evaluated according to [48]

$$\beta = \arctan\frac{1}{\ln a} = 80.41°. \tag{2.19}$$

According to the Babinet principle for complementary antennas (Ref. [61], Section. 11.8; Ref. [51]) the theoretical characteristic impedance of an infinite self-complementary antenna in free-space is real and equal to half the intrinsic impedance of vacuum $Z_0/2 \approx 188\ \Omega$. However, for finite spiral antennas the measured impedances are lower, i.e., in the range of 50 to 120 Ω, depending on arm width and thickness, substrate and feeding structure. For a planar self-complementary structure on a substrate we approximate the characteristic impedance by

$$Z_{\text{ant}} = \frac{Z_0/2}{\sqrt{\varepsilon_{\text{eff}}}} \approx \frac{Z_0/2}{\sqrt{\varepsilon_{\text{subst}}}}. \tag{2.20}$$

For an antenna for 30-THz radiation on a silicon substrate, this equation yields a characteristic impedance of about 55 Ω. However, it is probably too low if we take into account that narrow-arm structures should have higher impedances. Consequently, the impedance of our integrated spiral antennas approximately matches the impedance of our diodes.

Eq. (2.20) can also be derived using conformal mapping. The conformal transformation $z = \ln(w)$ previously applied to the bow-tie antenna, maps a self-complementary logarithmic antenna into oblique coplanar strips, with a strip width equal to the center-slot width as represented in Fig. 10 [50,62]. The calculation of the characteristic impedance results in Eq. (2.20) because of the properties of these particular coplanar strips.

The radiation pattern of a planar spiral antenna in free space exhibits a main lobe perpendicular to the antenna plane and a rotational symmetry. The main beamwidth is dependent on the tightness of the spiral and on the number of turns [57,63]. The substrate has a similar influence on spiral antennas as on dipole antennas [44,64].

The polarization of the antenna is circular over the antenna bandwidth in practically all directions [65]. The increase of the angle of incidence introduces only a slight elipticity of the polarization. A linear polarization should be detected independently of the polarization angle with a loss of 3 dB with respect to the detection of appropriate circular polarized radiation. A spiral antenna is unable to detect its own radiation reflected by a mirror, since the sense of polarization is reversed by reflection (Ref. [66], Chapt. 23-10).

3. Manufacture and testing of the thin-film Ni–NiO–Ni diodes

In this section, the fabrication, mounting and electrical testing of the thin-film Ni–NiO–Ni diodes are presented. In the first part, the technique of the manufacture of the nanometer-scale contact structures with electron-beam lithography is described, while the second part deals with the specific problem of forming the shape of the logarithmic spiral antenna by this technology. Subsequently, two different types of electrical connections between diodes and electronic devices are presented. This is followed by the discussion of the measurement of the electrical characteristics of the thin-film diodes which determine detection and mixing of infrared radiation. This permits a first qualitative control of the fabrication process. The results of this measurement are summarized in the final part of this section.

3.1. Electron-beam lithography

The requirement of small contact areas for our thin-film Ni–NiO–Ni diodes for a fast response cannot be fulfilled by conventional photolithography techniques. Therefore, the metal strips with a minimum width of about 110 nm have been produced by

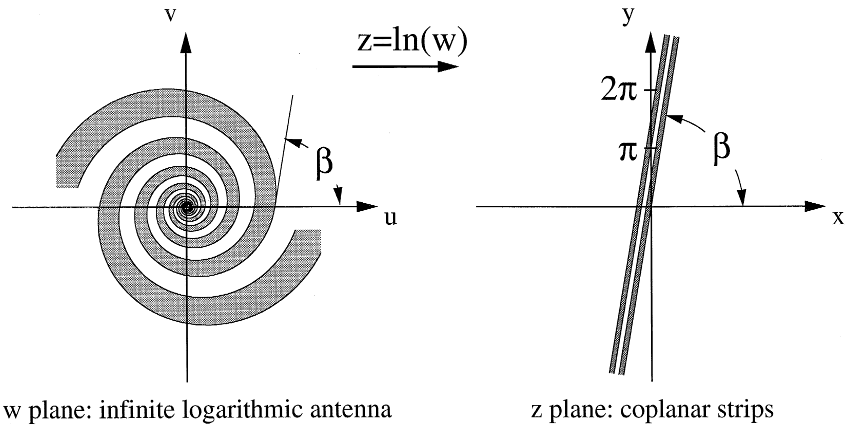

Fig. 10. Conformal mapping of a spiral antenna.

high-resolution electron-beam lithography at IBM Research Laboratory Rüschlikon. Details of this technology are found in Ref. [67]. The diode, the antenna and the connections to the diodes are written by an electron beam controlled by a computer in an area around the diode with a radius of approximately 100 μm. The two overlapping Ni layers of 2200 Å are sputtered as two separate depositions of Ni. The photoresist is removed by a conventional lift-off process. The precise alignment of the second Ni layer is performed with the help of previously written markers. The metal-oxide layer is sputtered after the deposition of the first antenna arm and before the deposition of the second antenna arm. Extremely thin insulating oxide layers of a few tens of angstroms between the two Ni layers are required for the tunneling process because of the exponential decrease of the tunneling currents for increasing barrier thickness [21]. The NiO-layer thickness is measured during sputtering by a quartz oscillator. Thus, layers of about 35 Å are manufactured. They represent a compromise between the high responsivity of thin layers and the robustness of thick layers. The dielectric properties of NiO thin films have been described in detail by Rao and Smakula [68], Fuschillo et al. [69,70], and Mochizuki [71]. The structure of the contact is apparent on the electron micrograph of Fig. 11. This picture of a Ni–NiO–Ni diode with an integrated bow-tie antenna is taken with an angle of incidence of 45° that permits to show how the layers overlap and thus produce the contact. Fig. 12 represents a schematic cross section of the contact with the indication of the thickness of the different layers.

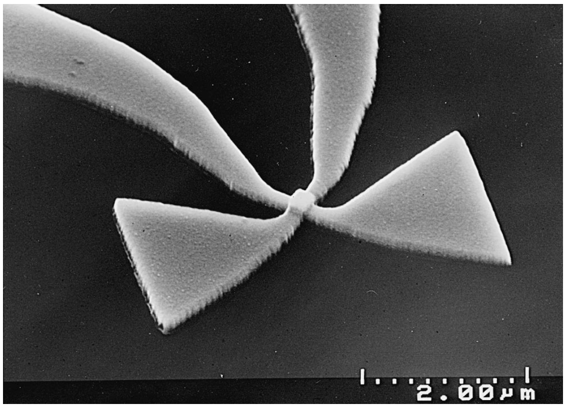

Fig. 11. Electron-microscope image of the thin-film Ni-NiO-Ni diode with integrated bow-tie antenna taken at 45° incidence.

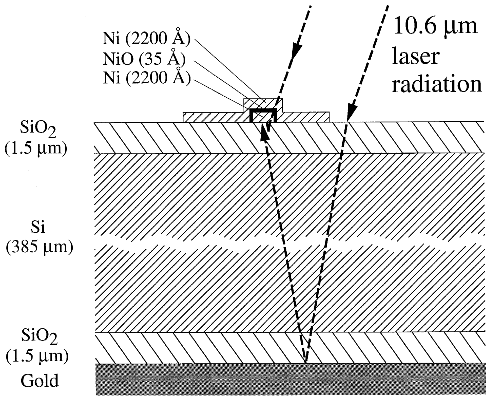

Fig. 12. Schematic cross section of Ni-NiO-Ni MOM diode.

The diodes are fabricated on a silicon substrate that is also represented in Fig. 12. The bulk silicon is n-doped with phosphorus. Its resistivity is 3–5 Ω cm. The wafers, with a thickness of 385 μm, are polished and covered on both sides with 1.5-μm SiO_2 layers produced in a standard oxidation oven. This layer isolates the diode from the semiconducting silicon thus preventing the formation of a Schottky contact. In addition, these layers act as anti-reflection coatings and increase the transmission of radiation through the silicon substrate up to about 80% at wavelengths near 10.7 μm. The measured transmissions of the coated and uncoated Si substrates have been published by Wilke et al. [19]. The chip supporting the diodes is either mounted on a gold socket, or its back side is coated with a gold mirror. This improves the coupling efficiency of the antenna (Section 2.2.1).

3.2. Manufacture of the spiral antennas

Electron-beam lithography systems traditionally approximate a structure by a set of trapezoidal shapes. Our spiral antennas represent an unconventional geometry that cannot be approximated by polygons with a sufficient fidelity to the original design, because of the small dimensions of the antennas. Recently, a new set of conic-based primitives was added to the basic set [72]. This offered the possibility to generate structures bounded by circles and ellipses. It allowed the manufacture of the small logarithmic spiral antenna with an outer diameter of 5.5 μm presented in Section 2.2.4. The basic primitive structures used for this purpose are bounded by two quarters of ellipses (inset of Fig. 13). The determination of the bounding quarters of ellipses for each primitive structure was performed as illustrated in Fig. 13: On each spiral curve two following points p_{i-1} and p_i with horizontal and vertical tangents are determined and chosen as ends of a quarter of an ellipse. The Cartesian coordinates of these two points, which also possess horizontal and vertical tangents on the ellipse, permits the determination of the center c_i and the principal axes of the ellipse. The spiral is then approximated with four such decentered quarters of ellipses. Outside the feed region, this combination of quarters of ellipses matches well the desired logarithmic spiral form, because of the abundance of points with identical tangents common to this curve and its approximation.

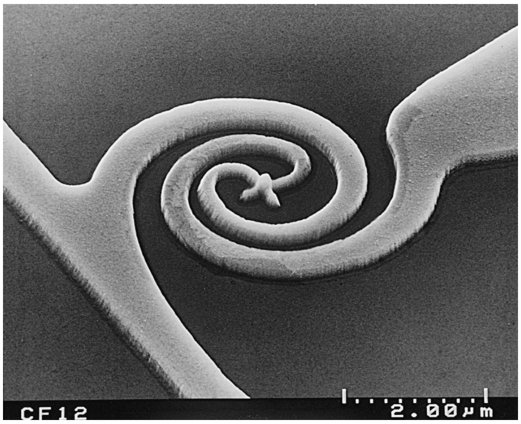

Fig. 14. Electron micrograph of the spiral antenna.

The Ni–NiO–Ni diode is positioned at the coincident origins of the logarithmic spirals. The minimum width of the contact structure is, as for the bow-tie antennas, in the range of 110 nm as shown on the electron micrograph of Fig. 14. The connection between contact and spiral antenna is also designed with circles and ellipses. The 90° intersection of the antenna arms at the diode is used to relax the tolerance for the relative positions of the two arm depositions. As demonstrated in Section 4, this asymmetric feed region introduces a polarization-dependent antenna responsivity that differs from the circular polarization expected for a symmetric spiral.

Two types of antennas have been manufactured with identical structure dimensions, yet with an opposite wiring sense of the spiral. A mirror symmetry

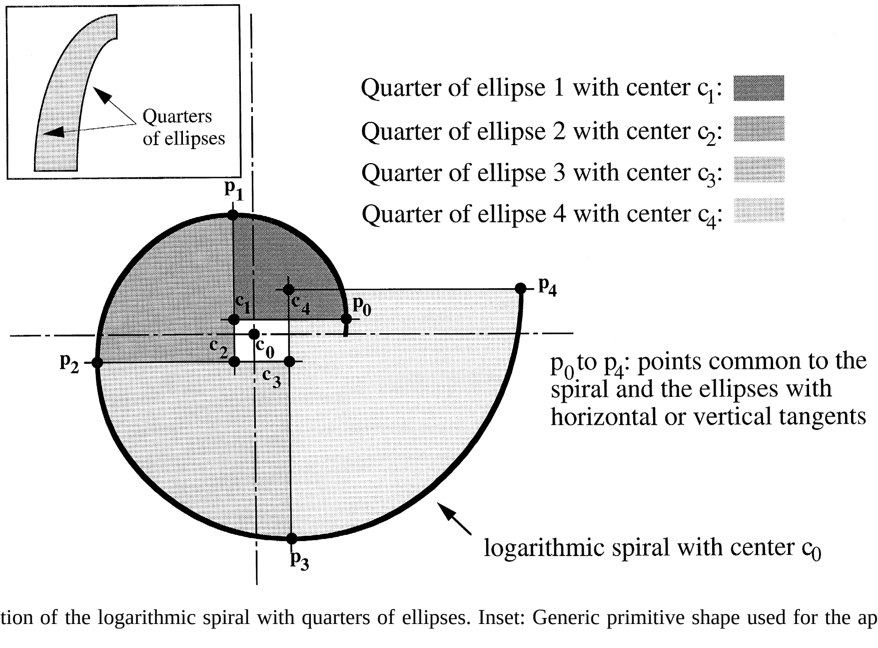

Fig. 13. Approximation of the logarithmic spiral with quarters of ellipses. Inset: Generic primitive shape used for the approximation of the spiral antenna.

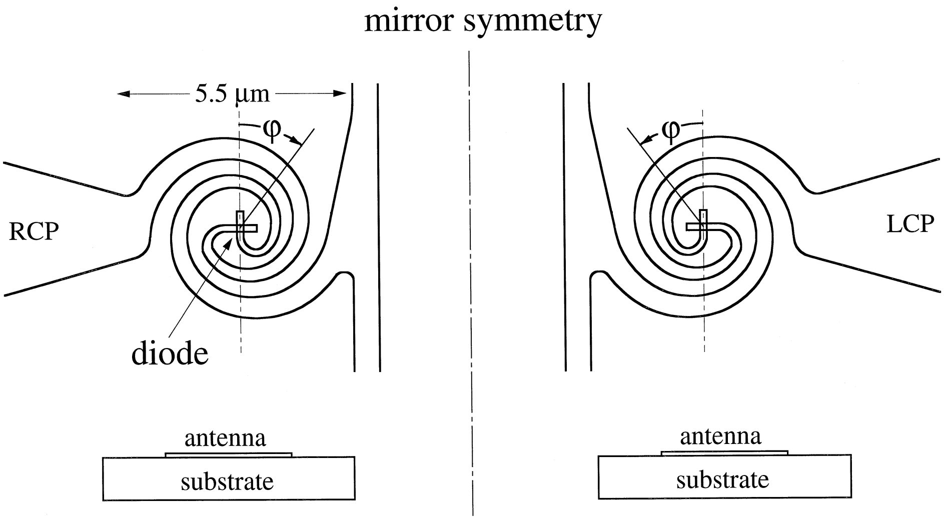

Fig. 15. Right and left circular integrated spiral antennas.

relates the two structures (Fig. 15). Two definitions of circular polarization coexist. They rely either on an emitting or a receiving antenna. Here, we adopt the IEEE definition, where for an observer looking in the direction of propagation, the right-hand polarization rotates clockwise [66]. The right-hand spiral antenna represented in Fig. 15 is then defined as right-circularly polarized (RCP) antenna for the radiation outward from the page, and the left-hand antenna as left-circularly polarized (LCP) antenna.

By considering the spiral antenna from the substrate side rather than from the air side the polarization of the receiving antenna takes the opposite sense. For the configuration of our integrated spiral antennas, this is counterbalanced by the fact that the reflection at the back side of the substrate that supports the antenna changes the sense of circularly-polarized radiation [73]. As a consequence an antenna matched to right-circularly polarized radiation incident from the air side is also matched to the reflected left-circularly polarized radiation incident from the substrate side.

3.3. Signal transmission

The thin-film Ni–NiO–Ni diodes have to be electrically connected to external electronics for signal readout and bias-voltage supply. The small size of diode and antenna requires a compromise between a good electrical connection and a metallic configuration that does not electrically affect the antenna. Two different types of connections to the diodes have been used depending on the nature of the signals. The detection of dc signals generated in the diode by the rectification of antenna currents requires only the simple configuration described first in Section 3.3.1. The transmission of high-frequency mixing signals and the detection of short pulses requires microwave transmission lines that are then presented in Sections 3.3.2 and 3.3.3.

3.3.1. Configuration for detection of cw radiation

The diodes are located on a substrate sawed as 3 mm × 3 mm chips. Outside the region defined by electron-beam lithography, the gold or rhodium connections to bonding pads are fabricated by standard photolithography techniques. The electron micrograph of Fig. 16 shows the transition that consists of an overlapping region of the nickel and the gold or rhodium layers. The Ni–NiO–Ni diode with an integrated bow-tie antenna is located in the center of the picture. Two different configurations of these leads on the chip have been applied. The first has been used before by Wilke et al. [19] to contact ten diodes with integrated dipole antennas on a chip with a common grounded central gold electrode (Fig. 17). The second was developed for diodes integrated with spiral antennas and then applied to diodes integrated

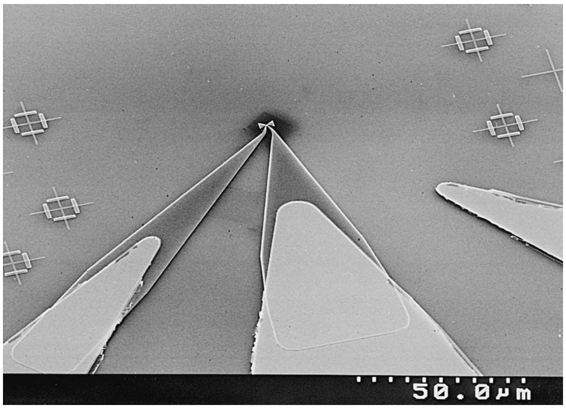

Fig. 16. Transition between the nickel leads manufactured by electron-beam lithography with photolithographic gold electric leads.

with bow-tie antennas. The left-hand side of Fig. 18 shows the design of this structure on a chip with six diodes indicated by circles. This configuration that makes use of rhodium layers is mainly adapted to transmission of high-frequency mixing signals as described in Section 3.3.3. In the detection experiments, however, no difference between the two configurations was found since in the vicinity of the antenna the tapered connections are in both cases sufficiently thin to avoid a dramatic distortion of the electric fields. The chips are mounted on gold TO5 sockets, while the connections are made by bonding wires of gold.

3.3.2. Configuration for high-frequency mixing and pulse detection

Mixing experiments and short pulse measurements demand connections to the MOM diode that transmit high-speed signals with minimal losses. The simple mounting on a socket applied to the dc detection experiments is not appropriate for this purpose. We therefore made use of microwave transmission lines, which operate at least up to 60 GHz to permit the transmission of a mixing signal of two adjacent transitions of the CO_2-laser spectrum in the 10P-branch.

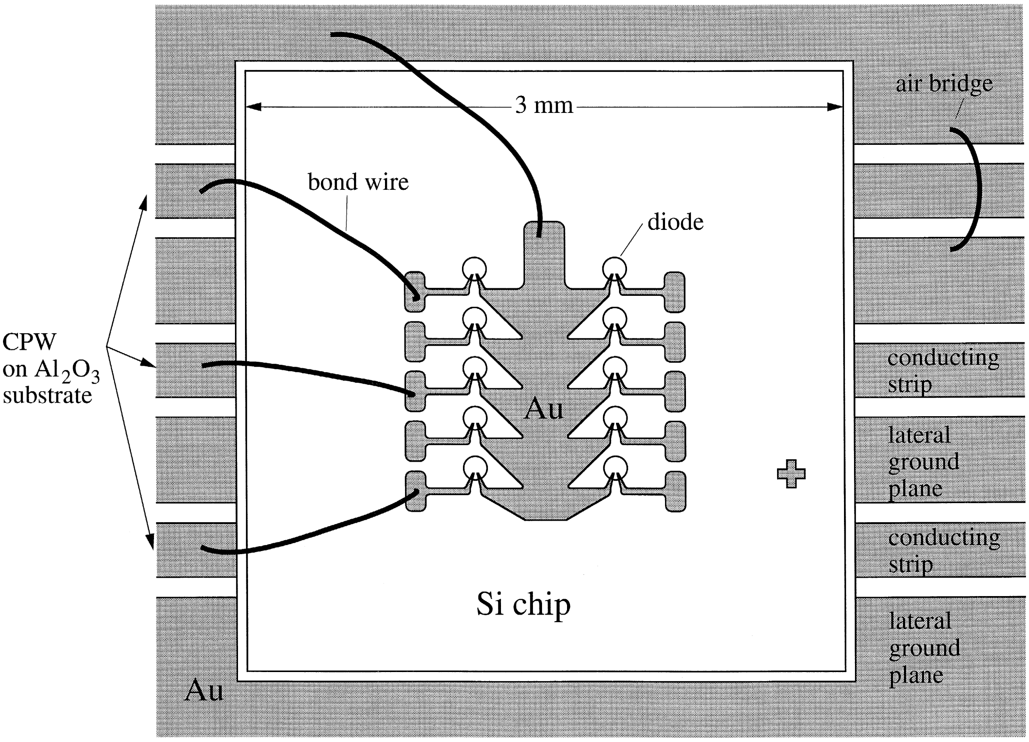

Fig. 17. Chip design for bonding-wire connections.

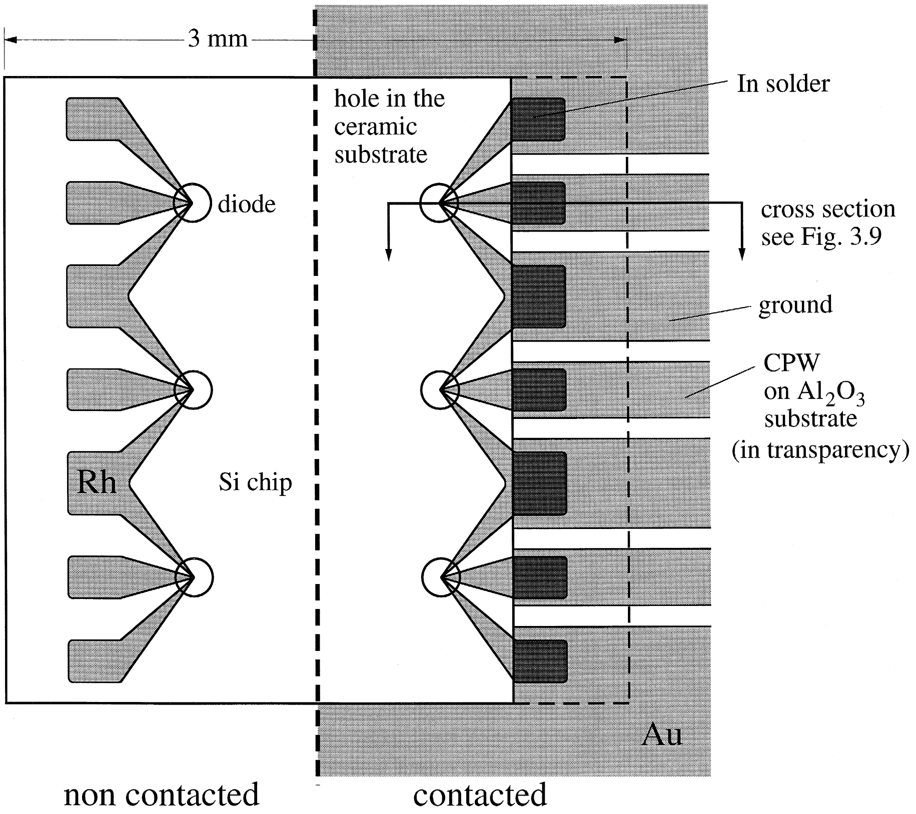

Fig. 18. Schematic drawing of the electric connections to the diodes. Left side: Chip design. Right side: Flip-chip connections to coplanar waveguides on a ceramic substrate.

The first configuration used is presented schematically in Fig. 17. The signals produced by the diode are transmitted from the structure on the chip by means of bonding wires to coplanar waveguides (CPW) (see, e.g., Ref. [74]). These structures consisting of a central conducting strip with two coplanar parallel grounds are produced by conventional photolithography techniques on a 0.5 in. × 1 in. ceramic substrate. In order to suppress losses due to surface waves, a thin Al_2O_3 substrate with a relative electric permittivity ε of about 10 in the microwave region and a thickness of 254 μm was chosen. This yields a cut-off frequency n_{TE} of about 98 GHz for the surface wave TE_1 mode according to Eq. (2.11). The characteristic impedance of the coplanar waveguide was calculated with the analytical formulas given by Ghione and Naldi [75]. With these quasistatic expressions, a characteristic impedance of 50 Ω for frequencies up to at least 60 GHz is obtained with an accuracy of a few percent for a strip width of 0.27 mm and slot width of 0.10 mm. Bonding wires have been used as air bridges that keep the two lateral ground planes of the CPW at the same potential. These air bridges separated by a distance smaller than half a wavelength of the highest operating frequency of the circuitry suppress the parasitic odd mode or slot mode [76] that can be excited strongly by any discontinuity of the CPW, such as a bend or a slight asymmetry. The Al_2O_3 substrate is mounted in a metallic housing. The transitions to high-frequency semirigid coaxial cables (Wiltron-V) are made with spark-plug launchers (Wiltron-V102F) operating up to 65 GHz.

The electrical properties of the system have been tested with a network analyzer. For this purpose, a test chip with a straight transmission line replaces the chip with the diodes. Transmission and reflection measurements have been performed for frequencies up to 60 GHz. For this configuration we estimated a minimal amount of loss of 13 dB at 50 GHz. In addition strong resonances are observed. Due to the chip geometry with a central ground electrode, it was expected that the actual losses are more dramatic than with the straight line transmission lines of the test chip.

The main cause of these relevant losses at high frequencies stems from the connections with bonding wires, because they represent parasitic inductors. In order to obtain relatively flat bonding wires and to minimize their length, the silicon chip supporting the diode was mounted into a hole in the ceramic substrate, so that both metallizations were located at the same level. However, in this configuration, a bonding wire causes a loss of approximately 7 to 8 dB at 50 GHz. Another important source of loss at high frequency originated in the use of silicon substrates with a low resistivity of 3 to 5 Ω cm. In order to minimize the substrate loss of the circuitry, silicon with a resistivity of several kΩ cm is used in high-frequency applications [77].

We have applied this configuration for pulse-detection experiments (Section 5) and for our first mixing experiments performed at LENS (Florence, Italy) (Section 6.1 and Ref. [78]) that resulted in the measurement of difference frequencies up to 85 MHz. Mixing with higher difference frequencies in the order of 60 GHz could not be achieved. This demonstrated the need for improvement of the contacting structures.

3.3.3. Improvement of the high-frequency configuration

For the second mixing experiments, which have been performed at the PTB (Braunschweig, Germany), the bond-wire connections to the diodes were replaced by the flip-chip connections schematically depicted in Fig. 18 and Fig. 19. The Ni–NiO–Ni diodes are connected to coplanar rhodium waveguides as shown in Fig. 18 for the three diodes on the left-hand side of the chip. After the manufacture of the diode, antenna and rhodium waveguide, the chip is flipped over and soldered at a temperature of 180°C to the previously mentioned 50-Ω gold CPW on a ceramic (Al_2O_3) substrate by indium solder bumps. The precise location of these tiny bumps on the metal parts of the CPW was achieved with the help of a molybdenum mask after a careful alignment. As before, the connection of the CPW to a

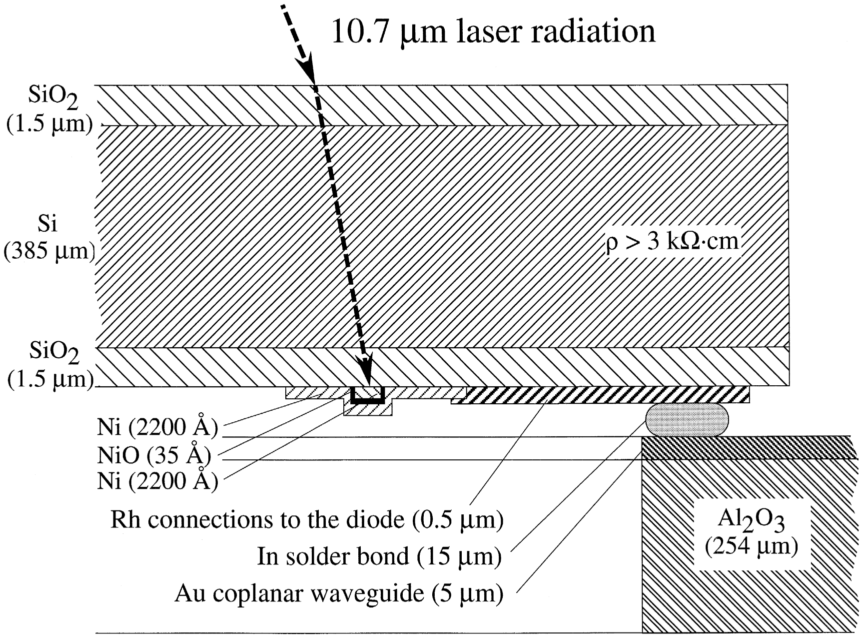

Fig. 19. Schematic cross section of a Ni-NiO-Ni diode and its connections (not to scale).

semirigid coaxial cable was made with spark-plug launchers (Wiltron-V102) screwed into the housing that encloses the circuit. The thickness of the different layers is also indicated in Fig. 19. Rhodium was used instead of gold for the waveguides on the silicon chip because of its thin-film compatibility with indium [79]. In previous attempts with gold waveguides on the chip, the applied 0.5-μm gold layer was completely dissolved by the indium solder. This effect is not observed for the gold CPW on ceramic substrates because of the considerably thicker applied Au layers. The flip-chip configuration has two decisive advantages: First, it guarantees an excellent electrical high-frequency connection to the diode and, secondly, it permits the irradiation of the antenna from the substrate side as represented in Fig. 19. This takes advantage of the higher sensitivity of an antenna to the radiation incident from the substrate [38]. The irradiation from the side of the SiO_2-coated substrate can be applied because of the 80% transmission of 10.7 μm radiation.

Contrary to our previous diodes, the diodes used for these second mixing experiments are supported by a high-resistivity ($\rho > 3$ kΩ cm) silicon substrate. By application of this high-resistivity substrate we minimize the substrate losses in the microwave range [77] and thus reduce the attenuation of antenna currents at infrared frequencies.

3.4. Electrical characteristics of the MOM diodes

MOM diodes are capable of rectification and mixing of infrared radiation because of their nonlinearity. The detection signals are proportional to the second derivative of the current–voltage characteristics $I(V)$ while mixing is determined by its derivative corresponding to the mixing order. The measurement of the second derivative of the $I(V)$ curve of a diode as a function of the bias voltage permits a first characterization of its nonlinearity. The simultaneous measurement of zero-bias resistance of the diode gives information on the thickness of the NiO layer and the size of the contact area.

3.4.1. Experimental arrangement

The electrical measurements of the MOM diodes have been described by Wilke et al. [18]. They are performed with the inelastic tunneling spectrometer developed by Edgar and Zyskowski [80]. The diode is mounted in a four-terminal bridge. A swept-bias voltage V_{bias} is applied to the diode together with a small sine-wave modulation $\Delta V \sin \omega t$ with the amplitude $\Delta V = 7$ mV and the frequency $\nu = \omega / 2\pi = 10$ kHz. The bias voltage is measured with a voltmeter while the Fourier components generated by the diode with the circular frequencies ω and 2ω are detected with a lock-in amplifier. In a first step, the bias voltage is kept zero and the bridge is balanced at frequency ω with the aid of a variable resistor. This permits the determination of the zero-bias resistance R_0 of the diode defined as

$$R_0 = \left(\left. \frac{\mathrm{d}I}{\mathrm{d}V} \right|_{V_{\text{bias}} \approx 0} \right)^{-1}. \tag{3.1}$$

In the second step, the bias voltage V_{bias} is continuously varied while the second derivative of the $I(V)$ curve is determined by measuring the signal with the circular frequency 2ω.

3.4.2. Zero-bias resistance

The zero-bias resistance R_0 of a MOM diode is mainly determined by the size of the contact structure and by the thickness of the oxide layer. In our previous measurements [18], no dependence of the zero-bias resistance R_0 on the contact area has been observed. This can be explained by the fact that the diodes with different contact areas were manufactured on wafers produced under different conditions, and consequently, had dissimilar NiO-layer thicknesses. The zero-bias tunneling resistance of the diode exhibits an exponential dependence on the barrier thickness d [18,22]

$$R_0 \propto \frac{d}{\sqrt{\bar{\phi}}} \exp\left(d\sqrt{\bar{\phi}} \right), \tag{3.2}$$

where $\bar{\phi}$ represents the average barrier height. Consequently, the effect of the variation of the contact area on R_0 has been masked by small differences of the oxide-layer thickness from wafer to wafer, which are inherent to the fabrication process and cannot be measured with sufficient accuracy. In order to overcome this difficulty, we simultaneously manufactured thin-film diodes with two different contact dimensions on the same wafer. Thus, all these diodes possess an identical NiO-layer thickness. The first type of Ni–NiO–Ni diodes was produced with a contact width of 0.14 μm that yields a contact area of about 0.020 μm^2, and the second type with a width of 0.18 μm and a corresponding contact area of about 0.032 μm^2. The results of the measurement of the zero-bias resistance R_0 as a function of the contact area for all the diodes on one wafer are presented in Fig. 20. Each point represents the average of R_0 over all the diodes connected to the same type of antenna, including resonant dipoles and bow-tie antennas with three different arm lengths. The average points over all the diodes that possess the same contact area are located at the intersection of the vertical and horizontal error bars. From these data, we first conclude that no dependence of R_0 on the type of antenna can be observed. The average zero-bias resistance results in 135.94 Ω for the diodes with the contact area of about 0.020 μm^2 and 98.59 Ω for the diodes with the contact area of about 0.032 μm^2. The standard deviation of about 12% for the smaller contact is higher than the 8.5% evaluated for wider contacts. According to these measurements the zero-bias resistance is therewith increased by a factor 1.38 when the contact area is decreased by a factor 1.65. The measurement over all diodes on another wafer with two corresponding contact dimensions yielded an increase of R_0 by a factor 1.36. This demonstrates the reproducibility of our measurements. The zero-bias resistance is consequently not exactly proportional to the inverse of the contact area. This deviation is explained by the different conduction mechanisms in the contact as discussed in the following. The resistance R_0 of the front-end contact between two metal cylinders with a common base section of radius a separated by a thin film can be approximated by the sum of two different contributions [81]:

$$R_0 = R_t + R_s = \frac{\sigma}{\pi a^2} + \frac{\rho}{2a}. \qquad (3.3)$$

The first term is the tunnel resistance R_t. It takes into account electron tunneling through the potential barrier and thermionic emission. This term is inversely proportional to the contact area and proportional to the tunnel resistivity σ of the film, which is a function $\sigma(\Phi, d, \varepsilon)$ of the height Φ, thickness d and relative permittivity ε of the potential barrier. The second term of Eq. (3.3) represents the spreading resistance R_s, which is proportional to the resis-

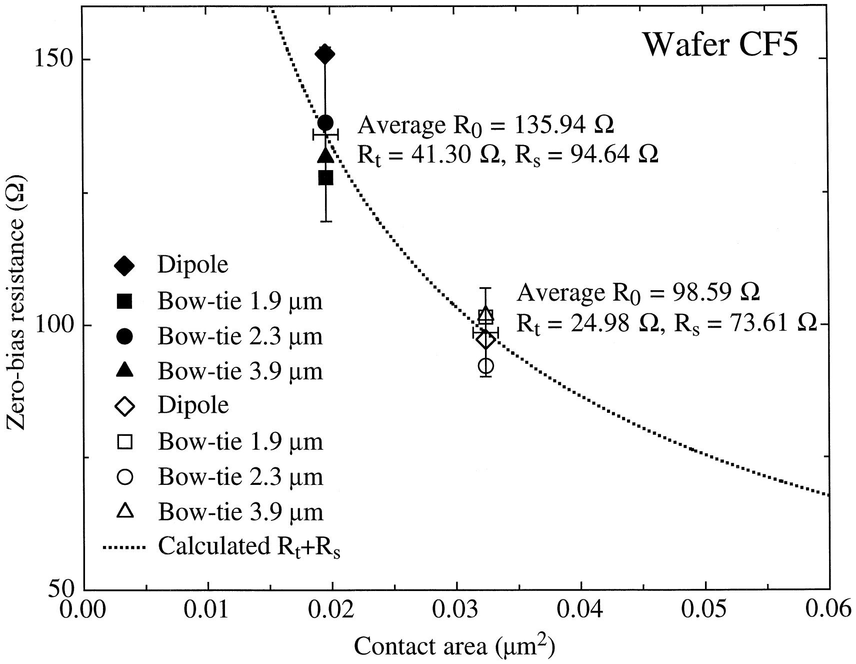

Fig. 20. Average zero-bias resistances as functions of the contact area for all diodes on one water.

Table 1
Average zero-bias resistances of thin-film Ni–NiO–Ni diodes

Wafer	Contact area (μm^{-2})	Antenna	R_0 (Ω)
CF5	0.032	Dipole	97.3 ± 10.4
CF5	0.032	Bow-tie 1.9 μm	101.5 ± 7.6
CF5	0.032	Bow-tie 2.3 μm	92.3 ± 7.2
CF5	0.032	Bow-tie 3.9 μm	101.9 ± 4.4
CF5	0.032	All types	98.6 ± 8.6
CF5	0.020	Dipole	151.0 ± 12.3
CF5	0.020	Bow-tie 1.9 μm	127.9 ± 14.3
CF5	0.020	Bow-tie 2.3 μm	138.2 ± 14.1
CF5	0.020	Bow-tie 3.9 μm	131.6 ± 11.3
CF5	0.020	All types	135.9 ± 15.8
CF6	0.020	Dipole	126.8 ± 12.8
CF6	0.032	Bow-tie 1.9 μm	87.0 ± 4.2
CF6	0.032	Bow-tie 3.9 μm	98.8 ± 12.4
CF7	0.012	Bow-tie 1.9 μm	91.4 ± 6.6
CF7	0.012	Bow-tie 2.3 μm	93.1 ± 4.0
CF7	0.012	Bow-tie 3.9 μm	85.34 ± 3.4
CF12	0.012	Spiral	97.4 ± 33.1
CF16	0.012	Bow-tie 2.3 μm	98.0 ± 42.1
CF16	0.012	Spiral	101.9 ± 40.2
All		All types	103.8 ± 26.0

tivity ρ of the metal and to the inverse of the contact diameter. In Fig. 20 the dotted curve is calculated with Eq. (3.3) adapted to a square contact. It yields the indicated resistances R_t and R_s. This measurement confirms that spreading resistance R_s also contributes to the nonlinear characteristics of our Ni–NiO–Ni diodes. This mechanism is dominant for contacts with resistances below 50 Ω. For diodes with intermediate resistances between 50 Ω and 1 kΩ the spreading resistance also exists independent of the tunneling and the thermal effects [33]. The zero-bias resistance of all the diodes used in our study range between 60 Ω and 200 Ω with an average of 103.8 ± 26.0 Ω (Table 1). The small resistances for the diodes with the minimal contact area of 0.012 μm^2 of Table 1 indicates an oxide layer slightly thinner.

3.4.3. Second derivative of the current–voltage characteristics

According to Eqs. (2.1) and (2.2), the second derivative $I''(V)$ of the current–voltage characteristics determines the efficiency of the diode for rectification of infrared radiation and second-order mixing of two coherent laser sources. The $I''(V)$ curve measured at radio frequencies adequately describes the nonlinearity of the diode up to optical frequencies [12]. This concerns the nonlinearity induced by electron tunneling and spreading resistance (Section 2.1.2). On the contrary, the $I''(V)$ curves measured at low frequencies do not include the thermionic emission signals observed in detection experiments at infrared frequencies, because the thermal effects originate in principle in the temperature rise caused by absorption of infrared radiation in the metal and/or in the substrate.

With our thin-film Ni–NiO–Ni diodes, we performed the measurements at the frequency of 10 kHz with bias voltages ranging from -250 mV to $+250$ mV. We did not make systematic measurements at higher bias voltages, because they would increase the probability of the dielectric breakdown of the NiO layer. These measurements permit also a first selection of the diodes by connecting them to a voltage above the typical working range for infrared measurement of 160 mV. All the measured $I''(V)$ curves are antisymmetric with respect to the zero bias voltage. Three types of dependence of I'' on the bias voltage have been observed. For the L-type diodes, the second derivative of the $I(V)$ characteristics varies linearly with the bias voltage (Fig. 21). This behaviour is typical for all the diodes that were manufactured with the larger contact area of 0.032 μm^2. For the S-type diodes, a saturation of the $I''(V)$ curve for bias voltages higher than 150 mV is observed (Fig. 22), while the M-type diodes exhibit a maximum of $I''(V)$ for bias voltages near 200 mV (Fig. 23). Averages over three samples of diodes of $I''(V)$ at the maximum or at $V_{\text{bias}} = 250$ mV are listed in Table 2. The average of the third row of the table can be compared with the first two rows only with caution, because it is related to diodes which were manufactured on wafers with an oxide layer that is probably thinner. However, a drastic increase of the nonlinearity at $V_{\text{bias}} = 250$ mV is definitely observed when the contact area is decreased.

An approximate classification of the diodes is also given in Table 2, which shows a shift from the linear $I''(V)$ curves to those with saturation or maximum when the nonlinearity increases. Therefore, we conclude that there is no basic difference in the nature of

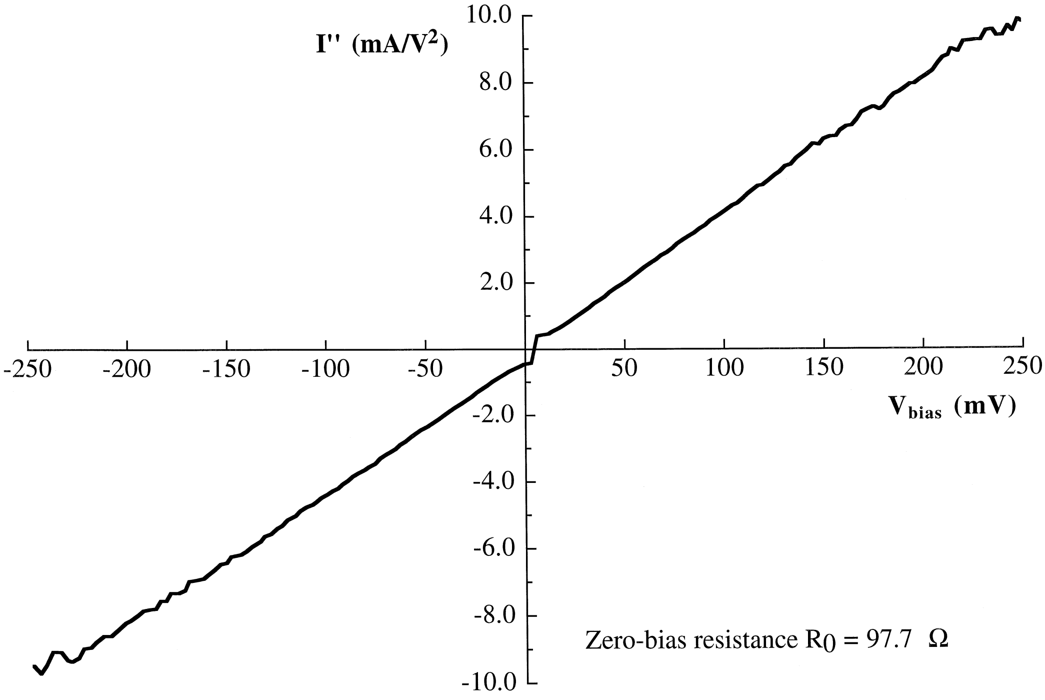

Fig. 21. Second derivative of the current-voltage characteristics $I(V)$.

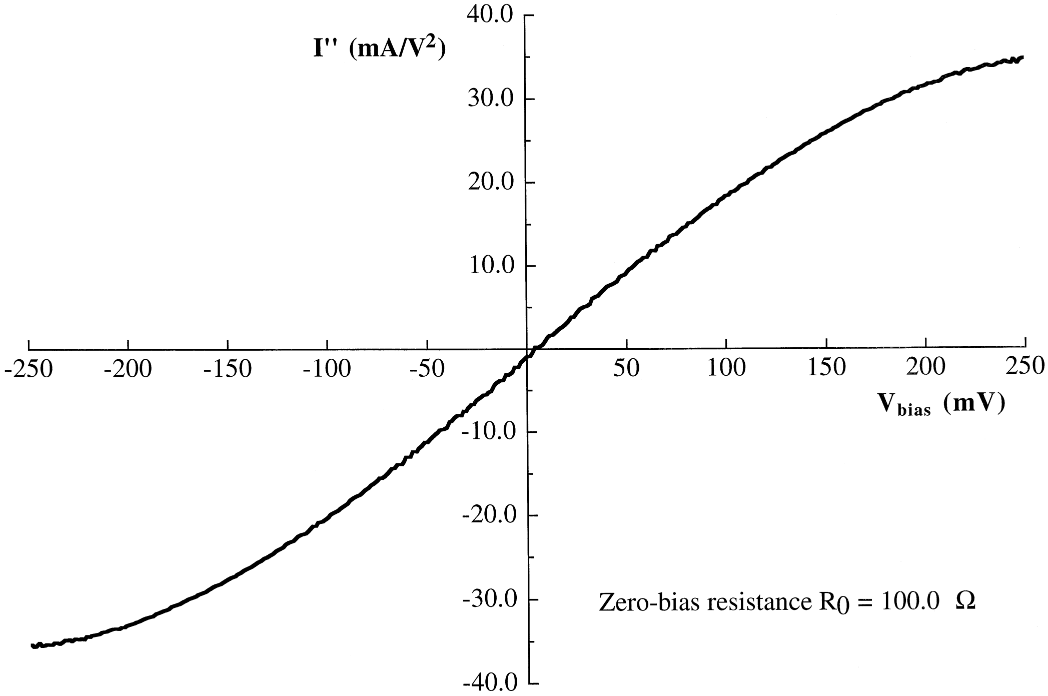

Fig. 22. Second derivative of the current-voltage characteristics $I(V)$ with saturation.

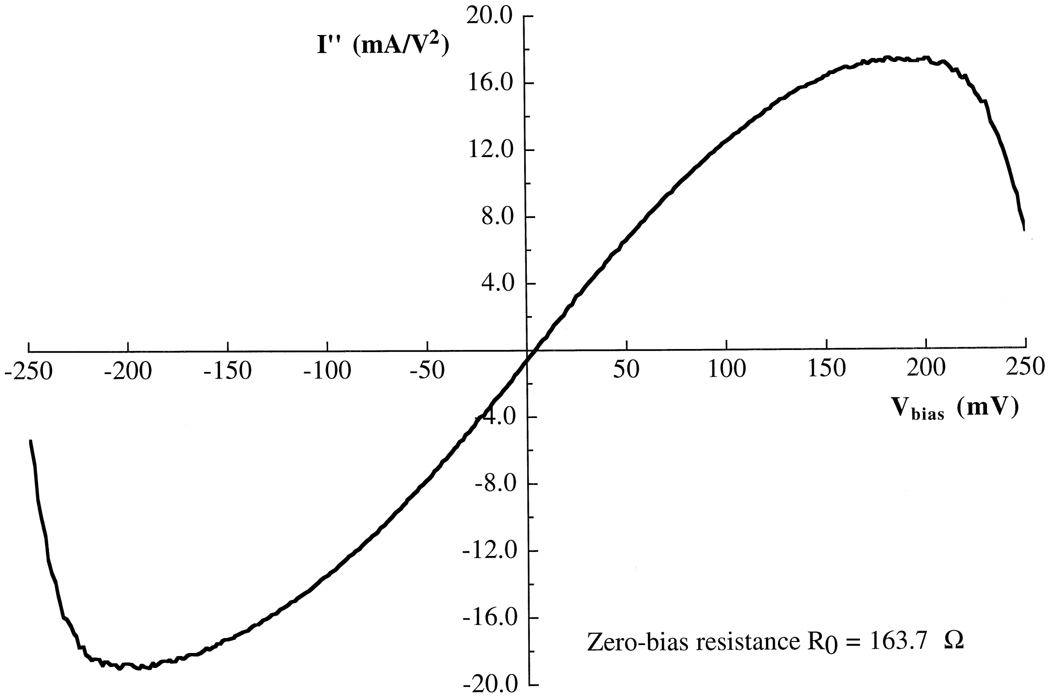

Fig. 23. Second derivative of the current-voltage characteristics $I(V)$ with a maximum.

the curves. The linear and saturated curves simply describe portions of curves with insufficient change of V_{bias} to exhibit a maximum in $I''(V)$. Fig. 24 shows an $I''(V)$ characteristic of a diode with the bias voltage extended up to 600 mV, which confirms this conclusion. This diode exhibits a linear $I''(V)$ characteristic up to 250 mV, then a domain with saturation and a maximum at a bias voltage of 545 mV. A similar behaviour has been observed by other authors for point-contact [82,33] and for thin-film MOM diodes [35,28,15]. The magnitude of $I''(V)$ of our thin-film Ni–NiO–Ni diodes at $V_{\mathrm{bias}} =$ 250 mV is comparable to those measured for point-contact diodes and larger than those reported for thin-film diodes manufactured by other authors. The maximal measured $I''(V_{\mathrm{bias}} = 250\ \mathrm{mV})$ is as high as 54.1 mA/V^2 for one of our diodes with a zero-bias resistance of 60 Ω.

The nonlinearity of a diode depends on the contact area and on the oxide-layer thickness. These also determine the diode zero-bias resistance R_0. We have observed that the second-order nonlinearity is higher for the contacts with a smaller R_0. The measurements of the second derivative of the $I(V)$ characteristics at a bias voltage $V_{\mathrm{bias}} = 250$ mV reported by [18] can be described as a function of R_0 by

$$I''(R_0) = aR_0^{-b} \tag{3.4}$$

with $a = 33\ \mathrm{A}/\mathrm{V}^2$ and $b = 1.91$. Measurements on point-contact diodes show the same behaviour with

Table 2
Average electrical characteristics of the three types of thin-film Ni–NiO–Ni diodes

Wafer	Contact area ($\mu\mathrm{m}^{-2}$)	$I''(V = 250\ \mathrm{mV})\ (\mathrm{mA}/\mathrm{V}^2)$	L type (%)	S type (%)	M type (%)
CF5	0.032	6.84 ± 1.78	100	0	0
CF5	0.020	9.63 ± 1.74	45	45	10
CF12 and 16	0.012	24.78 ± 9.53	0	75	25

The three types are defined by $I''(V)$: L = linear, S = with saturation, M = with a maximum.

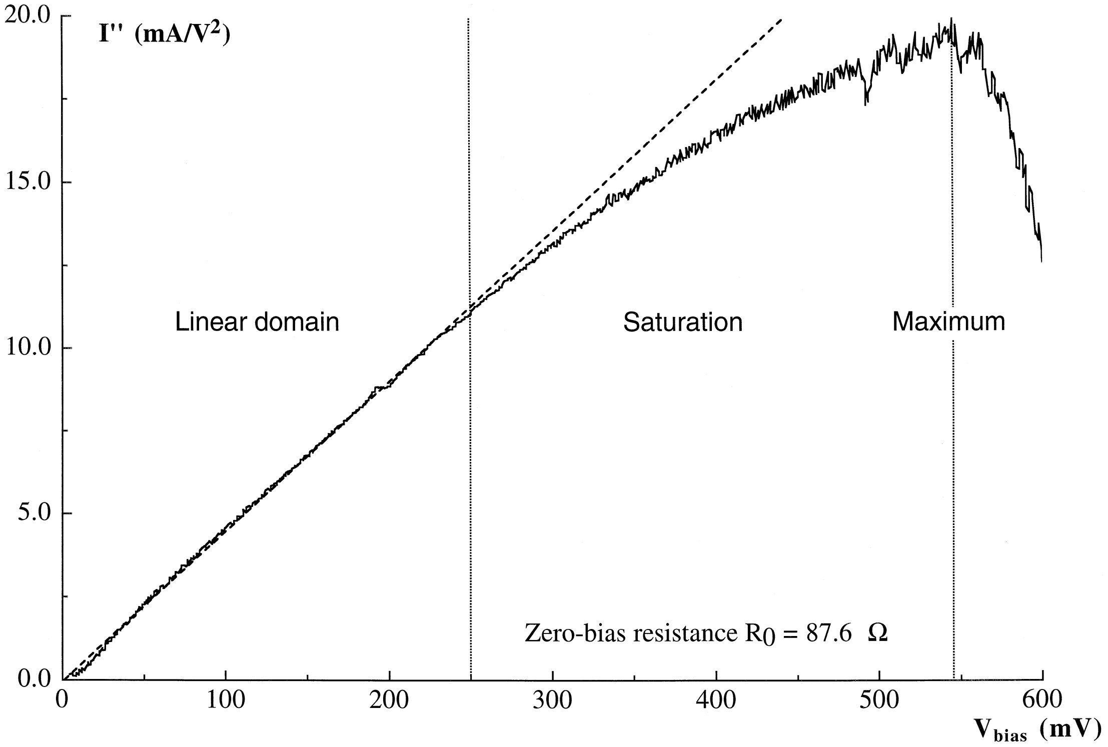

Fig. 24. Second derivative of the current-voltage characteristics $I(V)$ for a high bias voltage.

$b = 1.5$ (S. Marchetti, Instituto di Fisica Atomica e Molecolare del CNR, 56100 Pisa, Italy, Private communication, 1997). The fitting of our data for $I''(R_0)$ of all the measured diodes on different wafers results in $b = 1.52$, yet with a large standard deviation. The fact that the parameter a certainly depends on NiO-layer thickness and contact area explains the variation of our measured data. Fitting performed on samples of diodes with comparable quality yields values of b between 1 and 2.

4. Detection of infrared cw laser radiation

The nonlinearity of the MOM diodes permits the detection of infrared radiation because it generates a dc voltage that can then be measured with conventional electronics. In this section, the detection experiments of cw laser radiation are presented. After a brief description of the experimental arrangement, we discuss the substrate interferences that influence the response of all diodes. Subsequently, we describe the results of the measurement performed on linear polarized antennas. This section includes an explanation of the polarization-dependent response of the diodes, a comparison of the response of diodes with different contact areas and various types of antennas and information on the different antenna patterns. Section 4.4 is devoted to the particular polarization measurements performed on the diodes with integrated spiral antennas.

4.1. Experimental arrangement

The experimental arrangement for the detection of linearly polarized cw radiation is illustrated in Fig. 25. A grating-tuned flowing-gas cw-CO_2 laser generates linearly polarized radiation. The line emissions with a discrete wavelength distribution between 9.2 μm and 10.8 μm are generated in a TEM_{00} Gaussian mode. The stability of the output power is verified by coupling one part of the radiation with a beam splitter to a thermal power meter. The beam splitter also permits the colinear superposition of a

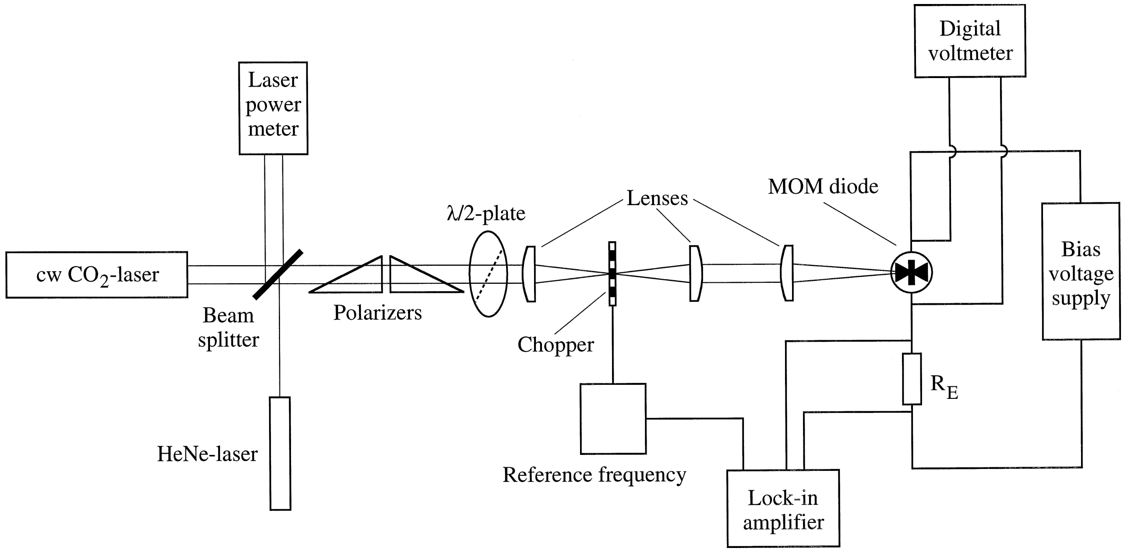

Fig. 25. Experimental arrangement for the detection of cw 10 μm CO_2-laser radiation.

HeNe-laser beam with our infrared radiation in order to facilitate the adjustment of the optics and the alignment of the diode. With the help of two polarizers composed of ZnSe windows under the Brewster angle we achieve a precise tuning of the laser power. By the rotation of the first polarizer, we can continuously attenuate the polarized beam produced by the laser. With the second fixed polarizer we can restore the original polarization. The direction of the linear polarization can be rotated by turning the fast axis of a CdS half-wave plate. The laser beam is chopped with a frequency of 3.6 kHz and focused onto the diode with a lens of 12.7 cm focal length. This yields a focal spot radius of approximately 100 μm. The signal is measured across a resistance R_E in series with a lock-in amplifier, while a bias voltage of typically 160 mV is applied to the diode. The diode is mounted on an x–y–z stage that can also be rotated to vary the angle of incidence. All the experiments are performed at room temperature.

4.2. Substrate interferences

As mentioned in Section 2.2.1, our integrated antennas are about forty times more sensitive to the radiation incident from the substrate than to radiation that comes from the air side. Because of the reflections at the interface between the several dielectric layers of our substrate, interference patterns are observed when the optical path in the substrate is varied. This variation occurs, e.g., when the angle of incidence or the wavelength of the incoming CO_2-laser radiation are varied. The marked interferences with identical characteristics for the dipole, the bow-tie and the spiral antennas mask the actual antenna patterns. The substrate three-layer system is analogous to a Fabry–Pérot interferometer. Radiation reflected at the first SiO_2 interface interferes with radiation transmitted by the substrate and reflected at the gold of the back side of the chip as indicated in Fig. 12. This effect is principally observed in the 10P-branch of the CO_2-laser spectrum between 10.4 and 11.0 μm wavelength. In this range, the transmission of our substrate reaches a maximum because of the small absorption in the SiO_2 and Si layers and due to the optimal efficiency of the SiO_2 antireflection coating [19]. The interference patterns are calculated for the variation of the angle of incidence at a fixed wavelength on one hand and for the variation of the wavelength for a fixed angle of incidence of the laser radiation on the other hand. All the expressions for the reflection and transmission coefficients as well as for the phase shifts at the different interfaces of the substrate are taken from Ref. [83] and the optical constants of the material from Ref. [84]. The absorption in the different layers and the variation of the material constants with the wavelength have been taken into account in the calculation. Two-beam interferences are expected to describe the effect with a sufficient accuracy, since beams reflected several times are strongly attenuated. The substrate thickness d is 385 ± 2 μm. The exact thickness d determines the location of the interference minima and maxima and is therefore the relevant fitting parameter. A small variation Δd of the substrate thickness d has a dramatic influence on the interference pattern. Thus, if $\Delta d = 0.77$ μm, which corresponds to one fourth of the effective wavelength of 10.6 μm radiation in our substrate, the location of the maxima and minima are reversed.

The response of a MOM diode as a function of the angle of incidence θ is displayed in Fig. 26 for two adjacent lines of the CO_2-laser with wavelengths near 10.6 μm. Also represented in these graphs are the calculated interferences. Both yield a silicon-layer thickness of 385.71 μm. From these calculations and from the measurements performed on several diodes, we conclude that the substrate thickness fluctuates along the surface of a wafer. However, these small fluctuations are only perceptible for diodes on the wafer, which are located several millimeters away from each other. The measurement performed as a function of the angle of incidence on a particular diode gives therefore an indication on the substrate thickness in its proximity and permits a reliable approximation of the interference effects for all the diodes located on the same chip and on the neighbours. As obvious from Fig. 26, the behaviour at any wavelength in the 10P-branch can also be calculated from the interference pattern measured at the particular wavelength.

By tuning our laser resonator with the help of a rotating grating, different vibrational–rotational CO_2-laser line emissions can be generated. These lines are approximately equidistant in each of the four branches of the spectrum (Ref. [85], Chapt. 12.6). Fig. 27 shows the dc response of a MOM diode as a function of the free-space wavelength in the 10P-branch for a fixed angle of incidence. The interference curve is calculated with the method already used for the variation of the angle of incidence. According to this measurement at normal

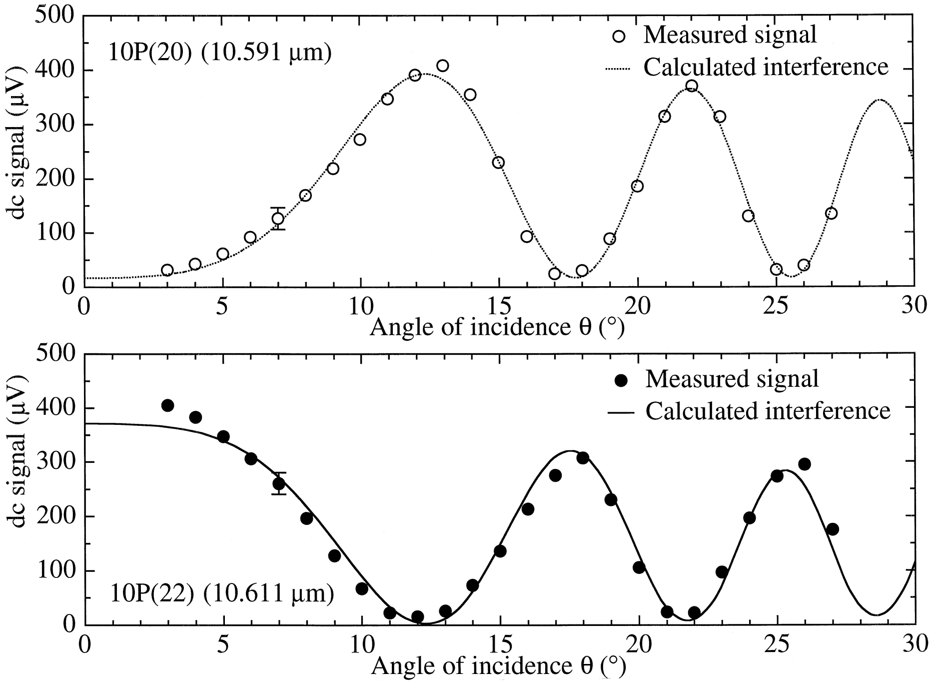

Fig. 26. Response of a MOM diode as a function of the angle of incidence for two adjacent CO_2-laser emissions, each with a power of 200 mW.

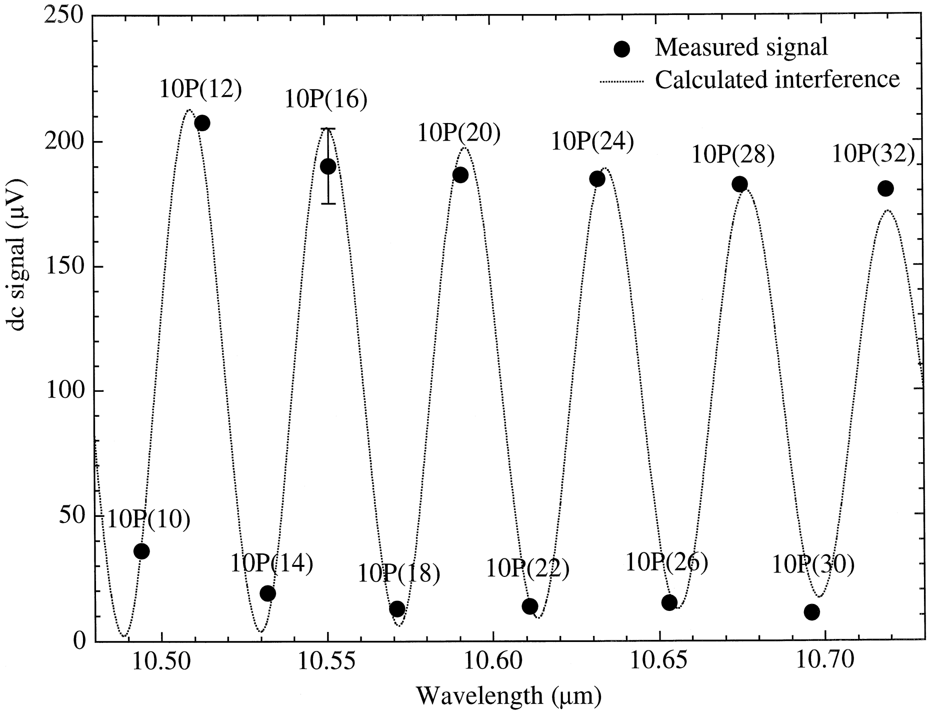

Fig. 27. Oscillation of the detected signal as a function of the free-space wavelength caused by the substrate interference as measured for a laser power of 200 mW.

incidence, the thickness of the substrate under this particular diode is estimated to be 384.96 μm. We also observe that if the response at a defined wavelength corresponds to an interference maximum, the signals measured by irradiation with adjacent lines are approximately at interference minima. This originates in the dielectric properties and the dimensions of our substrate and not in the characteristics of diode or antenna. The irradiation of the diode from the air side with reflection on the back side of the chip is consequently not well suited for mixing experiments between two adjacent CO_2-laser emissions because a measured interference maximum for the wavelength of a CO_2-laser emission implies an interference minimum for the adjacent emission.

The influence of substrate interferences and losses can be reduced in several ways. First, radiation can be coupled to the antenna through an antireflection coated hemispherical lens mounted on the back of the substrate [41]. Secondly, the lens can also be manufactured in the form of a Fresnel lens, by forming diffraction microstructures at the back side of the chip [86]. In another scheme, the silicon substrate is reduced to a thin membrane of a few micrometers by chemical etching [87].

In the chip configuration of our Ni–NiO–Ni diodes illumination from the back side of the substrate combines the better efficiency of the antenna for radiation coming from the substrate with the reduction of the amplitude of the oscillation caused by interferences. For CO_2-laser radiation in the 10P-branch with a wavelength near 10.6 μm about 80% of the incident beam is transmitted through the substrate to the diode and the antenna, while the reflection is poor. Consequently, one still observes interference patterns when the diode is illuminated from the back, yet with a much lower contrast. In this case, we have measured ratios of the signal for an interference maximum vs. the signal for an adjacent interference minimum below 2. In the case of the illumination from the air side, this ratio reaches about 5 for diodes on chips that are mounted on the gold socket. It exceeds 10, as apparent in Figs. 26 and 27, if the back side of the chip is coated with a gold layer. This layer constitutes a mirror with less roughness and, consequently, better reflectivity. Due to the technical problems caused by the connections of the diodes illuminated from the back side, this configuration has been used only for the mixing experiments in a flip-chip arrangement (Section 3.3.3).

4.3. Detection with linear polarized antennas

This section describes the polarization dependence of the response of thin-film diodes with integrated dipole and bow-tie antennas. According to theory these two types of antennas are matched to linearly polarized radiation with the electric field parallel to the antenna axis.

4.3.1. Polarization dependence of the laser-induced response

In the investigation of the polarization dependence of response of our diodes to linear polarized radiation, the angle φ between the antenna axis and the polarization direction is rotated in increments of 6° by means of the half-wave plate. The response of the diode is measured for normal incidence of the 10.6-μm laser radiation. As expected, the strongest signals are detected for the polarization parallel to the antenna axis when $\varphi \approx 0°$ (Fig. 28). The detected voltage $V(\varphi)$ can then be represented as the sum of a polarization-independent contribution V_{ip} and a polarization-dependent contribution $V_{\mathrm{p}}(\varphi)$ that is described by a cosine-squared curve

$$V(\varphi) = V_{\mathrm{ip}} + V_{\mathrm{p}}(\varphi) = V_{\mathrm{ip}} + V_{\mathrm{p}} \cos^2(\varphi - \varphi_0), \tag{4.1}$$

where φ_0 describes the location of the maximal polarization response. For all the investigated diodes with dipole and bow-tie antennas we have measured values of φ_0 close to zero. The small deviations within ±5° observed are explained by the error associated with the positioning of the diode and with the definition of the horizontal and vertical polarizations.

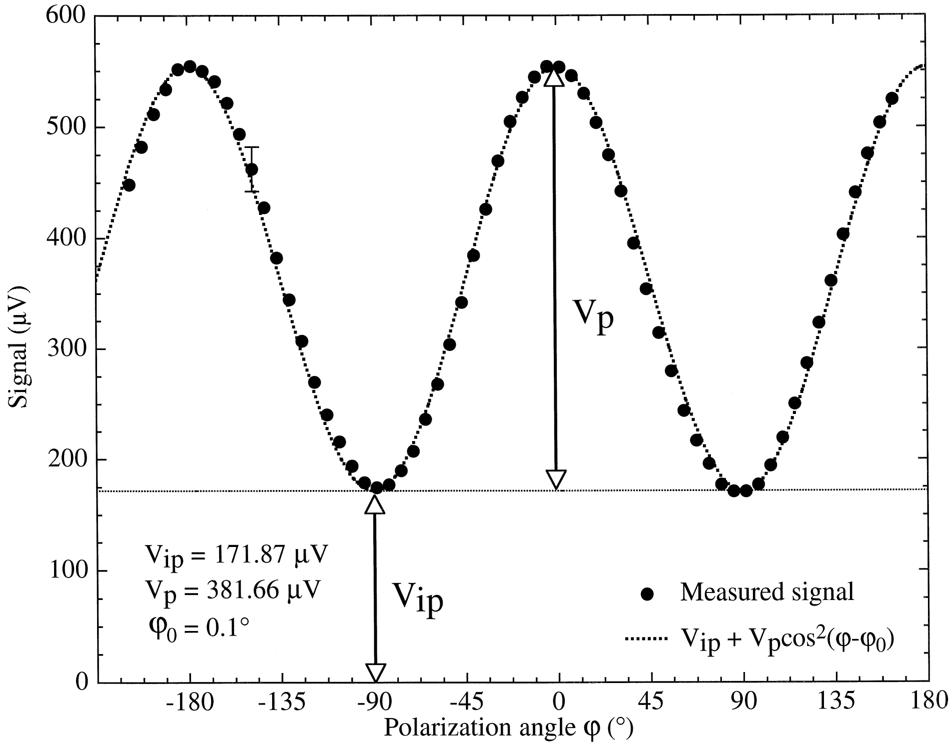

Fig. 28. Polarization dependent response of the MOM diode with integrated bow-tie antenna.

A maximum ratio $V_p/V_{ip} \approx 1.8$ was measured with MOM diodes equipped with bow-tie antennas with a half-length $L/2 = 2.3$ μm located on a silicon substrate with a low resistivity of 3–5 Ω cm. A few detection experiments performed with the diodes manufactured for the mixing experiments and based on a high-resistivity ($\rho > 3$ kΩ cm) silicon substrate showed the higher ratio $V_p/V_{ip} \approx 2.2$. This confirms that the antenna currents are less attenuated on this substrate.

The polarization-dependent part $V_p(\varphi)$ of the response is attributed to coupling of incident laser radiation in the antenna to the MOM diode. A part of this signal can be attributed to dissipation of antenna currents into Joule's heat. Yet this effect was shown not to contribute significantly to V_p [18]. The cosine-squared dependence of V_p corresponds to the prediction of antenna theory. The polarization-independent contribution V_{ip} includes the thermal response that originates predominantly in the absorption of laser radiation in the SiO_2-layer of the substrate. The above reference also presents experimental evidence that a fraction of V_{ip} can also be attributed to antenna coupling.

4.3.2. Comparison of the response of various thin-film diodes

In this section we present the method of comparison of the detection sensitivity of thin-film Ni–NiO–Ni diodes with various contact areas and antenna configurations. As for the investigation of the zero-bias resistance, the comparison between diodes manufactured on the same wafer eliminates the influence of dissimilar oxide-layer thicknesses. The responsivity of the diodes defined as the ratio of the output dc voltage vs. the incident radiation power yields a reliable figure of merit for the diode performance. However, the definition of the power incident on the diode implies the knowledge of the effective detector area. The focusing of 10-μm radiation with conventional ZnSe lenses results in beam waists much larger than the dimensions of diode and antenna, so that a definite determination of the effective area of the detector is difficult and a theoretical estimation is subject to caution. A simpler characterization of the relative figure of merit of the various configurations of our diodes is obtained by performing detection experiments under identical irradiance conditions at a wavelength near 10.6 μm in the 10P-branch of the CO_2-laser spectrum. For this purpose, we have focused infrared radiation with a power of 0.2 W onto a diode with a lens with 12.7-cm focal length. The aperture of the lens has a diameter of 1.5 cm. This results in a $1/e^2$-beam radius at the focus of approximately 100 μm and an irradiance of about 500 W/cm^2. The beam is chopped with a frequency of 3.6 kHz. A bias voltage of 160 mV is applied to the diode. For each measurement, the angle of incidence is varied from normal incidence to an interference maximum of the response. Calculation and measurement of interference patterns show that the first interference maximum occurs definitively in a range between normal incidence and an angle of incidence in air of 20°. As interference patterns originate in the substrate and do not depend on contact area or type of antenna, the response of the diode for an interference maximum near normal incidence is assumed to characterize the performance of a diode relative to the others. In the following, the influence of the contact area on the detected signal is first discussed. Then the efficiency of the various types of antennas, which couple the incident radiation to the diode, is analyzed. At the end of this section we give information on the radiation patterns of the different tested antennas and on the detector performance.

4.3.3. Response as a function of the contact area

The influence of the contact area on the response has been investigated with the diodes produced on the wafer already mentioned in Section 3.4.2. On this wafer, diodes with two different contact areas of about 0.020 μm^2 and 0.032 μm^2, yet with an equivalent oxide-layer thickness, have been manufactured. The polarization-independent and polarization-dependent signals V_{ip} and V_p averaged over all the diodes on the wafer with the same type of antenna, including resonant dipoles and bow-tie antennas with three different arm lengths, are plotted in Figs. 29a and 29b as functions of the contact area.

For both contact areas mentioned and various types of antennas, the polarization-independent contribution V_{ip} of the signal ranges within 142.9 ± 18.0 μV. It is apparently independent of the contact area (Fig. 29a). This contribution is mainly thermal in origin. Thermal effects are not related to the contact area [28]. Our diodes are square-law detectors. As a

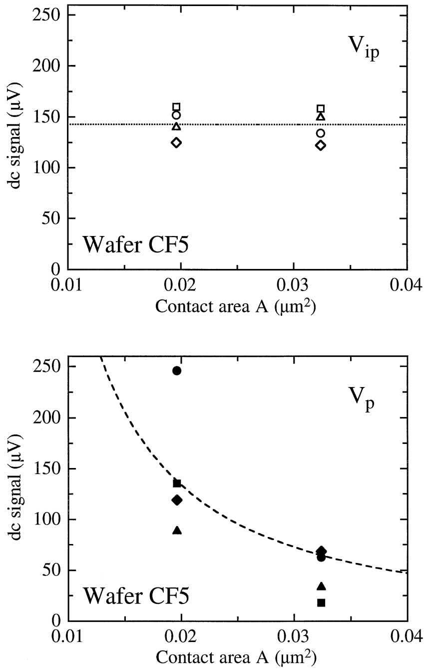

Fig. 29. (a): Average measured polarization-independent contribution V_{ip} as a function of contact area: ◇ Dipole $L = 3.1$ μm, □ bow-tie $L/2 = 1.9$ μm, ○ bow-tie $L/2 = 2.3$ μm, △ bow-tie $L/2 = 3.9$ μm, ······ $V_{\text{ip}} = 142.9$ μV. (b): Average measured polarization-dependent contribution V_{p} as a function of the contract area: ◆ Dipole $L = 3.1$ μm, ■ bow-tie $L = 1.9$ μm, ● bow-tie $L/2 = 2.3$ μm, ▲ bow-tie $L/2 = 3.9$ μm, --- $A^{-3/2}$-dependence.

consequence the signal is proportional to the incident radiation power. Thus, the rectified current density is also proportional to the temperature rise in the diode. This temperature rise is practically inversely proportional to the contact area that determines the volume of diode material and as a consequence the thermal mass. Larger temperature increases occur in the diodes with smaller contact areas. On this condition the resulting higher current densities compensate the current reduction caused by the smaller detector area.

On the contrary, the average polarization-dependent contribution V_{p} of the rectified signals shows a large increase when the contact area of the diode is decreased from 0.032 μm^2 to 0.020 μm^2 (Fig. 29b). The polarization-dependent contribution V_{p} originates principally in rectification of antenna currents in the diode by the tunneling mechanism. The different sensitivities of the various antenna types will be described in detail in Section 4.3.4. The overall increase of the signal for the small contact area is a consequence of the limitation of the efficiency of the tunneling mechanism by the RC-limited circuit speed described in Section 2.1.3. For both sizes of the contact represented in Fig. 29, the incident laser radiation with a frequency of approximately 28 THz exceeds the cut-off frequency ν_{c} of the circuitry defined by Eq. (2.3). According to Sanchez et al. [35], the response amplitude decreases for a fixed frequency above ν_{c} with an $A^{-3/2}$-dependence on the contact area A. This dependence is also represented in Fig. 29b.

These measurements show that the reduction of the contact area constitutes a crucial issue of extreme-frequency detection and mixing with thin-film MOM diodes. We succeeded in the manufacture of diodes with a minimal contact area of approximately 0.012 μm^2. These diodes exhibited the largest polarization-dependent responses, because of their comparatively large cut-off frequencies ν_{c}, close to that of the 28-THz incident radiation.

4.3.4. Response dependence on the type of antenna

In order to analyze the influence of the antenna type on the response of thin-film Ni–NiO–Ni diodes, we consider samples of diodes with identical contact areas and oxide-layer thicknesses. In Table 3 we

Table 3
Average detected polarization-independent V_{ip} and polarization-dependent V_{p} responses of thin-film Ni–NiO–Ni diodes with integrated antennas

Wafer	Contact area (μm^{-2})	Antenna type	Average V_{ip} (μV)	Average V_{p} (μV)
CF5	0.020	Dipole	125.0	119.0
CF5	0.020	Bow-tie $L/2 = 1.9$ μm	160.2	135.6
CF5	0.020	Bow-tie $L/2 = 2.3$ μm	152.2	245.8
CF5	0.020	Bow-tie $L/2 = 3.9$ μm	140.0	88.4

present the measured signal averaged over four samples of diodes equipped with resonant full-wave dipole antennas and bow-tie antennas of three different half-lengths $L/2$. The polarization-independent contribution V_{ip} of the response, which is mainly thermal in origin, shows only a weak dependence on the antenna type. A 20% smaller V_{ip} is measured with dipole antennas with respect to the V_{ip} obtained for bow-tie antennas. This is probably explained by the fact that in the last configuration, a small amount of radiation is also coupled by the antenna for the polarization perpendicular to the antenna axis.

As expected, the polarization-dependent part of the signal, that in principle originates in the rectification of antenna currents in the diode, exhibits a distinct dependence on the antenna type. The dipole antennas that were investigated in this case are identical to the most sensitive resonant dipoles presented by Wilke et al. [19]. They have a total length $L = 3.1$ μm which corresponds to a full dielectric wavelength of the incident radiation. Bow-tie antennas with half-lengths $L/2 = 1.9$ μm and $L/2 = 2.3$ μm show, under identical irradiance conditions, a larger response than these dipole antennas. The poor sensitivity attained with the longest bow-tie antenna with the half-length $L/2 = 3.9$ μm confirms that the antenna currents are strongly attenuated.

Deviations of the relative efficiencies for the different antenna types are observed from wafer to wafer. These deviations are caused by changes of the impedance-matching conditions because of the differences in contact area and oxide-layer thickness. They explain, e.g., the nontypical deficient sensitivity achieved by diodes with a contact area of 0.032 μm^2 connected to 1.9-μm bow-tie antennas (Fig. 29b). However, the following conclusions with respect to these linearly polarized antennas are still valid for the diodes with small contact areas $A \leq 0.02$ μm^2. First, the polarization-independent contribution V_{ip} of the signal is almost independent on the shape of the antenna. Secondly, polarization-dependent signals V_p approximately a factor 2 stronger than all the others are obtained for a bow-tie resonant half-length $L/2 = 2.3$ μm. This corresponds to a full length L of $3/2$ of the dielectric wavelength of 10.6-μm laser radiation. Furthermore, it should be noticed that bow-tie antennas with $L/2 = 1.9$ μm exhibit sensitivities slightly higher than resonant full-wave dipoles. As in the case of dipole antennas, the gain of a bow-tie antenna is not improved by increasing its length.

4.3.5. Radiation patterns

The radiation patterns of the bow-tie antennas integrated in our diodes have been measured in the E plane, defined by the inset of Fig. 5, for angles between $\theta = 0°$ for normal incidence and about $\theta = 50°$. This limit is set by the presence of diffraction effects on the bonding wires for larger angles. The interpretation of the results in this incomplete range is furthermore complicated by the substrate interferences that mask the antenna patterns. However, differences in the power patterns of the various antennas are perceptible with a good reproducibility and permit a first characterization. The angle θ is measured with an accuracy of $\pm 0.5°$ relative to the normal incidence $\theta = 0°$ that is determined with an accuracy of $\pm 5°$. The wavelength relevant in the following discussion is the dielectric wavelength of 10.6-μm laser radiation, i.e., approximately $\lambda_\varepsilon \approx \lambda_{eff} \approx 3.1$ μm.

For the bow-tie antennas with three different arm-lengths, no difference in the power pattern was observed for the polarization-independent response V_{ip}. For a variation of the angle of incidence θ, the overall behaviour of this contribution to the signal is well approximated by a $\cos \theta$ function. This part of the signal, mainly of thermal origin, varies then according to the decrease of laser irradiance if the angle of incidence is increased.

More interesting is the power pattern of the polarization-dependent response V_p, originating in the rectification of antenna currents in the diode. The observation of this pattern permits a better understanding of the operation of our bow-tie antennas with a flare angle $\phi = 60°$ and various arm lengths $L/2$. Extensive radiation-pattern measurements at frequencies of about 500 MHz on various triangular dipoles and conical antennas in free space have been performed by Brown and Woodward [54]. They permit a scaled comparison of their patterns with our patterns measured at infrared frequencies. A rigorous theoretical calculation of bow-tie antenna power patterns is missing in the literature. However, some similarities are observed in the distribution of the lobes measured for bow-tie antennas and calculated for thin dipole antennas with a sine-wave current distribution. The far-field pattern in the E plane of a dipole antenna with a full-length L yields [48]

$$E_\theta \propto \frac{\cos[\beta L\cos(\theta+\pi/2)/2]-\cos(\beta L/2)}{\sin(\theta+\pi/2)}, \tag{4.2}$$

where $b=2\pi/\lambda_{\mathrm{eff}}$. As the flare angle ϕ of a bow-tie antenna is increased, the narrow zeros calculated for the pattern of the thin dipole are filled. In our experiments, the incident laser radiation is not collimated, but rather focused by a lens of 12.7-cm focal length. This implies the additional convolution with an angular window, which broadens the lobes and fills the zeros. All curves measured are symmetrical in the E plane with respect to the normal axis.

The radiation pattern for a bow-tie antenna with a half-length $L/2=1.9$ μm is represented in Fig. 30. Here we observe a main lobe around normal incidence, broadened by the presence of a smaller side lobe. The experimental data of [54], which are represented in this inset of Fig. 30, are in good agreement with our data. The theory based on the ideal sine-wave dipole also predicts for this antenna length a broad main lobe, and extremely small side lobes centered around about $\pm 55°$. They are also represented in the inset. The complete absence of side lobes is only characteristic of dipole and bow-tie antennas smaller than a wavelength.

The radiation pattern measured for an integrated bow-tie antenna with $L/2=2.3$ μm is plotted in Fig. 31. From this measurement, we conclude that the pattern exhibits a main lobe for normal incidence and higher side lobes close to $\theta=\pm 50°$. Brown and Woodward [54] observed the same behaviour, however with a relatively weaker main lobe, and a second peak at approximately 45°. An ideal dipole with the same length shows side lobes near $\pm 42.4°$ with a slightly weaker amplitude than the main lobe.

The third investigated bow-tie antenna with a half-length $L/2=3.9$ μm exhibits the radiation pattern displayed in Fig. 32. For this longer structure, the antenna response V_{p} increases if the angle of incidence is increased. A lobe is observed for an angle of incidence $\geq 46°$. In the dipole model this lobe corresponds to the second side lobes located at $\pm 52.6°$ as shown in the inset of Fig. 32. For an increasing angle of incidence these follow the principal lobe for normal incidence and the first side lobes centered at $\theta=\pm 23.4°$. In the case of our bow-tie antennas the principal and the first lobes cannot be

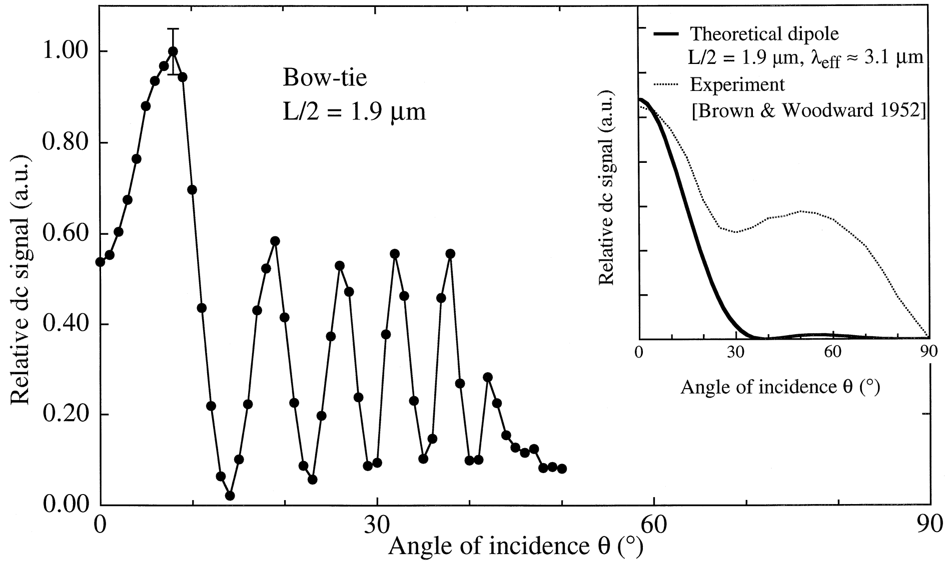

Fig. 30. Radiation pattern of the polarization-dependent contribution V_{p} in the E plane for a bow-tie antenna with half-length 1.9 μm at 10.6 μm wavelength.

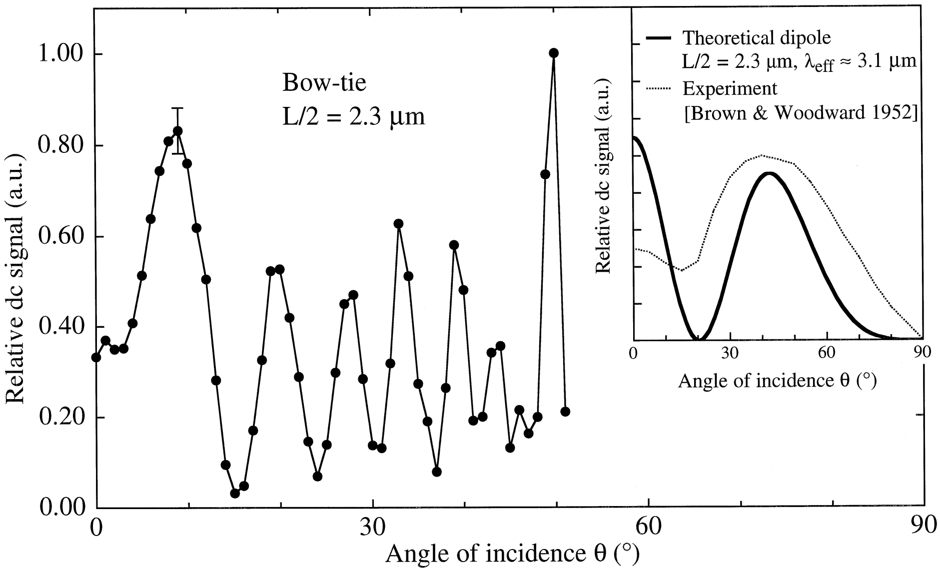

Fig. 31. Radiation pattern of the polarization-dependent contribution V_p in the E plane for a bow-tie antenna with half-length 2.3 μm at 10.6 μm wavelength.

distinguished experimentally, probably because they are broadened. To illustrate the effect of broadening the dashed curve of the inset shows the influence of a convolution over an angular window of ±8° for a thin dipole. This angular window does not correspond to our focusing optics. It is exaggerated to show the disappearance of the zeros and the broadening of the lobes. These effects originate in the convolution with an angular window. In addition, they are amplified by the deviation from the ideal sine-wave

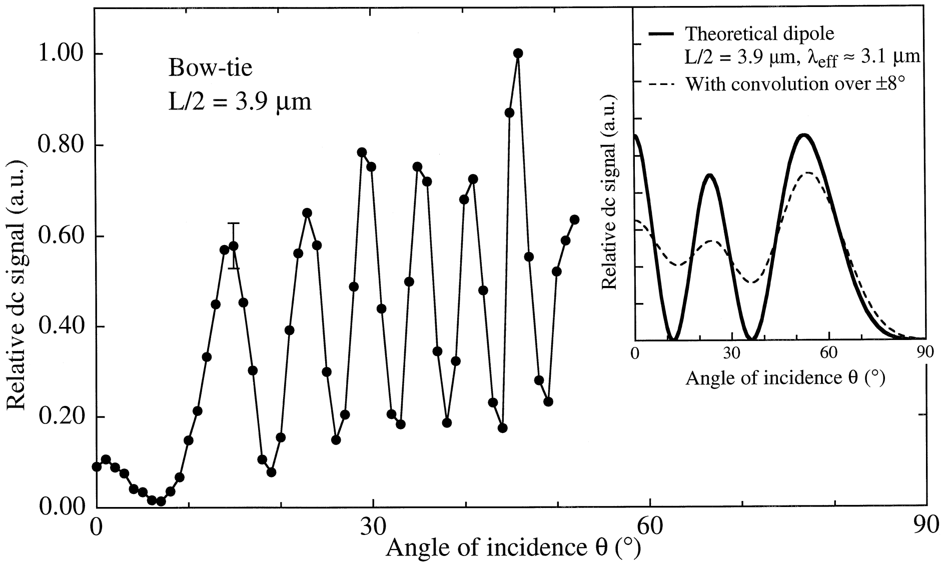

Fig. 32. Radiation pattern of the polarization-dependent contribution V_p in the E plane for a bow-tie antenna with half-length 3.9 μm at 10.6 μm wavelength.

current distribution on the bow-tie antenna. The data of Brown and Woodward include only antennas with lengths up to two wavelengths. Yet, the extrapolation suggests a decline of the lobes for small incidence angles when the length of the antenna is increased. This is in agreement with our measurement.

4.3.6. Detector performance

The effective receiving area of our integrated antennas is expected to cover only a fraction of a λ^2-area according to antenna theory [48,88]. As a consequence, we expect responsivities of the diodes in the order of a few V/W. A better estimation requires measurements of the effective receiving area of our integrated antennas.

The detection signals measured with our thin-film diodes are still about one order of magnitude below those obtained with point-contact MOM diodes for comparable CO_2-laser irradiance. We are convinced that their relatively low performance in this respect is simply caused by the smaller dimensions of their effective receiving area.

Wilke et al. [19] compared the performances of their diodes to those of other authors with the help of the enhancement factor G introduced by Heiblum et al. [28]. This factor permits only a comparison based on irradiance. Estimations for our thin-film Ni–NiO–Ni diodes connected to bow-tie antennas with a half-length $L/2 = 2.3$ μm yield a factor $G \approx 300$ at room temperature. The comparison with the G-factors listed by Wilke et al. reveals that the detection performances of our diodes are superior to those of previously reported thin-film diodes.

4.4. Detection with spiral antennas

Contrary to the antenna types already discussed the spiral antennas do not involve linear polarization. An ideal infinite spiral antenna is matched to circular polarization. However, the oversized asymmetric central feed region of our particular spiral antennas coupled to Ni–NiO–Ni diodes introduces a polarization-dependent antenna responsivity that differs from circular polarization. In order to investigate this effect, we have performed experiments with different polarizations. The Poincaré representation maps all possible polarization states one-to-one on the unit sphere [89,90,66,91]. The points located on the equator of the sphere correspond to linearly polarized radiation while the points on a meridional represent all the elliptically polarized radiations with a fixed direction of the principal axis. The axial ratio b/a of a polarization state, defined as the ratio of the minor axis b to the major axis a of the polarization ellipse, is characterized by the longitude 2ε on the sphere according to

$$\tan\varepsilon = \pm b/a. \qquad (4.3)$$

The angle ε is called the ellipticity of the ellipse and its sign is positive for left-elliptical polarization and negative for right-elliptical polarization according to the IEEE definition. Two diametrically opposite points on the sphere characterize two orthogonal polarizations, e.g., the north and south poles coincide with left and right circular polarizations. In the following sections, we describe detection experiments performed with our spiral antennas with elliptically and linearly polarized radiation.

4.4.1. Response to elliptical polarization

The experimental arrangement of Fig. 25 is modified in order to generate 10.6 μm radiation with elliptical polarization. A quarter-wave mirror for 45° incidence is mounted after the half-wave plate. The rotation of the fast axis of the half-wave plate causes a change of the polarization on a meridional line of the Poincaré sphere. Circular polarization is obtained after the reflection on the phase shift mirror when the plane of polarization of the incident beam is oriented at $\pm 45°$ from the plane of incidence. A rotation by an angle of $\varepsilon/2$ of the fast axis of the half-wave plate corresponds then to a rotation of 2ε on a meridional line of the Poincaré sphere. The angle φ of the principal axis of the polarization ellipse is defined in Fig. 15. It is arbitrarily chosen $\varphi = 0°$. We have registered the angle ε that determines the ellipticity of the polarization for maximal response of the diode as a function of the angle of incidence θ. The results expressed in axial ratios $\pm b/a$ (Eq. (4.3)) are represented in Fig. 33 for the two wiring senses of the spiral antennas manufactured. The two curves are averaged over the measurements performed on five spiral antennas with the same wiring sense, in order to reduce the error $\Delta\varepsilon = \pm 3°$ associated with a single measurement. The results for each type of spiral are located in the

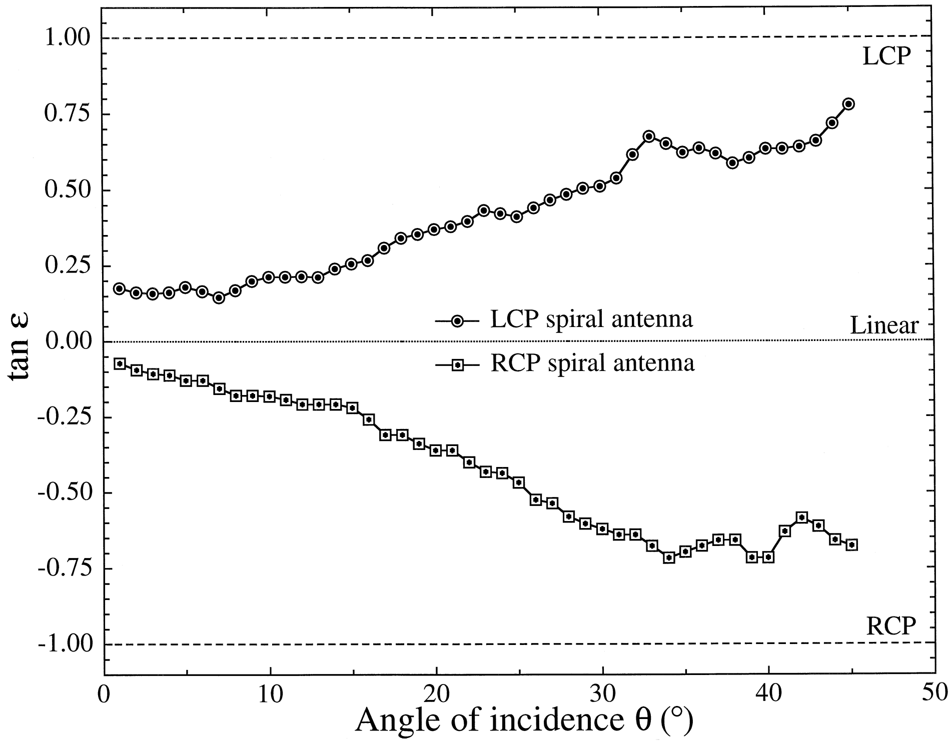

Fig. 33. Axial ratio tan $\epsilon = \pm b/a$ of the polarization at maximal response vs. angle of incidence. The positive sign indicates left-elliptical polarization and the negative sign right-elliptical polarization. The angle φ of the principal axis of the polarization ellipse is chosen arbitrarily.

hemisphere corresponding to the wiring sense of the spiral. However, the maximal response at normal incidence occurs for a flat elliptical polarization with an estimated axial ratio $b/a \approx 0.12$. It shows a strong deviation from the expected circular polarization. As the angle of incidence is increased, the maximal signal is detected for a polarization with a larger ellipticity, i.e., closer to circular polarization. These measurements demonstrate that our antennas are not matched to circular polarization. However, the two wiring senses can be clearly distinguished, particularly when the angle of incidence is increased.

4.4.2. Response to linear polarization

By measuring the maximal response of our diodes with integrated spiral antennas to linearly polarized radiation, we have determined the orientation of the major axis of the polarization ellipse. A detailed description of these experiments and their results has been published previously by Fumeaux et al. [92]. In this paper we report on the measured linear-polarization response of our diode and antenna as a function of the wavelength of the incident radiation in the range corresponding to the optimum transmission of our Si/SiO_2 substrate, between 10.2 μm and 10.7 μm in the 10R- and 10P-branches of the CO_2-laser spectrum. For this purpose the half-wave plate in the experimental arrangement shown in Fig. 25 is replaced by the combination of a CdS 10.6-μm half-wave plate, a 10.6-μm quarter-wave mirror and a BaF_2 wire-grid polarizer as illustrated in Fig. 34. This permits a precise rotation of the linear polarization of the incident radiation over the wavelength range investigated. This rotation is represented by the points on the equator of the Poincaré sphere.

The experiment was performed as follows for each CO_2-laser line investigated. The combination of the half-wave plate and the quarter-wave mirror for 10.6 μm permits a production of almost circular polarization over the entire wavelength range consid-

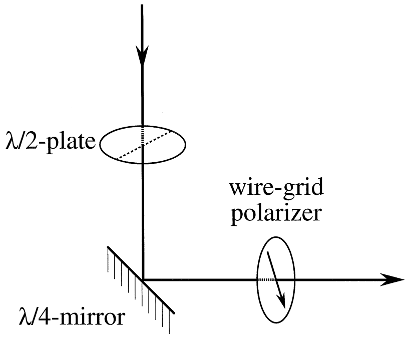

Fig. 34. Optical arrangement for the rotation of linearly polarized radiation with wavelengths between 10.2 μm and 10.7 μm.

ered by slightly rotating the fast axis of the half-wave plate with respect to the corresponding position at 10.6-μm wavelength. The selection of a linear component of the polarization in any direction is performed without change of the beam axis by rotating the wire-grid polarizer. This polarizer is mounted on a rotation stage that works with an accuracy of approximately 1 arc min. The power as a function of the polarization angle φ defined in Fig. 15 was measured with the reference thermal detector. This yields a typical power of 100 mW for all orientations of the linear polarizer. The laser beam is then focused on the diode under normal incidence. Thus, the diode response is measured as a function of the polarization angle over a range of $\geq 200°$ in 5° steps. The measured signal is proportional to the laser power. Therefore the signal for 100-mW power as a function of φ can be determined with the previously mentioned calibration curve. The resulting response can be well approximated by the sum of a constant and a squared cosine as shown in Fig. 35. The maximum response of the diode corresponds to the orientation φ_0 of the principal axis of the elliptical polarization of our spiral antenna.

The measurement has been performed for 19 lines of the CO_2-laser emission at wavelengths between 10.2 and 10.7 μm. The measured wavelength dependence of the orientation φ_0 of the principal axis of the elliptical polarization of the spiral antenna is represented in Fig. 36. The measurement shows an overall strong wavelength dependence in this small range from 10.2 to 10.7 μm with fast oscillations superimposed. The reproducibility of the data is within $\pm 1°$.

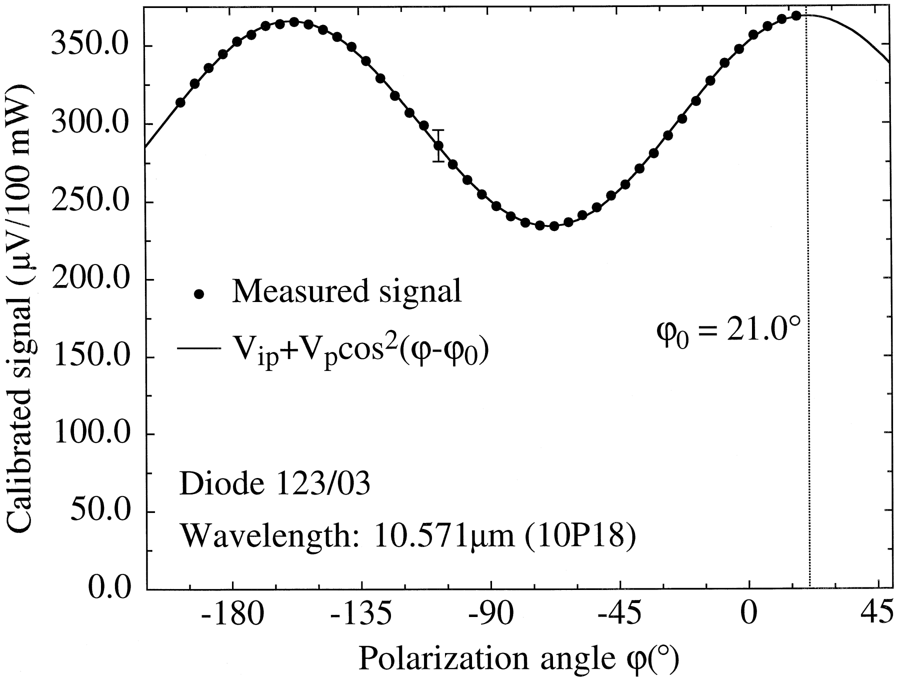

Fig. 35. The polarization dependence of the spiral antenna that determines φ_0.

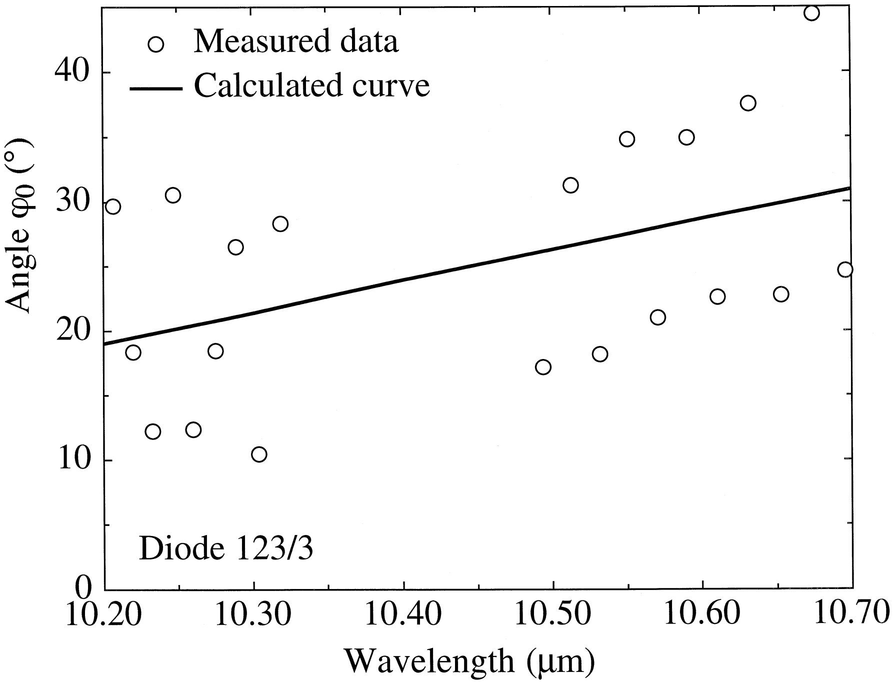

Fig. 36. Wavelength dependence of the orientation φ_0 of the principal axis of the polarization ellipse of the spiral antenna. The solid line is computed from the model.

The marked wavelength dependence can be explained by a model based on the vector addition of phasor-current elements tangential to the inner curves of the spiral. In this model introduced by Fumeaux et al. [92], the thin-film spiral antenna is approximated by a thin wire on the inner edge of the metallized section (Fig. 37) by taking into account that the current is concentrated near the innermost surface of the spiral antenna [64]. Regarding our spiral antenna as a transmitting antenna [39], a travelling wave with the circular frequency ω and an effective wavelength corresponding to the substrate wavelength of the incident radiation is sent from the feed point at the diode position. This wave propagates along the antenna as on a lossy transmission line with an attenuation coefficient $\Gamma = 0.15\ \mu\text{m}^{-1}$ (Section 2.2.2). The vector sum of all closely spaced current elements tangential to the spiral wires gives an instantaneous image of the direction and amplitude of a corresponding Hertzian dipole. During one period of the 30-THz cycle, this instantaneous dipole rotates by

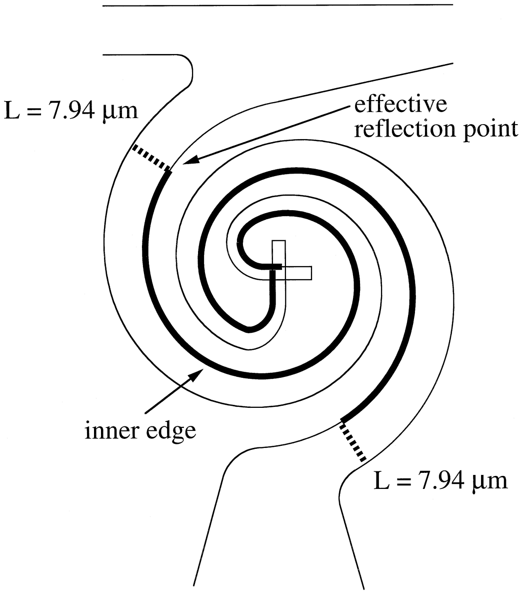

Fig. 37. Wire approximation for the current-wave paths considered in our model.

2π and covers an ellipse that represents the elliptical polarization state of the antenna. The orientation of the principal axis of this ellipse corresponds to the polarization angle φ_0 of the maximum diode response to linearly polarized radiation.

Because of the capacitive impedance of the diode and the asymmetries of the feed structure and the readout configuration, the antenna structure cannot be considered as balanced. This requires that two modes are taken into account in the calculation, a balanced mode with amplitude B and phase difference $\Delta\alpha = \pi$ at the feed point between the outgoing waves on the two spiral antenna arms on one hand, and an unbalanced mode with amplitude U and $\Delta\alpha = 0$ on the other hand. The effective propagating mode is a combination of these two fundamental modes [93].

The spiral antenna forms a transmission line for waves with frequencies of the order of 30 THz. The curvature of the antenna structure itself as well as the terminations of the arms introduce a distributed reflection of the original outgoing wave. In our model, this distributed reflection is represented by a lumped reflection after a path L on the wire spiral at a discrete location where total reflection of the outgoing wave occurs. The wave then propagates back toward the feed with a phase shift of π required by the boundary condition at the reflection point. The measured attenuation coefficient $\Gamma = 0.15\ \mu\mathrm{m}^{-1}$ is such that we neglect a second reflection of the reflected wave at the feed point.

A linear fit to the measured data yields $\varphi_0 = 30.84°$ for $\lambda_0 = 10.7\ \mu\mathrm{m}$ and a difference of $\Delta\varphi_0 = 11.75°$ for wavelengths between 10.7 and 10.2 μm. These estimations are compared with calculations performed with the aid of our model with the path L before reflection and the mode mixing ratio U/B as free parameters. This comparison yields $U/B = -0.75$ and $L = 7.94\ \mu\mathrm{m}$. This demonstrates that a significant unbalanced mode exists on the antenna structure and that reflections of the current waves near the ends of the arms affect the observed polarization behaviour. With these solutions for U/B and L we can evaluate φ_0 and $\Delta\varphi_0$ as functions of λ_0 on the basis our two-mode model. The results of this evaluation are shown as the solid line in Fig. 36.

The fast oscillation of the polarization angle φ_0 within the small wavelength range investigated, which is apparent in Fig. 36, cannot be explained by this model. A plausible cause may be rather in the surroundings of the antenna than in its structure. The period of the oscillations of φ_0 corresponds to that of the interferences presented in Section 4.2 and illustrated in Fig. 27 as functions of the wavelength in the 10P-branch. In the case of constructive substrate interference, the effect of the radiation detected from the air side of the antenna can be neglected. In the case of destructive interference, however the small signals can be influenced by modes exited by radiation incident from the air side. The oscillation of the signals resulting from these interferences induces an oscillation of the maximum polarization angle φ_0. Consequently, one should also observe oscillations of the angle φ_0 for a fixed wavelength when the angle of incidence θ is varied. Fig. 38 shows a measurement of the signal as a function of the angle of incidence θ for the CO_2-laser line 10P(20) at 10.591-μm wavelength. The same graph shows also the oscillation in opposition of the simultaneously registered angle φ_0 of the maximum polarization that is related to the right-hand y axis. The amplitude of these oscillations between $\varphi_0 = 15°$ and $\varphi_0 = 35°$ corresponds to the measurement of Fig. 36 between the line 10P(20) and the adjacent lines. This confirms that the fast oscillations are caused by a substrate effect.

4.4.3. Performance and antenna patterns

The separation of polarization-dependent and polarization-independent contribution to the response of the diode introduced for linear polarized antennas is not possible for spiral antennas. However, the sensitivity of an ideal circularly polarized antenna to linearly polarized radiation is 3 dB lower than the maximal sensitivity attainable with matched circular polarization. The maximal detected signals obtained with diodes with integrated spiral antennas illuminated with linearly polarized radiation sets then a lower limit to the possible efficiency. Therefore, we have compared only the maximal response to linear polarization attained by the best bow-tie antennas with a half-length $L/2 = 2.3\ \mu\mathrm{m}$ on one hand and the spiral antennas on the other hand. The diodes with the two types of antennas have been produced on the same wafer. For both configurations the contact area was approximately $0.012\ \mu\mathrm{m}^2$. An absolute

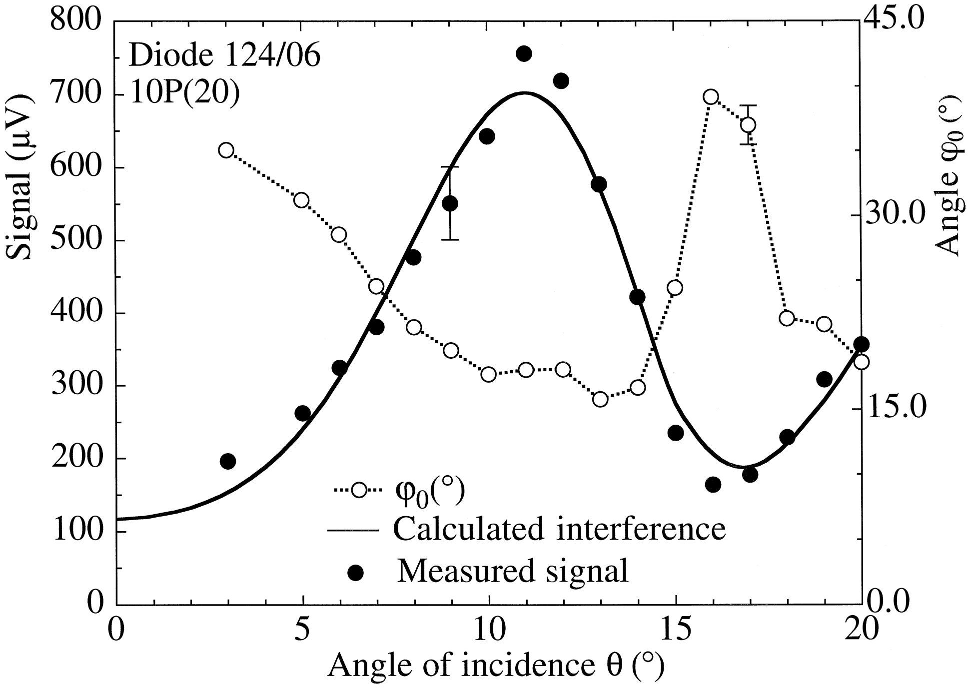

Fig. 38. Measured signal V_{tot} and maximal polarization angle φ_0 as functions of the angle of incidence θ.

comparison of these diodes relies on the assumption that the thermal effects are independent of the type of antenna. The average maximum response measured under the irradiance conditions mentioned in Section 4.3.2 is 530.15 ± 66.96 μV for thin-film Ni–NiO–Ni diodes with integrated bow-tie antennas

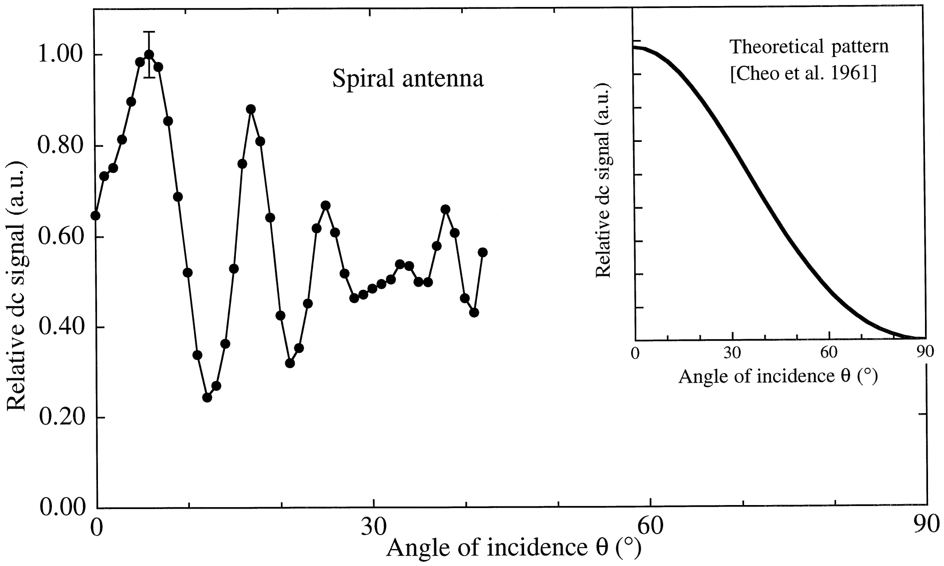

Fig. 39. Radiation pattern V_{tot} for 10.6 μm wavelength for an integrated spiral antenna with a diameter of 5.5 μm.

and 713.93 ± 33.35 μV for diodes connected to spiral antennas. Consequently, the application of spiral antennas yields a gain of at least a factor 1.35 over the best bow-tie antennas tested.

A typical measured antenna pattern of a MOM diode with an integrated spiral antenna is represented in Fig. 39. It shows a main lobe perpendicular to the antenna plane. For logarithmic spiral antennas a calculation was performed by Cheo et al. [60]. It resulted in the following dependence of the far-field amplitude $|E_\theta|$ on the angle of incidence θ:

$$|E_\theta| \propto \frac{\cos\theta\left(\tan\frac{\theta}{2}\right)^n \exp((n/a_c)\arctan(a_c\cos\theta))}{\sin\theta\sqrt{1+a_c^2\cos^2\theta}} \tag{4.4}$$

In this expression, a_c equals $(-\ln a)$ according to our definition of the spiral by Eq. (2.13), while n is an integer that equals unity for a two-arm antenna. According to this calculation, the main-beam width depends on the tightness of the spiral antenna and becomes large for a loosely tightened spiral. The calculated power pattern corresponding to our spiral antenna with $a = 1.184$ is represented in the inset of Fig. 39 for comparison. A single main lobe for perpendicular incidence was also observed for spiral antennas in free-space by Dyson [57], and for integrated spirals by Grossman et al. [44] and Büttgenbach et al. [59]. In spite of the influence of the substrate, the measured patterns agree well with the theoretical pattern of a spiral antenna in free space calculated by Cheo et al. [60].

5. Pulse measurements

The application of short infrared radiation pulses gives information about the speed of the different conduction mechanisms in our Ni–NiO–Ni diodes. For this purpose, we have used our optical-free-induction-decay (OFID) system that produces 35-ps 10.6-μm CO_2-laser pulses with a repetition rate of 0.5 Hz. It is described briefly in the following together with the experimental arrangement for the measurement of the response of our diodes to the 35-ps 10.6-μm radiation pulses. Subsequently we present the results of these experiments, which include the polarization dependence of the signals, and the theoretical explanation of the thermal effects. Finally, we describe the pulse detection with the Ni–NiO–Ni diodes for zero bias voltage.

5.1. Experimental arrangement

The experimental setup for the pulse detection is presented in Fig. 40. The OFID system developed in our laboratory generates the 35-ps CO_2-laser pulses

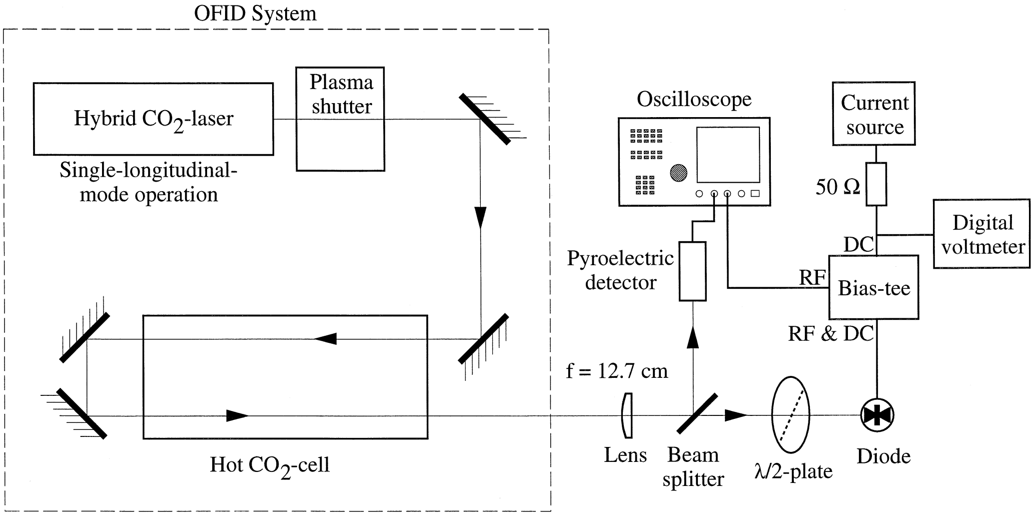

Fig. 40. Experimental arrangement for the detection of 35 ps 28 THz OFID CO_2-laser pulses.

[94–98]. Single-longitudinal-mode TEM_{00q} operation is achieved with a hybrid 10.6-μm CO_2-laser. The single-mode pulses emitted are truncated by a plasma shutter at the maximum truncation time of about 10 ps. This produces sidebands in the spectrum of the truncated pulse. The plasma shutter is followed by a cell of hot CO_2 that acts as filter which eliminates the central frequency without affecting the sidebands. The results are short 35-ps 10.6-μm pulses with an energy of typically 100 μJ. They are focused on the diode with a 12.7-cm-focal-length ZnSe lens. A reference signal is produced by a pyroelectric detector (Molectron P5-00, Cambell, USA). The linear polarization of the 10.6-μm laser radiation can be rotated with a half-wave plate. The thin-film Ni–NiO–Ni diode as target is biased with a current source over a 50-Ω resistance and a bias-tee. The bias voltage is measured and stabilized at typically 200 mV. The fast diode signal is recorded from the RF connection of the bias-tee with a 2-channel oscilloscope (TDS 620, Tektronix, Wilsonville, USA). The signal from the pyroelectric detector serves as a trigger. It is also registered with the oscilloscope. Furthermore, it gives information on the shot-to-shot variation of the pulse energy. The diode is mounted on an *x–y–z* stage and the incidence angle can be varied over a few degrees for alignment purposes. The laser radiation can be attenuated by calibrated teflon sheets in order to avoid high intensities that could destroy the diode.

The diodes used for these measurements have been equipped with bow-tie antennas. They were mounted in the configuration used for the first mixing experiments (Section 3.3.2) that made use of bonding wires as connections.

We have recorded the signals of over fifteen hundred OFID pulses with our MOM diodes under various conditions. In Section 5.2, we describe the general characteristics of the observed signals.

5.2. General characteristics of the diode response

The response of a thin-film Ni–NiO–Ni diode to 35-ps short pulses is represented in Fig. 41 together with the reference signal from the pyroelectric detector. The signal from the diode has a rise time of less than 1 ns. It is comparable with that of the reference signal and limited by the resolution of the oscillo-

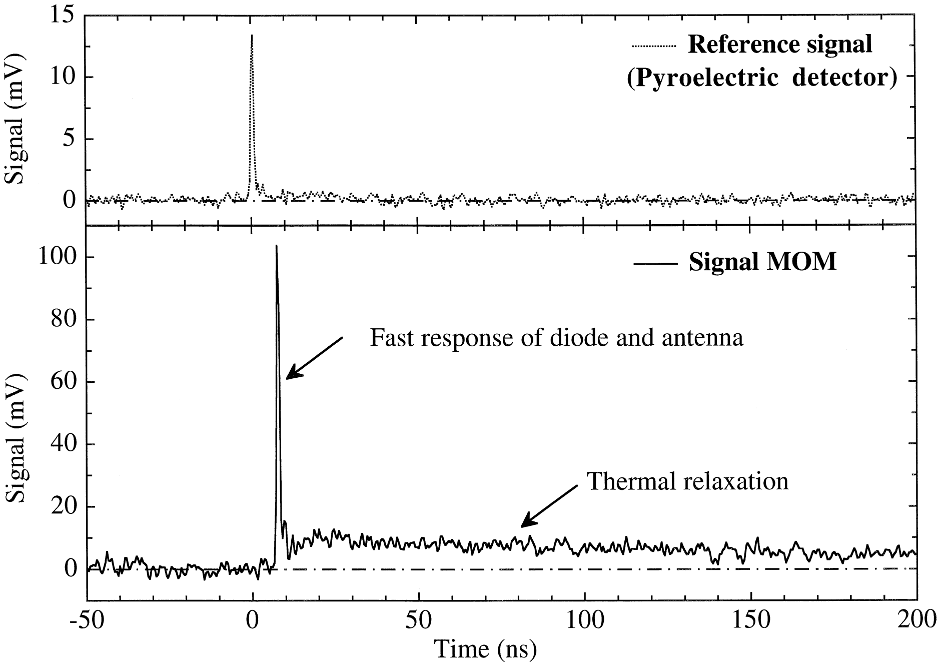

Fig. 41. Responses to a 35 ps 28 THz OFID CO_2-laser pulse.

scope, which has an RC-limited rise time of about 700 ps. Due to the characteristic response time of the apparatus, the signal rise is not resolved temporally.

After a fast peak the response exhibits a slower relaxation that contains the information on the thermal response speed of our diodes. The thermal relaxation times of the diodes are longer than the temporal resolution of our oscilloscope. This permits us to determine the general form of the measured relaxation. A good approximation of this relaxation is achieved by the sum of two exponential decay functions (Fig. 42). This reveals that at least two thermal processes are involved in the detection. The longer exponential decay time τ_1 is about 100 ns. It can probably be assigned to the thermal diffusion in SiO_2. The shorter decay time τ_2 of about 15 ns is probably related to thermal relaxation in Ni. A model that involves these exponential decays is presented in Section 5.4. The two time constants mentioned can vary slightly with the alignment of the diode.

Apart from the thermal relaxation there exists a fast response caused by rectification of the antenna currents in the diode. It is not observed in each response because it is attenuated and partly masked by the thermal effects.

Examples of measured responses are plotted in arbitrary units in Fig. 43b. The different forms observed can be simulated by varying the relative ratio of the different contributions as shown in Fig. 43a. For these simulations, the pulse rise is approximated by Gaussian functions with short characteristic times from 1 to 7 ns, and the decay by three exponential functions with decay times 100, 15 and 1 ns. The ratio of the signal amplitudes caused by two thermal contributions is taken 1:2 in favour of the faster thermal effect. This corresponds approximately to our measurements. Starting from the plot at the top, the magnitude of the antenna contribution is increased toward the bottom, i.e., the ratio *r* of the maximal amplitude of the antenna contribution to the

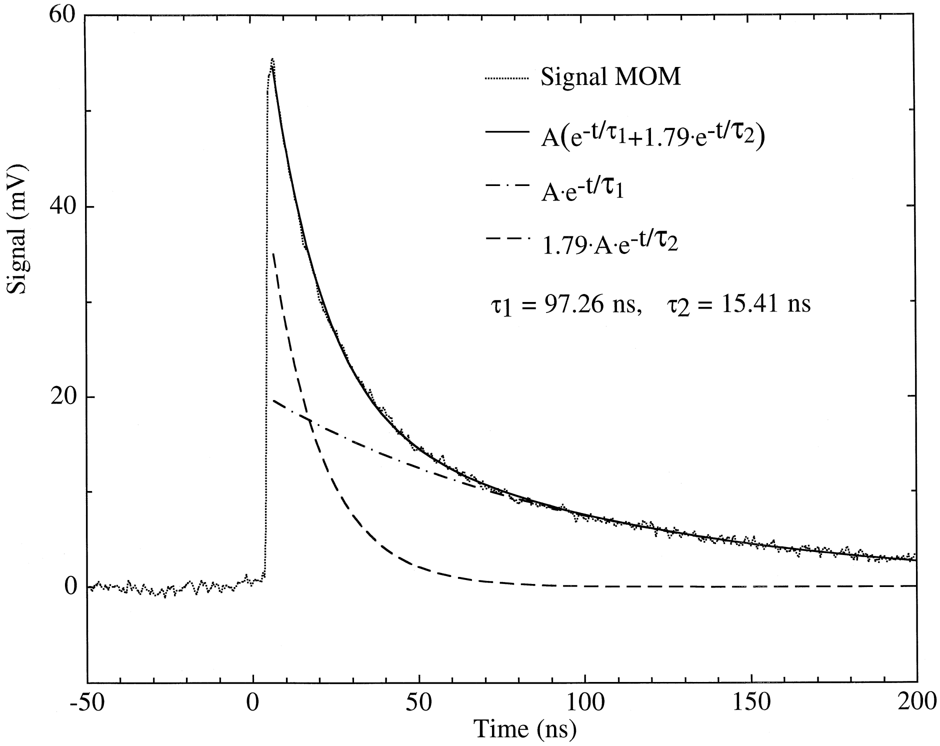

Fig. 42. Thermal response of the MOM diode to a 35 ps 28 THz CO_2-laser pulse.

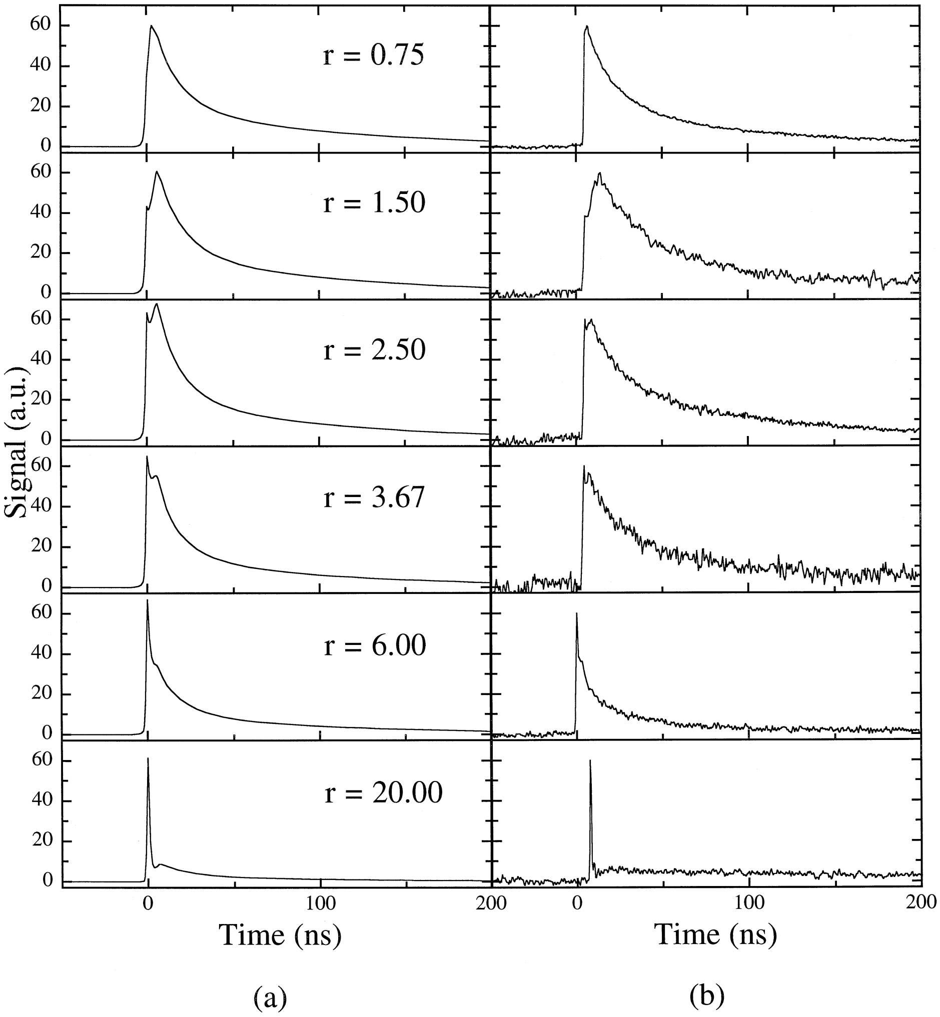

Fig. 43. Typical responses of the Ni-NiO-Ni diodes to 35 ps 28 THz CO_2-laser pulses: (a) Simulated pulses including three contributions with the amplitude ratio 1:2:r; (b) Measured pulses.

amplitude of the faster thermal effect contribution is increased.

5.3. Polarization dependence

As for the detection of cw 10.6-μm laser radiation the response of the MOM diodes to short pulses exhibits a dependence on the polarization of the incoming radiation. This polarization dependence is represented in Fig. 44 for a Ni–NiO–Ni diode connected to a bow-tie antenna with a half-length $L/2 = 2.3$ μm. It is the result of a measurement performed near normal incidence. The maximal amplitude of the response of the diode is plotted as a function of the polarization angle φ. The signal is calibrated with respect to the simultaneously registered response of the pyroelectric detector that determines the energy of each pulse. Each point of the figure corresponds to the measured calibrated signal averaged over four pulses. The measured peak voltage $V(\varphi)$ as a function of the polarization angle φ is appropriately described by the sum of a constant V_{ip} and a cosine squared function according to Eq. (4.1). As in the detection experiments of cw radiation, the

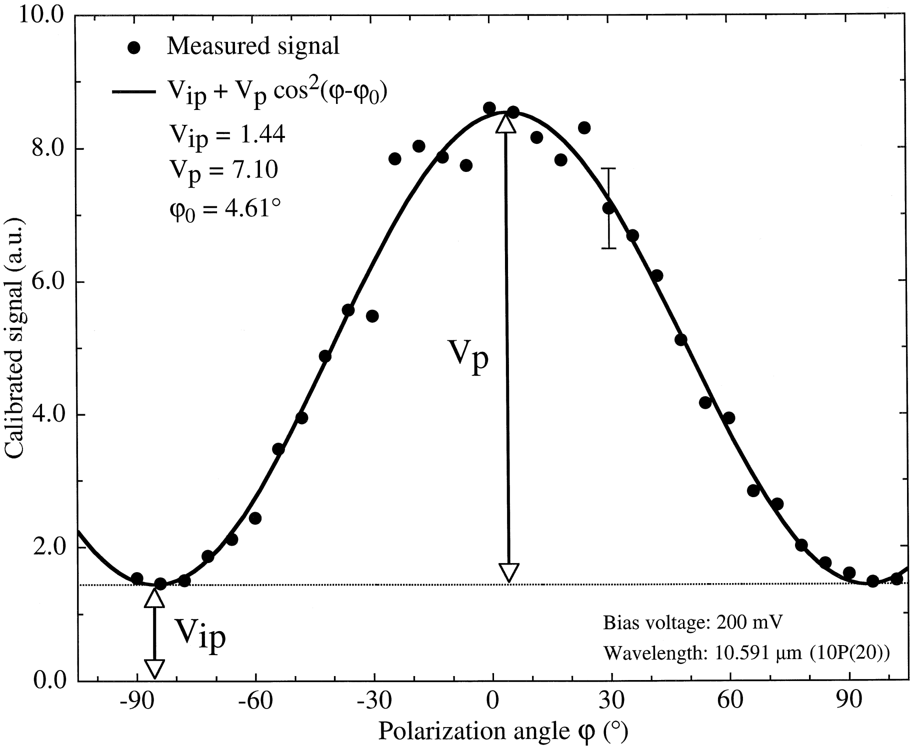

Fig. 44. Polarization dependence of the calibrated peak signal from our thin-film Ni-NiO-Ni diode integrated with a bow-tie antenna.

maximum of the curve described by φ_0 is located near 0°, corresponding to the polarization direction parallel to the antenna axis as expected. The value $\varphi_0 = 4.61°$ calculated from the measurement represented by Fig. 44 differs from 0°. This deviation can be explained by the experimental error. The ratio V_p/V_{ip} of the measurement illustrated in Fig. 44 equals 4.93. Other similar measurements yielded ratios between 4 and 5, much higher than the maximal ratio found for the detection of cw laser radiation. This can be explained by the fact that Fig. 44 characterizes the height of the fast peak which is in principle determined by the rectification of antenna currents in the diode. The polarization-independent thermal effects mostly determine the slower relaxation and contribute only little to the fast response.

5.4. The thermal response

The following calculation which describes the measured transient behaviour of the diode response can be applied to both relaxation effects. The thermal signal amplitude is proportional to the temperature increase δT in the diode area. Thermal diffusion in a bulk is described by the equation of heat conduction

$$\rho c \frac{\partial(\delta T)}{\partial t} - \lambda \Delta(\delta T) = 0 \text{ or}$$

$$\Delta(\delta T) - \frac{1}{D}\frac{\partial(\delta T)}{\partial t} = 0$$

$$\text{with } D = \lambda/\rho c, \tag{5.1}$$

where ρ (kg/m^3) is the density, c (J/kg K) the specific heat, λ (W/m K) the thermal conductivity of the medium and D (m^2/s) the thermal diffusivity.

In the following, we assume that an extremely short laser pulse that hits a plane sample causes a temperature rise δT with a two-dimensional radial distribution. We renounce a description by a three-dimensional distribution because the 1.5-μm SiO_2 layer is thin with respect to thermal diffusion. In addition, the SiO_2 layers as well as the Si substrate absorb only about 3% of the laser radiation. Therefore, we consider a two-dimensional radial distribution where the decay of $\delta T(r,t)$ can be approximated by the following solution of Eq. (5.1):

$$\delta T(r,t) = \delta T_0 J_0(r/r_0) e^{-t/\tau} \quad \text{for } r \le x_{01} r_0,$$
$$\delta T(r,t) = 0 \quad \text{for } r > x_{01} r_0, \tag{5.2}$$

with $r_0^2 = D\tau$ and $J_0(x_{01}) = 0$.

The function $J_0(x)$ represents the Bessel function of zero order [53] and $x_{01} = 2.4048$ its first zero. This approximation is based on two assumptions. First, we assume that for $r > x_{01} r_0$ the sample represents an infinite heat sink that suppresses any temperature rise, so that $\delta T \approx 0$. Secondly, we assume that the section of the short laser pulse whose absorption contributes to the temperature rise has the form

$$I(r,t) = I_0 \delta(t) J_0(r/r_0) \quad \text{for } r \le x_{01} r_0,$$
$$I(r,t) = 0 \quad \text{for } r > x_{01} r_0, \tag{5.3}$$

where the Dirac delta function $\delta(t)$ reflects the extremely short laser pulse. In view of our experiments, we should mention that our minimal estimates for the radius $r = x_{01} r_0$ resulted in 0.56 μm for SiO_2, 2.80 μm for Si and 1.27 μm for Ni. These estimated radii are reasonable because they are larger than the radius of the diode contact area, where the temperature rise causes an effect.

This model that describes the exponential behaviour of the thermal relaxation in the pulse measurements will be used also in Section 6 for the characterization of the influence of thermal effects in mixing experiments. The thermal characteristic times measured by pulse detection permits us to estimate the range of difference frequencies where the thermal effects play a role in the mixing process.

5.5. Zero-bias pulse detection

The response of a Ni–NiO–Ni diode to OFID pulses when no bias voltage is applied permits a reliable separation of the optical from the thermal effects. An example of response measured with $V_{bias} \approx 0$ V is represented in Fig. 45. In this case the fast response and the thermal signal exhibit opposite

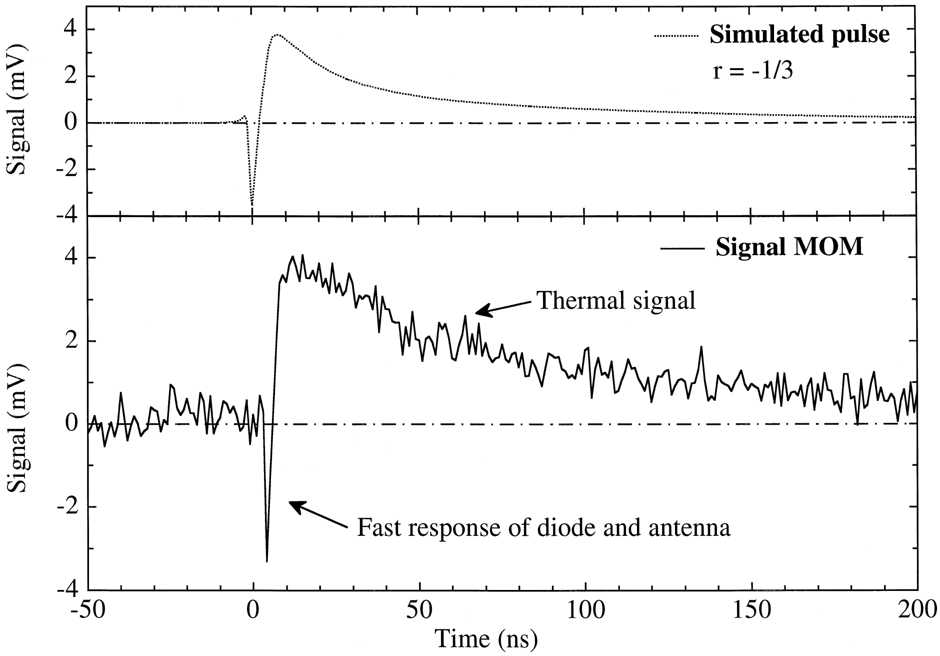

Fig. 45. Response of the unbiased diode to 35 ps 28 THz OFID CO_2-laser pulses and a simulated pulse including the three contributions with the amplitude ratio 1:2:r.

polarities. For an ideally symmetric MOM contact, no net rectified current is observed when the bias voltage applied to the diode is zero. However, in practical configurations of thin-film MOM diodes, the barrier tends to be asymmetric with a slightly lower barrier height on the side of the metal deposited first [27]. This explains that even for a bias voltage of zero, a small tunneling signal is observed. This fast signal due to field-assisted electron tunneling exhibits rise and decay times of less than 1 ns which represents the temporal resolution of the oscilloscope. The slower response that follows with an opposite sign is caused by the thermal effects and by the asymmetry of the configuration. The first deposited metal electrode of the diode is in direct contact with the substrate that is heated by absorption of radiation. The overlapping Ni arm has no direct contact with the substrate at the diode location, so that this electrode contains less thermally excited electrons. This results in a net flow of electrons through the barrier. The nature of the small asymmetry induces then the opposite sign of the contributions of the two effects when the bias voltage is kept at zero. The upper plot of Fig. 45 shows a simulated pulse similar to Fig. 43. The negative ratio r of Fig. 45 reflects the fact that the thermal and the optical contributions have opposite polarities.

6. Mixing experiments

Point-contact MOM diodes have been intensively used as mixers for absolute frequency measurements and high-resolution spectroscopy. In this section we describe the first successful mixing of 28-THz CO_2-laser radiation performed with our thin-film Ni–NiO–Ni diodes with integrated bow-tie antennas and integrated rhodium waveguides. These experiments resulted in the measurement of laser difference frequencies up to 176 GHz in mixing processes up to the fifth order by addition of microwaves generated by a Gunn oscillator.

6.1. Preliminary experiments

Preliminary mixing experiments of two 28-THz CO_2-laser emissions with our Ni–NiO–Ni diodes were made at LENS (Florence, Italy). They resulted in the generation of difference frequencies up to 85 MHz between two CO_2 lasers oscillating on the same transition in the 10P-branch and tuned over the Doppler gain curve [78]. The diodes used on this occasion were mounted in the configuration presented in Section 3.3.2 (Fig. 17) with bonding-wire connections. They were based on silicon substrates with a resistivity of 3 to 5 Ω cm. Because of the considerable attenuation of signals at GHz frequencies caused by the bonding wires, the substrate losses and the unfavourable structure on the chip mixing at higher difference frequencies was not possible.

On this occasion we demonstrated that the second-order mixing signal amplitudes measured with our thin-film Ni–NiO–Ni diodes are proportional to the second derivative of the static $I(V)$ characteristics according to Eq. (2.2). The mixing-signal amplitude shows therefore a linear dependence on the square root of the product of the power of the two lasers. The results from these first mixing experiments indicated the potential of our diodes concerning mixing of adjacent CO_2-laser emissions with difference frequencies in the order of 60 GHz.

6.2. Experimental arrangement

During our following mixing experiments performed at the Physikalisch-Technische Bundesanstalt (PTB, Braunschweig, Germany) we detected considerably higher difference frequencies between two adjacent or close 28-THz CO_2-laser transitions in the 10P branch [99,100]. On this occasion, we used thin-film Ni–NiO–Ni diodes with a contact area of approximately 110 nm × 110 nm connected to the integrated bow-tie antennas that exhibit the best detection signals. These antennas possess an overall length of 4.6 μm corresponding to $3/2$ of the substrate wavelength of incident 10.6-μm radiation (Section 4.3.4). The diodes were mounted in the improved high-frequency configuration described in Section 3.3.3 with flip-chip connections and novel integrated rhodium waveguides. The diodes and antennas were consequently irradiated from the back side of the chip. They were supported by low losses high-resistivity (>3 kΩ cm) silicon substrates coated on both sides with 1.5-μm SiO_2-layers.

The experimental setup for mixing two CO_2-laser emissions at room temperature is illustrated in

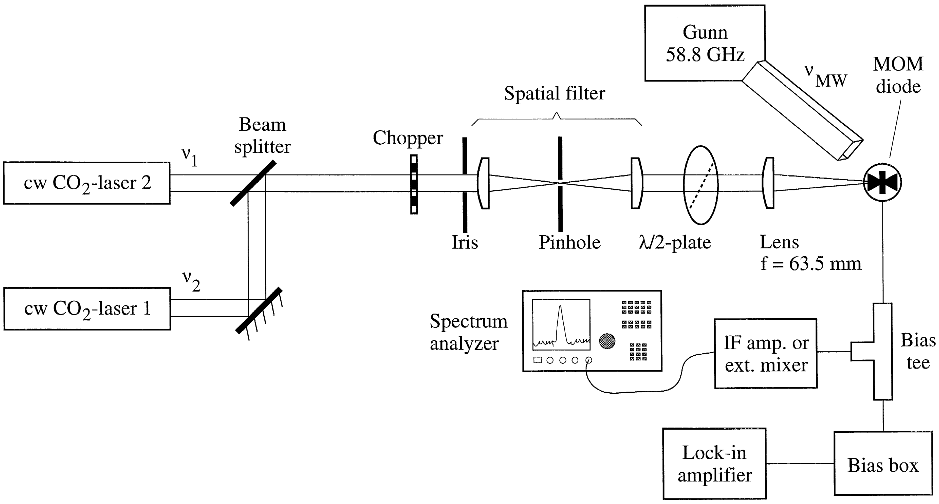

Fig. 46. Experimental arrangement for mixing experiments with cw 28 THz CO$_s$-Laser radiation.

Fig. 46. The two tunable CO$_2$ lasers constitute part of the permanent frequency-measurement chain of the PTB [101]. The CO$_2$-laser emissions used in our experiments are listed in Table 4(Ref. [102]). The colinearly combined infrared beams were spatially filtered through a pinhole and focused onto the Ni–NiO–Ni diode with a lens of 63.5 mm focal length at an incidence angle of approximately 8° to prevent back reflection in the beam axis. The linear polarization of the infrared radiation, identically oriented for the two lasers, was rotated with a CdS half-wave plate. The total laser power on the diode was controlled with an iris and kept at approximately 400 mW for all the measurements. The alignment of the diode and the colinearity of the two lasers were optimized by measuring the dc output signal of the diode when used as detector. For this purpose, the beam was mechanically modulated by a chopper with a frequency of 170 Hz, while the rectified signal was measured with a lock-in amplifier. The bias voltage applied to the diode was in all the experiments limited to 200 mV, which constitutes a safe working condition for our thin-film diodes.

Table 4
Frequencies and wavelengths of the vibrational–rotational CO$_2$-laser transitions [102] used in our mixing experiments

CO$_2$-laser emission	Frequency (THz)	Wavelength (μm)
10P(30)	28.0274319	10.7640602
10P(32)	27.9694499	10.7411219
10P(34)	27.9107213	10.7185683
10P(36)	27.8512433	10.6963942

In the second-order mixing experiments, the difference-frequency signals of over 50 GHz between two adjacent CO$_2$-laser lines were transmitted by HF coaxial cables (Wiltron-V) to a high-sensitivity microwave receiver for the 40–60 GHz band that was developed at the Swiss Post Office Research Laboratory (PTT, Bern, Switzerland). This external mixing of the beat signals with a tunable microwave source yielded signals in the 10–500 MHz range which were monitored on a spectrum analyzer. For the measurement of beat signals in the MHz range between the CO$_2$-lasers oscillating on the same transition, the IF-signals were preamplified and displayed on the spectrum analyzer.

The detection of the higher-order mixing processes required microwave radiation generated by a Gunn oscillator working at the frequencies 58.8 GHz ± 50 MHz with a power of 100 mW. For this purpose the diode was irradiated with the microwaves emitted from the open end of a hollow waveguide at a distance of 2 cm to 3 cm. The mixing signals were measured with the spectrum analyzer after 32-dB preamplification. The mixing processes performed with this arrangement are listed in Table 5.

Table 5
Mixing performed with thin-film Ni–NiO–Ni diodes

Mixing process	Mixing order	Laser difference frequency $\Delta\nu$	S/N ratio (dB)	Bandwidth (kHz)	Polarization contrast (dB)
Beat 10P(30)–10P(30) (e.g.)	2	0.5 to 70 MHz	61	100	14–22
10P(32)–10P(34) (external mixing)	2	58.73 GHz	22	100	34.4
10P(32)–10P(34) + MW 58.8 GHz	3	58.73 GHz	47	100	34.4
10P(30)–10P(30):2 × $\Delta\nu$	4	12 MHz	8	100	–
10P(30)–10P(34) + 2 × MW 58.8 GHz	4	116.71 GHz	19	100	> 25
10P(36)–10P(30) + 3 × MW 58.8 GHz	5	176.19 GHz	14	300	–

In Sections 6.3, 6.4 and 6.5, the results are presented in detail, first for second-order and then for higher-order mixing.

6.3. Second-order mixing

Second-order mixing and detection by MOM diodes are determined by the second-order term in the Taylor expansion of the current I as a function of the voltage V for the bias voltage V_{bias} applied. The nonlinearity of MOM diodes for frequencies in the 28-THz region follows the dc $I(V)$ characteristics as demonstrated by Klingenberg and Weiss [103] and verified by Fumeaux et al. [78] for our thin-film Ni–NiO–Ni diodes. Thus, the second derivative of the $I(V)$ curve measured at 10 kHz describes adequately the detection and second-order mixing response in all our experiments performed with CO_2-laser radiation. The $I''(V)$ characteristic of the diodes used for the present experiments (Fig. 22) is symmetric with respect to the zero-bias point. It shows a saturation of the linear behaviour observed in 1996 by Fumeaux et al. [78].

The second-order mixing of the 10P(32) and 10P(34) transitions of the CO_2-lasers with a difference frequency $\Delta\nu \approx 58.7$ GHz was measured with our thin-film MOM diode as described in Section 6.2. It showed a signal-to-noise (S/N) ratio of 22 dB with a 100 kHz resolution bandwidth (RBW) at a bias voltage of 160 mV. A monotonous increase of the signal with the bias voltage was observed with a saturation above 160 mV in agreement with the $I''(V)$ curve of Fig. 22.

Beat signals between the two CO_2-lasers oscillating at the same transition, e.g. 10P(30), and tuned on the gain curve of the lasers by means of piezoelectric elements were measured with frequencies between 500 kHz and 70 MHz and S/N ratios up to 61 dB (100 kHz RBW). The discrepancy between the magnitude of the signals in the MHz and GHz range is explained by the contribution of the thermal effects at frequency in the MHz range on one hand and by the partial coupling of the 58.7 GHz signal into the coplanar rhodium waveguide on the other hand. Additional losses in the rhodium and succeeding gold waveguides and connectors are 4 to 5 dB.

The amplitude of the beat signal as a function of the polarization angle φ is represented in Fig. 47 in a linear scale for the second-order mixing of the 10P(32) and 10P(34) transitions with a difference frequency of 58.7 GHz. In agreement with antenna theory, the dependence on φ is well described by the sum of a small constant V_{ip} and a squared cosine with amplitude V_{p}. This corresponds to the polarization dependence of detection signals of Eq. (4.1). The maximal polarization response with respect to the bow-tie antenna axis occurs for the polarization parallel to the antenna, i.e., for $\varphi_0 \approx 0°$. The small deviation of the angle φ_0 from 0° can be explained by the experimental errors of the positioning of the diode, the polarization of the lasers and the calibration of the half-wave plate. Eq. (4.1) permits an interpolation of data also for signals under the noise level. It yields a contrast ratio $V_{\mathrm{p}}/V_{\mathrm{ip}}$ of 52.21 corresponding to 34.4 dB in a logarithmic scale. This almost perfect polarization dependence at the difference frequency of 58.7 GHz demonstrates the complete linear polarization of our bow-tie antenna as predicted by the antenna theory of microwave techniques [48]. This can be explained by the fact that in our range of difference frequencies, the polarization-independent thermal effects are too slow to influence the mixing signal.

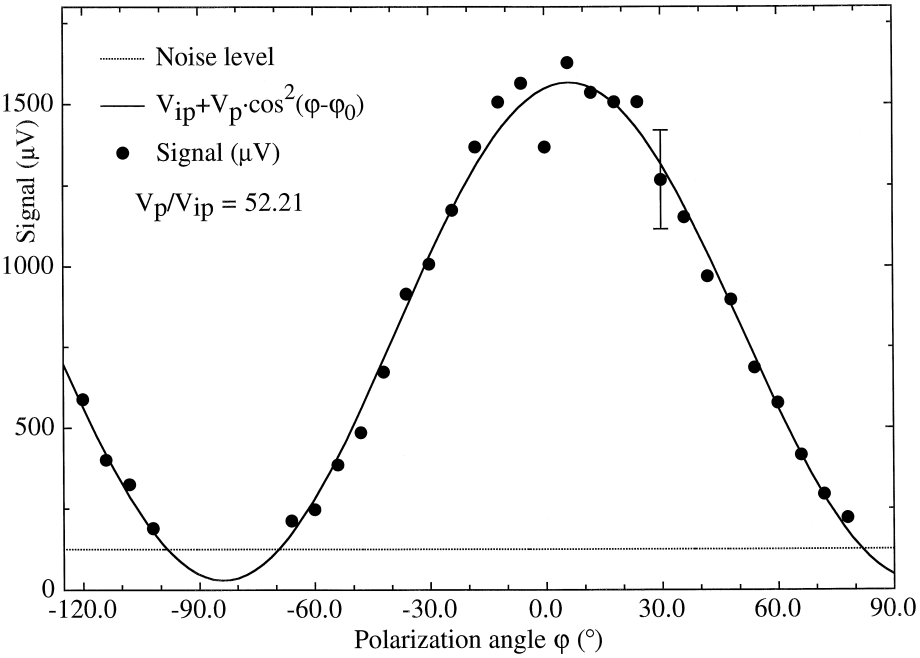

Fig. 47. Polarization dependence of the signal amplitude of the second-order mixing of the CO_2-laser transitions 10P(32) and 10P(34) with a difference frequency of 58.7 GHz.

6.4. Dependence of the thermal response on the difference frequency

The difference-frequency dependence of the polarization ratio V_p/V_{ip} was also measured between 0.5 and 70 MHz by making use of the beat signal of the radiation of the two lasers oscillating on the 10P(30) transition. The measured ratios V_p/V_{ip} of the response for the polarization parallel to the antenna axis vs. the response for the cross-polarization are represented in Fig. 48 as functions of the difference frequency $\Delta\nu$, together with the ratio at 58.7 GHz. The circles indicate the measurements performed with a thin-film Ni–NiO–Ni diode mounted in the flip-chip configuration and supported by the high-resistivity substrate. The squares indicate the measured ratios for a diode used for the preliminary mixing experiments [78] making use of bonding-wire connections and 3–5 Ω cm silicon for the substrate. The error associated with these measurements is ±0.5 dB for each point. The difference-frequency dependence of this ratio is explained by the fact that the polarization-independent thermal contributions to the mixing signal are slow and disappear for difference frequencies $\Delta\nu$ above a few megahertz.

The description of the influence of the thermal effects in the mixing experiments is made on the basis of the model already presented in Section 5.4 for pulse detection measurements. In the case of mixing, the laser power $I(r,t)$ absorbed per unit volume has a radial distribution and a component modulated at the beat circular frequency $\Delta\omega = 2\pi\Delta\nu$. This component causes a temperature modulation $\delta T(r,t)$ at the beat frequency that is determined by the equation of heat conduction as follows

$$\rho c\frac{\partial(\delta T)}{\partial t} - \lambda\Delta(\delta T) = I(r,t)$$

$$= I(r)(1+\cos(\Delta\omega t))$$

$$\text{or}\quad \Delta(\delta T) - \frac{1}{D}\frac{\partial(\delta T)}{\partial t} + \frac{I(r)}{\lambda}(1+\cos(\Delta\omega t)) = 0. \qquad (6.1)$$

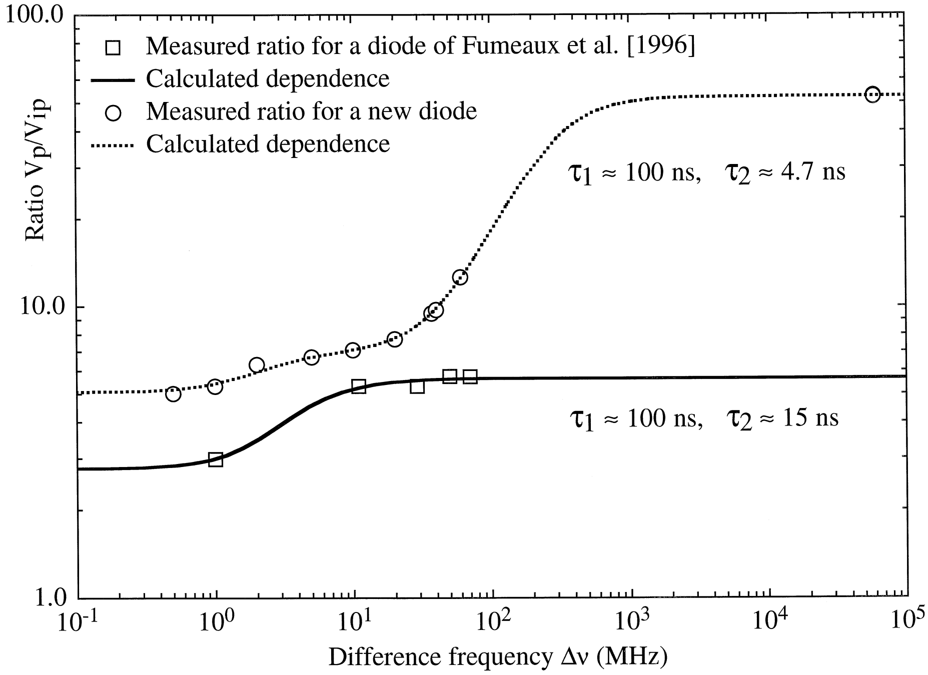

Fig. 48. Dependence of the ratio V_p/V_{ip} of the signal amplitudes for the polarization parallel to the antenna axis and for the cross polarization on the difference frequency $\Delta\nu$.

As in Section 5.4 this equation can be solved if one assumes for the power modulation a radial distribution described by the Bessel function $J_0(x)$ of zero order

$$I(r) = I_0 J_0(r/r_0) \quad \text{for } r \le x_{01} r_0,$$
$$I(r) = 0 \quad \text{for } r > x_{01} r_0, \tag{6.2}$$

with $r_0^2 = D\tau$ and $J_0(x_{01}) = 0$.

The particular solution of Eq. (6.1) with the assumption of Eq. (6.2) yields the dependence of the amplitude of the temperature modulation $\delta T(r,t)$ with respect to the difference circular frequency $\Delta\omega$

$$\delta T(r,t) = \frac{D\tau}{\lambda} \frac{I_0}{\sqrt{1+(\Delta\omega\tau)^2}} J_0(r/r_0) \times (1+\cos(\Delta\omega t - \varphi)) \tag{6.3}$$

for $r \le x_{01} r_0$ and $\varphi = \arctan(\Delta\omega\,\tau)$.

The amplitude of the thermal beat signal is proportional to the part of this temperature modulation $\delta T(r,t)$ oscillating with the circular frequency $\Delta\omega$ and the phase retardation φ. The total oscillating signal $V_{\text{total}}(t)$ is the sum of the two thermal contributions with the amplitudes $A_{\text{th},1}$, $A_{\text{th},2}$ and the optical contribution with the amplitude A_{opt}

$$V_{\text{total}}(t) = A_{\text{opt}}\cos(\Delta\omega t) + A_{\text{th},1}(\Delta\omega) \times \cos(\Delta\omega t - \varphi_1) + A_{\text{th},2}(\Delta\omega) \times \cos(\Delta\omega t - \varphi_2) \tag{6.4}$$

with the corresponding thermal amplitudes and phases

$$A_{\text{th},1\&2}(\Delta\omega) = \frac{A_{\text{th},1\&2}(0)}{\sqrt{1+(\Delta\omega\tau_{1\&2})^2}} \text{ and}$$
$$\varphi_{1\&2} = \arctan(\Delta\omega\tau_{1\&2}). \tag{6.5}$$

By taking account of trigonometric relations, the total signal $V_{\text{total}}(t)$ can also be represented by

$$V_{\text{total}}(t) = A_{\text{total}}(\Delta\omega)\cos(\Delta\omega t - \varphi_{\text{total}}) \tag{6.6}$$

with the total amplitude $A_{\text{total}}(\Delta\omega)$ that is given by

$$A_{\text{total}}(\Delta\omega) = \left(A_{\text{opt}}^2 + A_{\text{th},1}^2(\Delta\omega) + A_{\text{th},2}^2(\Delta\omega) + \text{phase terms}\right)^{1/2} \tag{6.7}$$

with the phase terms

$$2A_{\mathrm{opt}}(A_{\mathrm{th},1}(\Delta\omega)\cos\varphi_1 + A_{\mathrm{th},2}(\Delta\omega)\cos\varphi_2) + 2A_{\mathrm{th},1}(\Delta\omega)A_{\mathrm{th},2}(\Delta\omega)\cos(\varphi_1-\varphi_2). \quad (6.8)$$

$A_{\mathrm{th},1}(\Delta\omega)$, $A_{\mathrm{th},2}(\Delta\omega)$, φ_1 and φ_2 are described by Eq. (6.5). The ratio $V_{\mathrm{p}}/V_{\mathrm{ip}}$ can be calculated by the relation

$$\frac{V_{\mathrm{p}}}{V_{\mathrm{ip}}}(\Delta\omega) = \frac{\text{Signal amplitude for parallel polarization}}{\text{Signal amplitude for perpendicular polarization}} = \frac{A^{\|}_{\mathrm{total}}(\Delta\omega)}{A^{\perp}_{\mathrm{total}}(\Delta\omega)} \quad (6.9)$$

with the $A^{\|}_{\mathrm{total}}(\Delta\omega)$ and $A^{\perp}_{\mathrm{total}}(\Delta\omega)$ determined by Eq. (6.7).

The curves of Fig. 48 have been calculated according to this model. The calculated full curve is characterized by the time constants $\tau_1 = 100$ ns and $\tau_2 = 15$ ns which were measured on identical diodes in the first configuration by short-pulse detection experiments. It shows an asymptotical behaviour of the ratio $V_{\mathrm{p}}/V_{\mathrm{ip}}$ already in the MHz range. On the contrary, the new thin-film MOM diodes do not exhibit this asymptotical behaviour of the $V_{\mathrm{p}}/V_{\mathrm{ip}}$ curve under 70 MHz. A monotonic increase is observed which culminates in a ratio of 52.2 for the difference frequency of 58.7 GHz. This suggests a thermal time constant shorter than those of the previous diodes and a contact area even smaller than stated before. In our fitting procedure, the time constant of the thermal diffusion in the SiO_2-layer of our substrate was kept at the measured value of $\tau_1 = 100$ ns, while the second time constant τ_2 for the diffusion in Ni, which is crucially dependent on the geometry of the Ni-layer and on the contact area, was taken as a free parameter. The fitting yielded $\tau_2 \approx 4.7$ ns and resulted in the dotted curve of Fig. 48.

For our diode manufactured on the high-resistivity silicon ($> 3\ \Omega$ cm), the following two extremes can be deduced from the experimental data presented in Fig. 48

$$\frac{V_{\mathrm{p}}}{V_{\mathrm{ip}}}(0) = \frac{A^{\|}_{\mathrm{opt}} + A_{\mathrm{th},1}(0) + A_{\mathrm{th},2}(0)}{A^{\perp}_{\mathrm{opt}} + A_{\mathrm{th},1}(0) + A_{\mathrm{th},2}(0)} \approx 5.1,$$

$$\frac{V_{\mathrm{p}}}{V_{\mathrm{ip}}}(\infty) = \frac{A^{\|}_{\mathrm{opt}}}{A^{\perp}_{\mathrm{opt}}} \approx 52.2. \quad (6.10)$$

$A^{\|}_{\mathrm{opt}}$ and $A^{\perp}_{\mathrm{opt}}$ represent the signal amplitudes due to antenna coupling for the polarization parallel and perpendicular to the antenna axis.

6.5. Higher-order mixing

Higher difference frequencies between CO_2-laser transitions were also measured in third-, fourth- and fifth-order mixing processes. For this purpose, the thin-film Ni–NiO–Ni diode was irradiated by microwaves generated by a Gunn oscillator working at the frequencies of 58.8 GHz ± 50 MHz as well as by the two CO_2-laser beams. The mixing signal was measured at the frequency

$$\nu_{\mathrm{measured}} = |(\nu_1 - \nu_2) - (n-2)\nu_{\mathrm{MW}}|, \quad (6.11)$$

where ν_1 and ν_2 represent the CO_2-laser frequencies, ν_{MW} the frequency of the Gunn oscillator, and $n = 2, 3, 4, 5$, the mixing order.

A third-order mixing signal ($n = 3$) at a frequency $\nu_{\mathrm{measured}} = 109$ MHz is displayed in Fig. 49. It exhibits a 47-dB S/N ratio (100 kHz RBW). This is the result of a measurement with the unbiased diode. At present, mechanism and efficiency of the coupling of microwave radiation to our structures are unknown. The coupling that probably occurred via the connections was optimized by moving the position of the hollow waveguide relative to the diode. Polarization and incidence angle of the microwave radiation are not critical. Therefore third-order mixing signals with an S/N ratio of 30 dB (100 kHz RBW) were easily achieved even with unfavourable microwave irradiation.

The third-order mixing signal is proportional to the third-order coefficient of the Taylor expansion of the current I as a function of the voltage V across the diode. Fig. 50 represents the smoothed calculated third derivative $I'''(V)$ that is proportional to this coefficient. This third derivative was evaluated numerically with the smoothed $I''(V)$ curve of Fig. 22. Also represented in Fig. 50 is the relative magnitude of the third-order mixing signal in arbitrary units as a function of the bias voltage. It shows the same behaviour as the third derivative $I'''(V)$ with a maxi-

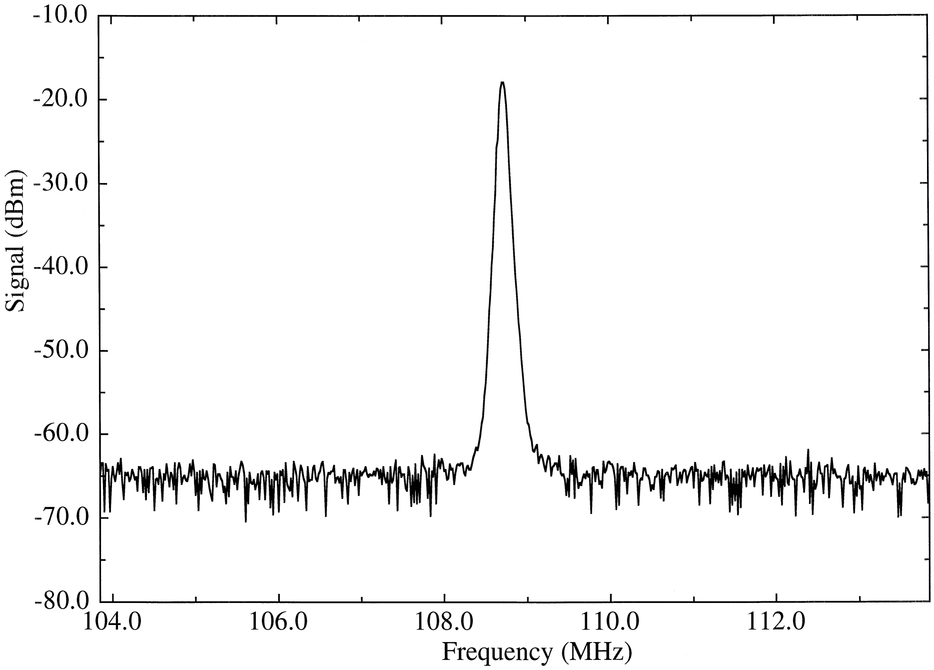

Fig. 49. Signal of third-order mixing ($n = 3$) between the two CO_2-laser emissions 10P(32) and 10P(34) and a Gunn oscillator working at 58.8 GHz. The two CO_2-laser emissions, each with a power of ≈ 200 mW, are polarized parallel to the antenna axis. The bandwidth of the spectrum analyzer is 100 kHz.

mum for zero-bias voltage. Because of the symmetry of the contact, the same points are taken for positive and negative bias voltages. Consequently, the $I(V)$ characteristics measured at 10 kHz describes accurately the nonlinearity for frequencies up to at least 28 THz.

The dependence of the third-order mixing signal on the polarization of the incident CO_2-laser radiation was also measured. It is represented in Fig. 51 in a linear scale. The signal is below the noise level for the polarization perpendicular to the antenna axis. The interpolation of the data below the noise level is performed by fitting with the aid of Eq. (4.1). This yields a ratio of the amplitude of the response for polarization and cross-polarization of 52.14 or 34.3 dB in perfect accordance with the analogue measurement of second-order mixing with the difference frequency of 58.7 GHz presented in Fig. 47.

Fourth-order mixing was measured in two different ways. First, we measured a signal with a frequency $\nu_{\text{measured}} \approx 900$ MHz by mixing the 10P(30) and 10P(34) CO_2-laser transitions with the second harmonic of the 58.8 GHz microwaves generated by the Gunn oscillator ($n = 4$). This resulted in a S/N ratio of 19 dB (100 kHz RBW). In this measurement, we observed a monotonic increase of the amplitude of the signal for increasing bias voltage. The symmetry of our contact explains the necessity of a bias voltage for even order mixing processes because the corresponding terms of the $I(V)$ expansion almost vanish for zero V_{bias} [104]. Fourth order-mixing was also demonstrated without microwave illumination with a weak S/N ratio of 8 dB. For this purpose we measured simultaneously the beat signal of the two CO_2-lasers oscillating on the 10P(30) transition with a difference frequency of 6 MHz and the second harmonic of this beat signal at 12 MHz. The measured ratio of the amplitude of the beat signal vs. the amplitude of its second harmonic was -52 dB. The contribution to the amplitude of the second harmonic caused by the nonlinearity of amplifier and circuitry was measured at the frequency of 6 MHz which was generated by a frequency synthesizer. The amplifier and the circuitry produced the second harmonic at a

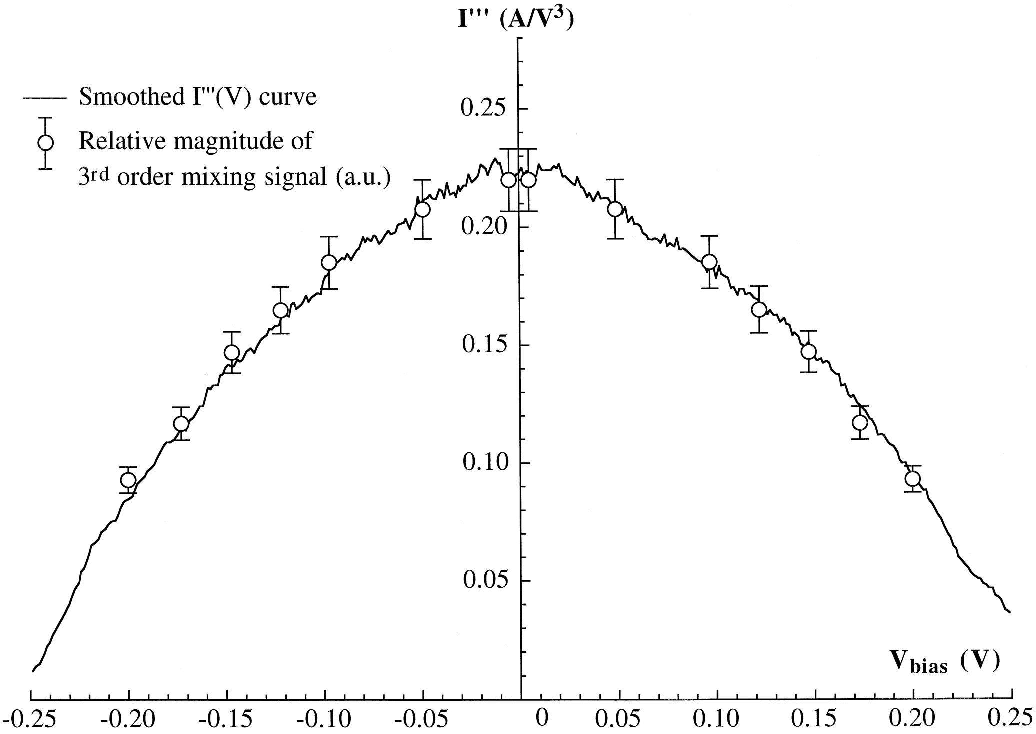

Fig. 50. Third derivative $I'''(V)$ of the static current-voltage characteristics $I(V)$ compared with the relative amplitudes of third-order mixing signals as a function of the bias voltage V_{bias}.

frequency of 12 MHz with a relative ratio of -60 dB. The 8-dB difference between the two measurements is therefore attributed to harmonic generation in the Ni–NiO–Ni diode. The weak S/N ratio resulting from this calculation reflects the lower level of even-order mixing signals already reported for point-contact diodes [105].

The highest laser difference frequency of 176.2 GHz measured with our thin-film MOM diodes was obtained by fifth-order mixing ($n = 5$) of the 10P(36) and 10P(30) transitions of the CO_2-lasers and the third harmonic of the 58.8 GHz microwaves. The resulting signal has a frequency $\nu_{\mathrm{measured}} \approx 230$ MHz and a maximal S/N ratio of 14 dB (300 kHz RBW). The low S/N is not the consequence of the high difference frequency yet of the fast decrease of the S/N ratio with increasing mixing order n. For an odd mixing order n_{odd} an S/N ratio decreasing as

$$S/N \approx \mathrm{const} \cdot n_{\mathrm{odd}}^{-7.4} \tag{6.12}$$

was reported for point-contact diodes by Sakuma and Evenson [105]. A direct comparison of our experiments with this dependence would require mixing data at higher orders and identical optimization of all the different mixing steps. However, the tendency of our results is in accordance with the measurements on point-contact diodes.

6.6. Future aspects

Our experiments represent the first mixing of 28-THz laser radiation with difference frequencies up to 176 GHz for nonlinear processes up to the fifth order. At difference frequencies in the GHz range, the polarization-independent thermal effects that are observed at lower difference frequencies and in detection experiments are too slow to contribute to the mixing process. This explains that the ratio $V_{\mathrm{p}}/V_{\mathrm{ip}}$ of the signal for the polarization parallel to the antenna axis vs. the signal for the cross-polarization increases as a function of the difference frequency

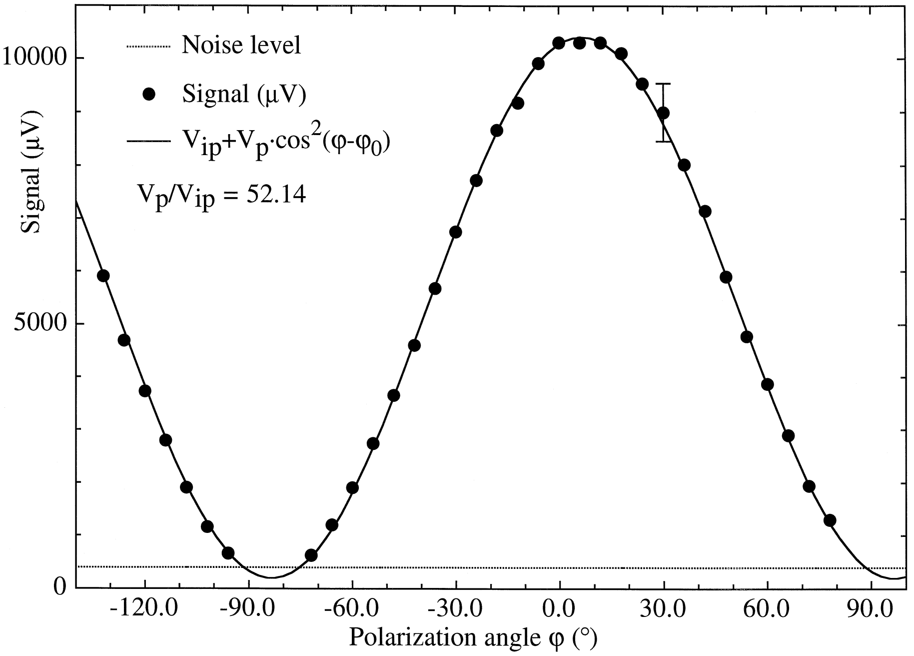

Fig. 51. Polarization dependence of the signal of third-order mixing between the CO_2-laser emissions 10P(32) and 10P(34) and microwaves generated by the Gunn oscillator at a frequency of 58.8 GHz.

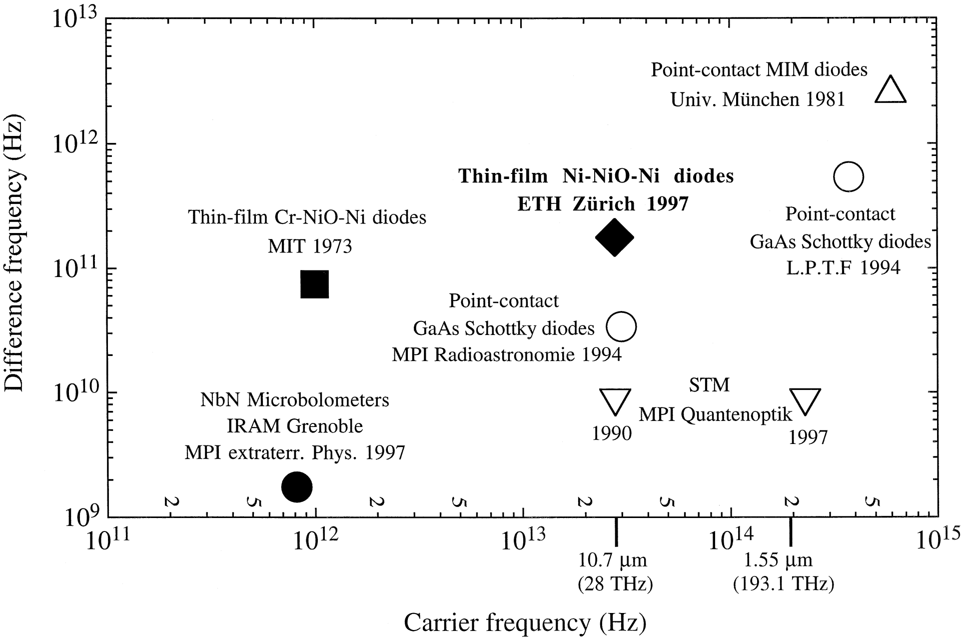

Fig. 52. Historical development of point contact mixers (white) and thin-film mixers (black) with respect to carrier and difference frequencies. References: Point-contact MIM diodes [4,26], Schottky point-contact diodes [26,107], scanning tunneling microscope ([108], Krieger, 1977), thin-film Cr-NiO-Ni diodes [12], NbN bolometers [109].

and reaches the asymptotic value of 52.2 at a difference frequency of 58.7 GHz. This high ratio demonstrates the efficiency and perfect polarization of our integrated resonant bow-tie antenna with an arm length of 4.6 μm. The mixing experiments with high difference frequencies permitted the elimination of the masking thermal effects in the study of our planar infrared antennas.

As for point-contact MOM diodes, the static $I(V)$ characteristics of our thin-film Ni–NiO–Ni diodes describe correctly the nonlinearity of the device for infrared frequencies up to at least 28 THz. The signals measured are proportional to the derivative of this $I(V)$ characteristics corresponding to the mixing order. The detailed knowledge of this $I(V)$ curve and its Taylor expansion permits to optimize the bias voltage applied to the diode in order to maximize the mixing-signal amplitude.

Higher difference laser frequencies by the mixing of 28-THz radiation with our thin-film diodes can be achieved in higher-order mixing processes. However, the rapid decrease of the S/N ratio of the mixing signal with increasing mixing order suggests the application of microwave sources with higher frequencies, e.g., 200-GHz klystrons, in a low-order mixing process.

The S/N ratios of 14 to 47 dB measured with our thin-film diodes are still below those which resulted from the corresponding measurements on point-contact MOM diodes [104–106]. The performance of our diodes can be improved by narrower focusing of the infrared radiation and by a more efficient coupling of the microwave radiation to the diode. The demonstration of the generation of difference frequencies with our thin-film Ni–NiO–Ni diodes has revealed that the present contact area of 110 nm × 110 nm yields a response to 10.7-μm CO_2-laser radiation within times of about 36 fs.

The historical progress of point-contact and thin-film mixers is represented in Fig. 52 from the perspective of the maximal attained carrier- and difference-frequencies. MOM diodes were demonstrated to work up to the visible range [4,25] yet with poor sensitivity. Promising devices for heterodyne measurements at 10 μm wavelength [107] and in the visible range [26] are Schottky point-contact diodes and the scanning tunneling microscope (Ref. [108]; W. Krieger, Max-Planck-Institut für Quantenoptik, 8046 Garching, Germany, private communication, 1997). The extreme-frequency operation of thin-film devices involves severe problems, yet represents an alternative leading to the realization of more stable and reproducible devices that could be integrated in arrays. The mixing of 300-μm radiation performed by Small et al. [12] with thin-film Cr–NiO–Ni diodes remained the unsurpassed limit for over 20 years. The mixing of 10.7-μm radiation with our thin-film Ni–NiO–Ni diodes constitutes an important step forward that demonstrates that thin-film diodes can achieve the performance of point contacts. At present other thin-film devices like NbN bolometers [109] and superconductor–isolator–superconductor (SIS) contacts [110] are well suited for low-noise astronomical applications with frequencies up to 1 THz.

7. Conclusions

In this study we have reported on the fabrication of thin-film Ni–NiO–Ni diodes with a minimum contact area of 110 nm × 110 nm (0.012 μm^2). To our knowledge our MOM diodes are the smallest thin-film diodes ever manufactured. They are fabricated on SiO_2/Si substrates with the help of electron-beam lithography and possess contact areas with dimensions in the range of those of point-contact diodes. Our diodes are connected to integrated infrared dipole, bow-tie and spiral antennas that couple 28-THz CO_2-laser radiation and permit detection and mixing.

The nonlinearity of our thin-film diodes up to at least 28 THz can be described by the second derivative of the $I(V)$ characteristics measured at 10 kHz. The detection signals and second-order mixing signals are proportional to this second derivative, whereas higher-order mixing is described by the derivative corresponding to the mixing order. The typical second derivative $I''(V)$ as a function of the bias voltage applied to the diode is linear for low bias. As the bias voltage is increased, $I''(V)$ exhibits a saturation followed by a maximum. The zero-bias resistance R_0 of the thin-film diodes investigated in this study is in the order of 100 Ω. The deviation from an inversely proportional dependence of R_0 on the contact area of the diode shows the presence of a contribution from spreading resistance besides the generally accepted electron tunneling mechanism.

The measurement of the dc signals generated by the diodes with integrated linear polarized antennas when irradiated with a CO_2-laser permits the distinction between a polarization-dependent contribution V_p caused by antenna-coupling and a polarization-independent contribution V_{ip} that is mainly of thermal origin. The polarization-independent part of the signal shows no dependence on the contact area and the type of integrated antenna. On the contrary, the polarization-dependent antenna signals are superior for smaller contacts and depend explicitly on the type of antenna. The overall best responsivities of linearly polarized integrated antennas are achieved by diodes connected to a bow-tie antenna with a total length of 4.6 μm. This length corresponds to $3/2$ of the substrate wavelength of 10.6 μm CO_2-laser radiation. The maximal amplitude ratio V_p/V_{ip} of the polarization-dependent signal to the polarization-independent signal reaches 2.2.

Spiral antennas yield the highest signals for a given irradiance. However, our asymmetric spiral antennas show a deviation from the circular polarization expected. The wavelength dependence of the orientation of the principal axis of the elliptical polarization can be explained by a model that describes the propagation of current waves on a lossy transmission line. This model demonstrates that a balanced and an unbalanced mode propagate on the arms of the spiral. The imbalance is probably caused by the reactive impedance of the diode and by the asymmetry of the feed region. The reflection near the ends of the spiral arms influences the polarization of the antenna.

The response of our thin-film Ni–NiO–Ni diodes to 35 ps 28-THz OFID CO_2-laser pulses includes three distinct additive contributions. A fast response caused by antenna coupling is followed by a slower relaxation that consists of two diffusion effects which probably occur in the SiO_2 and Ni layers of our structures. The thermal relaxation is adequately described by two exponential functions with the characteristic times $\tau_1 \approx 100$ ns and $\tau_2 \approx 15$ ns. In consideration of these characteristic times we conclude that thermal effects are too slow to play a role in the mixing of two CO_2-laser beams for difference frequencies in the GHz range. The polarization dependence of the peak response of the diode to the short pulses corresponds to the dependence observed when detecting cw radiation. However, the contrast measured is half that found for pulse measurements.

For the first time we have achieved mixing of 28-THz radiation with thin-film diodes. Thus, we have measured laser difference frequencies up to 176 GHz in mixing processes from the second to the fifth order by irradiation of the diode with two CO_2-laser beams and microwaves generated by a Gunn oscillator. These measurements have been performed with thin-film Ni–NiO–Ni diodes connected to our optimal bow-tie antennas. The transmission of the high-frequency signals to the amplifiers was ensured by integrated rhodium waveguides, miniature flip-chip connections to coplanar waveguides on a ceramic substrate and high-frequency coaxial cables. Diode and antenna were in this arrangement irradiated through the high-transmittance Si/SiO_2 substrate. This permitted us to take advantage of the better sensitivity of an antenna to the radiation incident from the substrate side. This also reduces substrate interference fringes. The excellent polarization dependence of the mixing signals demonstrates that our antennas are almost perfectly linearly polarized. The ratio of the mixing signals for the polarization parallel to the axis of the bow-tie antenna to the signals for the cross polarization is higher than 50 at a difference frequency of 58.7 GHz. At this difference frequency, the polarization-independent thermal signals are too slow to contribute to the mixing process. In summary, our experiments extend the range of millimeter-wave and microwave thin-film techniques to the infrared.

Thin-film MOM diodes are very promising devices as fast antenna-coupled detectors which can be integrated in arrays. They also represent an alternative for the unpractical point-contacts in heterodyne measurements. Our Ni–NiO–Ni diodes remain stable over years. However, two difficulties associated with their fabrication and use should be kept in mind. First, they still demand costly handling and technology. Secondly, their operation requires precautions, because the devices are highly sensitive to electrostatic discharges and transients from the line. The performance of antenna-coupled thin-film diodes can still be enhanced. Taking into account that they certainly possess effective receiving areas smaller than point-contact diodes, we are convinced that the responsivities and the conversion efficiencies of thin-film diode will soon reach those of point contacts.

Acknowledgements

The authors are greatly indebted to Prof. H. Melchior, Prof. H. Baltes, Prof. W. Bächtold, H. Benedickter, M. Lanz, Swiss Federal Institute of Technology (ETH), Zürich; Prof. G.D. Boreman, University of Central Florida, Orlando; P. Vettiger and G. Sasso, IBM Research Laboratory, Rüschlikon; J. Siegenthaler, PTT, Bern; Dr. F. Heiniger, GR/EMD, Bern; Dr. C.O. Weiss, B. Lipphardt, PTB, Braunschweig; Dr. I. Wilke, University of Hamburg, for active support and advice. This study is supported by GR/EMD, Bern; ETH, Zürich; and IBM Research Laboratory, Rüschlikon.

References

[1] J.W. Dees, Detection and harmonic generation in the submillimeter wavelength region, Microwave J. 9 (1966) 48–55.

[2] L.O. Hocker, D.R. Sokoloff, V. Daneu, A. Szoke, A. Javan, Frequency mixing in the infrared and far-infrared using a metal-to-metal point contact diode, Appl. Phys. Lett. 12 (1968) 401–402.

[3] S.M. Faris, T.K. Gustafson, J.C. Wiesner, Detection of optical and infrared radiation with dc-biased electron-tunneling metal–barrier–metal diodes, IEEE J. Quantum Electron. QE-9 (1973) 737–745.

[4] H.-U. Daniel, M. Steiner, H. Walther, Response of metal–insulator–metal point contact diodes to visible laser light, Appl. Phys. 25 (1981) 7–12.

[5] B.-I. Twu, S.E. Schwarz, Mechanism and properties of point-contact metal–insulator–metal diode detectors at 10.6 μ, Appl. Phys. Lett. 25 (1974) 595–598.

[6] K.M. Evenson, M. Inguscio, D.A. Jennings, Point contact diode at laser frequencies, J. Appl. Phys. 57 (1985) 956–960.

[7] V. Daneu, D. Sokoloff, A. Sanchez, A. Javan, Extension of laser harmonic-frequency mixing techniques into the 9 μ region with an infrared metal–metal point contact diode, Appl. Phys. Lett. 15 (1969) 398–401.

[8] L.M. Matarrese, K.M. Evenson, Improved coupling to infrared whisker diode by use of antenna theory, Appl. Phys. Lett. 17 (1970) 8–10.

[9] B.M. Kale, Electron tunneling devices in optics, Opt. Eng. 24 (1985) 267–274.

[10] K.M. Evenson, Frequency measurements from the microwave to the visible, the speed of light, and the redefinition of the meter, in: P.H. Cutler, A.A Lucas (Eds.), Quantum Metrology and Fundamental Physical Constants, Vol. 98, Nato ASI Series B: Physics, 1983, pp. 181–197.

[11] K.M. Evenson, D.A. Jennings, F.R. Petersen, Tunable far-infrared spectroscopy, Appl. Phys. Lett. 44 (1984) 576–578.

[12] J.G. Small, G.M. Elchinger, A. Javan, A. Sanchez, F.J. Bachner, D.L. Smythe, Ac electron tunneling at infrared frequencies: Thin-film M–O–M diode structure with broad-band characteristics, Appl. Phys. Lett. 24 (1974) 275–279.

[13] S.Y. Wang, T. Izawa, T.K. Gustafson, Coupling characteristics of thin-film metal–oxide–metal diodes at 10.6 μm, Appl. Phys. Lett. 27 (1975) 481–483.

[14] T.K. Gustafson, R.V. Schmidt, J.R. Perucca, Optical detection in thin-film metal–oxide–metal diodes, Appl. Phys. Lett. 24 (1974) 620–622.

[15] A.B. Hoofring, V.J. Kapoor, W. Krawczonek, Submicron nickel–oxide–gold tunnel diode detectors for rectennas, J. Appl. Phys. 66 (1989) 430–437.

[16] T. Shimizu, H. Moritsu, Y. Yasuoka, K. Gamo, Fabrication of antenna-coupled microbolometers, Jpn. J. Appl. Phys. 34 (1995) 6352–6357.

[17] E. Wiesendanger, F.K. Kneubühl, Thin-film MOM-diodes for infrared detection, Appl. Phys. 13 (1977) 343–349.

[18] I. Wilke, Y. Oppliger, W. Herrmann, F.K. Kneubühl, Nanometer thin-film Ni–NiO–Ni diodes for 30 THz radiation, Appl. Phys. A 58 (1994) 329–341.

[19] I. Wilke, W. Herrmann, F.K. Kneubühl, Integrated nanostrip dipole antennas for coherent 30 THz infrared radiation, Appl. Phys. B 58 (1994) 87–95.

[20] H.C. Torrey, C.A. Whitmer, Crystal Rectifiers, McGraw-Hill, New York, 1948.

[21] J.C. Fisher, I. Giaever, Tunneling through thin insulating layers, J. Appl. Phys. 32 (1961) 172–177.

[22] J.G. Simmons, General formula for the electric tunnel effect between similar electrodes separated by a thin insulating film, J. Appl. Phys. 34 (1963) 1793–1803.

[23] E.H. Hauge, J.A. Støvneng, Tunneling times: A critical review, Rev. Mod. Phys. 61 (1989) 917–936.

[24] D.A. Jennings, F.R. Petersen, K.M. Evenson, Extension of absolute frequency measurements to 148 THz: Frequencies of the 2.0- and 3.5-μm Xe laser, Appl. Phys. Lett. 26 (1975) 510–511.

[25] R.E. Drullinger, K.M. Evenson, D.A. Jennings, F.R. Petersen, J.C. Bergquist, L. Burkins, H.-U. Daniel, 2.5-THz frequency difference measurements in the visible using metal–insulator–metal diodes, Appl. Phys. Lett. 42 (1983) 137–138.

[26] O. Acef, L. Hilico, M. Bahoura, F. Nez, P. De Natale, Comparison between MIM and Schottky diodes as harmonic mixers for visible and microwave sources, Opt. Commun. 109 (1994) 428–434.

[27] G.M. Elchinger, A. Sanchez, C.F. Davis, A. Javan, Mechanism of detection of radiation in a high-speed metal–metal oxide–metal junction in the visible region and at longer wavelengths, J. Appl. Phys. 47 (1976) 591–594.

[28] M. Heiblum, S. Wang, J.R. Whinnery, T.K. Gustafson, Characteristics of integrated MOM junctions at dc and at optical frequencies, IEEE J. Quantum Electron. QE-14 (1978) 159–169.

[29] J.G. Simmons, Potential barriers and emission-limited current flow between closely spaced parallel metal electrodes, J. Appl. Phys. 35 (1964) 2472–2481.

[30] G. Carelli, M. Inguscio, N. Ioli, A. Moretti, M. Prevedelli, F. Strumia, D. Pereira, On the work mechanism of MIM point contact diodes, Int. J. Infrared Millimeter Waves 13 (1992) 1014–1099.

[31] I.K. Yanson, N.I. Bogatina, Experimental observation of phonon generation in point contacts, JETP Lett. 16 (1972) 279–281.

[32] R.W. van der Heijden, S.G.M. Jansen, J.H.M. Stoelinga, H.M. Swartjes, P. Wyder, A new mechanism for high-frequency rectification at low temperatures in point contacts between identical metals, Appl. Phys. Lett. 37 (1980) 245–248.

[33] R.W. van der Heijden, H.M. Swartjes, P. Wyder, Contribution of the spreading resistance to high-frequency rectification in metal–metal point contacts, J. Appl. Phys. 55 (1984) 1003–1011.

[34] A.G.M. Jansen, P. Wyder, H. van Kempen, Point-contact spectroscopy and all that, Europhys. News 18 (1987) 21–24.

[35] A. Sanchez, C.F. Davis Jr., K.C. Liu, A. Javan, The MOM tunneling diode: Theoretical estimate of its performance at microwave and infrared frequencies, J. Appl. Phys. 49 (1978) 5270–5277.

[36] C.C. Bradley, G.J. Edwards, Characteristics of metal–insulator–metal point-contact diodes used for two-laser mixing and direct frequency measurements, IEEE J. Quantum Electron. QE-9 (1973) 548–549.

[37] S.I. Green, Point contact MOM tunneling detector analysis, J. Appl. Phys. 42 (1971) 1166–1169.

[38] C.R. Brewitt-Taylor, D.J. Gunton, H.D. Rees, Planar antennas on a dielectric surface, Electron. Lett. 17 (1981) 729–730.

[39] J.R. Carson, A generalization of the reciprocal theorem, Bell Syst. Tech. J. 3 (1924) 393–399.

[40] D.B. Rutledge, D.P. Neikirk, D.P. Kasilingam, Integrated-circuit antennas, Infrared and Millimeter Waves, Vol. 10, Chap. 1, 1983.

[41] D.B. Rutledge, M.S. Muha, Imaging antenna arrays, IEEE Trans. Antennas Propagation AP-30 (1982) 535–540.

[42] N. Engheta, C.H. Papas, C. Elachi, Interface extinction and subsurface peaking of the radiation pattern of a line source, Appl. Phys. B 26 (1981) 231–238.

[43] N. Engheta, C.H. Papas, C. Elachi, Radiation patterns of interfacial dipole antennas, Radio Sci. 17 (1982) 1557–1566.

[44] E.N. Grossman, J.E. Sauvageau, D.G. McDonald, Lithographic spiral antennas at short wavelengths, Appl. Phys. Lett. 59 (1991) 3225–3227.

[45] G. Hasnain, A. Dienes, J.R. Whinnery, Dispersion of picosecond pulses in coplanar transmission lines, IEEE Trans. Microwave Theory Tech. MTT-34 (1986) 738–741.

[46] M.Y. Frankel, S. Gupta, J.A. Valdmanis, G.A. Mourou, Terahertz attenuation and dispersion characteristics of coplanar transmission lines, IEEE Trans. Microwave Theory Tech. MTT-39 (1991) 910–915.

[47] W.J. Getsinger, Microstrip dispersion model, IEEE Trans. Microwave Theory Tech. MTT-21 (1973) 34–39.

[48] J.D. Kraus, Antennas, 2nd edn., McGraw-Hill, New York, 1988.

[49] R.H. DuHamel, D.E. Isbell, Broadband logarithmically periodic antenna structures, IRE National Convention Record, Part 1, 1957, pp. 119–128.

[50] H. Kober, Dictionary of Conformal Representations, 2nd edn., Dover Publications, New York, 1957.

[51] W. Hilberg, Ueber die Möglichkeit, gewisse Wellenwiderstansformeln, die elliptische Integrale enthalten, durch Näherungsformeln beliebig hoch wählbarer Genauigkeit zu ersetzen, Arch. Elek. Uebertragung 21 (1967) 603–616.

[52] O. Zinke, H. Brunswig, Lehrbuch der Hochfrequenztechnik, Band 1, Vierte Auflage, Springer-Verlag, Berlin, 1990.

[53] M. Abramowitz, I.A. Stegun, Handbook of Mathematical Functions, Dover, New York, 1968.

[54] G.H. Brown, O.M. Woodward, Experimentally determined radiation characteristics of conical and triangular antennas, RCA Rev. 13 (1952) 425–452.

[55] R.C. Compton, R.C. McPhedran, Z. Popovic, G.M. Rebeiz, P.P. Tong, D.B. Rutledge, Bow-tie antennas on a dielectric half-space: Theory and experiment, IEEE Trans. Antennas Propagation AP-35 (1987) 622–631.

[56] V.H. Rumsey, Frequency independent antennas, IRE National Convention Record, Part 1, 1957 pp. 114–118.

[57] J.D. Dyson, The equiangular spiral antenna, IRE Trans. Antennas Propagation 7 (1959) 181–187.

[58] J.A. Kaiser, The archimedean two-wire spiral antenna, IRE Trans. Antennas Propagation 8 (1960) 312–323.

[59] T.H. Büttgenbach, R.E. Miller, M.J. Wengler, D.M. Watson, T.G. Phillips, A broad-band low-noise SIS receiver for submillimeter astronomy, IEEE Trans. Microwave Theory Tech. MTT-36 (1988) 1720–1725.

[60] B.R.-S. Cheo, V.H. Rumsey, W.J. Welch, A solution to the frequency-independent antenna problem, IRE Trans. Antennas Propagation AP-9 (1961) 527–534.

[61] C.A. Balanis, Antenna Theory (Analysis and Design), 2nd edn., Wiley, 1997.

[62] A. Betz, Konforme Abbildung, 2nd edn., Springer-Verlag, Berlin, 1964.

[63] W.L. Curtis, Spiral antennas, IRE Trans. Antennas Propagation 8 (1960) 298–306.

[64] G.D. Boreman, A. Dogariu, C. Christodoulou, D. Kotter, Dipole-on-dielectric model for infrared lithographic spiral antennas, Opt. Lett. 21 (1996) 309–311.

[65] V.H. Rumsey, Frequency Independent Antennas, Academic Press, 1966.

[66] R.C. Johnson, H. Jasik (Eds.), Antenna Engineering Handbook, 2nd edn., McGraw-Hill, New York, 1984.

[67] T.H.P. Chang, D.P. Kern, E. Kratschmer, K.Y. Lee, H.E. Luhn, M.A. McCord, S.A. Rishton, Y. Vladimirsky, Nanostructure technology, IBM J. Res. Dev. 32 (1988) 462–493.

[68] K.V. Rao, A. Smakula, Dielectric properties of cobald oxide, nickel oxide, and their mixed crystals, J. Appl. Phys. 36 (1965) 2031–2037.

[69] N. Fuschillo, B. Lalevic, B. Leung, Dielectric properties of NiO and NiO(Li), Thin Solid Films 24 (1974) 181–192.

[70] N. Fuschillo, B. Lalevic, B. Leung, Electrical conduction and dielectric breakdown in crystalline NiO and NiO(Li) films, J. Appl. Phys. 46 (1975) 310–316.

[71] S. Mochizuki, Radiative optical modes of vibration in NiO thin film, Phys. Status Solidi B 126 (1984) 105–114.

[72] F. Vasey, D. Prongué, H. Rothuizen, P. Vettiger, Electron-beam lithography of curved structures with an enhanced vector-scan pattern generator supporting conic-based primitives, J. Vac. Sci. Technol. B 12 (1994) 34603–34604.

[73] H. Mott, Polarization in Antennas and Radar, Wiley, New York, 1986.

[74] K.C. Gupta, R. Garg, I.J. Bahl, Microstrip Lines and Slotlines, Artech, Dedham, 1979.

[75] G. Ghione, C.U. Naldi, Analytical formulas for coplanar lines in hybrid and monolithic MICs, Electron. Lett. 20 (1984) 278–279.

[76] R. Goyal (Ed.), Monolithic Microwave Integrated Circuits: Technology and Design, Artech House, Norwood, MA, 1989.

[77] A. Rosen, M. Caulton, P. Stabile, A.M. Gombar, W.M. Janton, C.P. Wu, J.F. Corboy, C.W. Magee, Silicon as a millimeter-wave monolithically integrated substrate—A new look, RCA Rev. 42 (1981) 633–660.

[78] C. Fumeaux, W. Herrmann, H. Rothuizen, P. De Natale, F.K. Kneubühl, Mixing of 30 THz laser radiation with nanometer thin-film Ni–NiO–Ni diodes and integrated bow-tie antennas, Appl. Phys. B 63 (1996) 135–140.

[79] W. Schreiter, Seltene Metalle, Band II. Veb Deutscher Verlag für Grundstoffindustrie, Leipzig, 1961.

[80] A. Edgar, A. Zyskowski, A versatile system for inelastic electron tunneling spectroscopy, J. Phys. E 18 (1985) 863–868.

[81] R. Holm, Electric contacts, 4th edn., Springer-Verlag, Berlin, 1967.

[82] B.G. Whitford, Experimental nonlinearity coefficients for the tungsten–nickel point-contact diode, IEEE J. Quantum Electron. QE-18 (1982) 428–432.

[83] M. Born, E. Wolf, Principles of Optics, 6th edn., Pergamon, 1980.

[84] E.D. Palik (Ed.), Handbook of Optical Constants of Solids, Academic Press, 1985.

[85] F.K. Kneubühl, M.W. Sigrist, Laser, 4th edn., Teubner Studienbücher, Stuttgart, 1995.

[86] M. Rossi, R.E. Kunz, H.P. Herzig, Refractive and diffractive properties of planar micro-optical elements, Appl. Opt. 34 (1995) 5996–6007.

[87] G.M. Rebeiz, W.G. Regher, D.B. Rutledge, R.L. Savage, N.C. Luhmann Jr., Submillimeter-wave antennas on thin membranes, Int. J. Infrared Millimeter Waves 8 (1987) 1249–1255.

[88] G.D. Boreman, A. Dogariu, C. Christodoulou, D. Kotter, Modulation transfer function of antenna-coupled infrared detector arrays, Appl. Opt. 35 (1996) 6110–6114.

[89] H. Poincaré, Théorie Mathématiques de la Lumière, Vol. 2, Gauthier-Villars, Paris, 1892.

[90] P.S. Theocaris, Modern methods in polarisation optics, in: G.S. Holister (Ed.), Developments in Stress Analysis, Vol. 1, Applied Science Publ., London, 1979.

[91] F.K. Kneubühl, Oscillations and Waves, Springer-Verlag, Berlin, 1997.

[92] C. Fumeaux, G.D. Boreman, W. Herrmann, H. Rothuizen, F.K. Kneubühl, Polarization response of asymmetric-spiral infrared antennas, Appl. Opt. 36 (1997) 6485–6490.

[93] R.G. Corzine, J.A. Mosko, Four-arm Spiral Antennas, Artech House, Norwood, MA, 1990.

[94] A.W. Kälin, R. Kesselring, C. Hongru, F.K. Kneubühl, Optical-free-induction-decay (OFID) 10 μm CO_2 laser systems, Infrared Phys. 33 (1992) 73–112.

[95] D.P. Scherrer, F.K. Kneubühl, First realization of new ps-10 μm-CO_2-OFID laser systems with far-infrared laser gases as spectral filters, Infrared Phys. 33 (1992) 67–70.

[96] R. Kesselring, A.W. Kälin, H.J. Schötzau, F.K. Kneubühl, Picosecond CO_2 laser pulse generation and amplification, IEEE J. Quantum Electron. QE-29 (1993) 997–1004.

[97] J. Knittel, D.P. Scherrer, F.K. Kneubühl, The first optical-free-induction-decay system with a tunable single-mode high-pressure CO_2 laser, Infrared Phys. 35 (1994) 67–71.

[98] J. Knittel, D.P. Scherrer, F.K. Kneubühl, High-pressure single-mode CO_2 laser with ps-plasma shutter, Opt. Eng. 34 (1995) 2000–2016.

[99] C. Fumeaux, W. Herrmann, F.K. Kneubühl, H. Rothuizen, B. Lipphardt, C.O. Weiss, Mixing of 28-THz (10.7 μm) CO_2-laser radiation by nanometer thin-film Ni–NiO–Ni diodes with difference frequencies up to 176 GHz, Infrared Phys. Technol. 38 (1997) 393–396.

[100] C. Fumeaux, W. Herrmann, F.K. Kneubühl, H. Rothuizen, B. Lipphardt, C.O. Weiss, Nanometer thin-film Ni–NiO–Ni diodes for mixing 28-THz CO_2-laser emissions with difference frequencies up to 176 GHz, Appl. Phys. B 66 (1998) 327–332.

[101] H. Schnatz, B. Lipphardt, J. Helmcke, F. Riehle, G. Zinner, First phase-coherent frequency measurement of visible radiation, Phys. Rev. Lett. 76 (1996) 18–21.

[102] K.M. Baird, H.D. Riccius, K.J. Siemsen, CO_2 wavelengths and the velocity of light, Opt. Commun. 6 (1972) 91–95.

[103] H.H. Klingenberg, C.O. Weiss, Rectification and harmonic generation with metal–insulator–metal diodes in the mid-infrared, Appl. Phys. Lett. 43 (1983) 361–363.

[104] T. Kurosawa, Properties of the S/N ratio of the beat note in frequency-mixing using the W–Ni point contact diode at 32 THz, Jpn. J. Appl. Phys. 27 (1988) 55–61.

[105] E. Sakuma, K.M. Evenson, Characteristics of tungsten–nickel point contact diodes used as laser harmonic-generator mixers, IEEE J. Quantum Electron. QE-10 (1974) 599–603.

[106] T. Kurosawa, T. Sakurai, K. Tanaka, DC bias dependence of W–Ni and W–Co point-contact diodes as harmonic generators and mixers at 9.4 μm, Appl. Phys. Lett. 36 (1980) 751–754.

[107] H.-W. Hübers, G.W. Schwaab, H.P. Röser, Video detection and mixing performance of GaAs Schottky-barrier diodes at 30 THz and comparison with metal–insulator–metal diodes, J. Appl. Phys. 75 (1994) 4243–4248.

[108] W. Krieger, T. Suzuki, M. Völcker, H. Walther, Generation of microwave radiation in the tunneling junction of a scanning tunneling microscope, Phys. Rev. B 41 (1990) 10229–10232, also W. Krieger, private communication (1997).

[109] M. Schicke, T. Lehnert, K.H. Gundlach, H. Rothermel, P. Dieleman, T.M. Klapwijk, H. van de Stadt, NbN tunnel junctions with Al Striplines and NbN transition-edge bolometers for terahertz mixers, Proceedings of the ESA Symposium SP-401, The Far Infrared and Submillimetre Universe, Grenoble (15–17 April 1997).

[110] H. Rothermel, B. Plathner, K.H. Gundlach, M. Aoyagi, S. Takada, Antenna-coupled superconducting contacts in submillimeter and FIR astronomy, Infrared Phys. Technol. 35 (1994) 463–476.